

Dissertation

The composition-dependent conductivity of $\text{Li}_7\text{La}_3\text{Zr}_2\text{O}_{12}$ ceramics investigated by spatially resolved impedance spectroscopy

ausgeführt zum Zwecke der Erlangung des akademischen Grades eines
Doktors der technischen Wissenschaften

unter der Leitung von

Univ.-Prof. Dipl.-Phys. Dr. Jürgen Fleig

am Institut für chemische Technologien und Analytik
im Fachbereich Elektrochemie


eingereicht an der Technischen Universität Wien
Fakultät für Technische Chemie

von

Dipl. Ing. Andreas Wachter-Welzl

Matrikelnr. 0528007
Oberhoferstrasse 7A/2/10
A-2130 Mistelbach

Niederösterreich, im Oktober 2017

You get the results you deserve, but not the ones you need. 

Chapter 1

Abstract

Current Li-ion batteries suffer from problems caused by the chemical instability of their organic electrolyte. Therefore, a lot of research focuses on replacing the organic electrolyte by inorganic solid ion conductors. The cubic $\text{Li}_7\text{La}_3\text{Zr}_2\text{O}_{12}$ (LLZO) garnet and its variants are among the most promising candidates for next generation all solid state Li-ion batteries. This thesis presents a detailed study on effects of compositional variations and of common sintering techniques on the overall performance of LLZO, investigated by electrochemical impedance spectroscopy (EIS). Roles of sintering temperature, preparation procedure and sample dimension are considered and reasons behind severe variations of effective Li-ion conductivities are discussed. Besides overall Li-ion conductivity, measurements on microelectrodes were performed to obtain information on local Li-ion conductivities. Those were combined with ICP-OES (inductively coupled plasma optical emission spectrometry) measurements to analyze how variations in lithium and aluminium (dopant) content affect the Li-ion conductivity.

Chapter 2

Kurzfassung

Eines der größten Probleme moderner Li-Batterien ist die chemische Instabilität ihrer organischen Elektrolyte. Aus diesem Grund konzentriert sich ein Teil der Batterieforschung darauf, organische Elektrolyte durch inorganische Festkörperelektrolyte zu ersetzen. Aktuell ist der kubische Granat $\text{Li}_7\text{La}_3\text{Zr}_2\text{O}_{12}$ (LLZO) einer der aussichtsreichsten Kandidaten mit denen die nächste Generation von Festkörperlithiumbatterien gebaut werden könnte.

Diese Arbeit präsentiert eine detaillierte Studie über die Auswirkung von Zusammensetzungsvariationen, und die damit zusammenhängende Probensinterung auf das Betriebsverhalten von LLZO. Untersuchungen wurden mit Hilfe elektrochemischer Impedanzspektroskopie durchgeführt. Einflüsse wie Sintertemperatur, Herstellungsprozedur und Probengeometrie werden untersucht und Gründe für die starken Schwankungen der effektiven Leitfähigkeit diskutiert. Neben Messungen der effektiven ionischen Leitfähigkeit von Lithium wurden auch Messungen an mikrostrukturierten Elektroden durchgeführt, welche es erlauben Informationen über lokale Leitfähigkeiten zu erhalten. Diese Resultate wurden kombiniert mit ICP-OES (induktiv gekoppeltes Plasma - optische Emissionsspektroskopie), um zu analysieren, welchen Einfluss Lithium oder Aluminium (Dotierelement) auf die Li-Ionenleitfähigkeit ausübt.

Contents

1	Abstract	3
2	Kurzfassung	4
3	Introduction	7
4	Experimental	16
4.1	Overview	16
4.2	Macroelectrodes	17
4.2.1	Variations of pressure during sample preparation	17
4.2.2	Optimization of electrode material	18
4.3	Optimization of the macro-measurement set-up	20
4.3.1	Motivation for new set-up	20
4.3.2	Realization of improved macro-measurement set-up	21
4.4	Microelectrodes	25
5	Results and Discussion	30
5.1	The origin of conductivity variations in Al-substituted $\text{Li}_7\text{La}_3\text{Zr}_2\text{O}_{12}$ ceramics	30
5.1.1	Experimental	30
5.1.2	Results and Discussion	32
5.1.3	Influence of sample's height	40
5.1.4	Conclusion	43

5.2	The temperature dependent conductivity of LLZO with different composition	44
5.2.1	Mid-frequency contributions	47
5.3	Electrochemical investigation of a tetragonal LLZO sample	52
5.4	Properties of a Ta-stabilized LLZO single crystal	57
5.5	Microelectrodes for local conductivity and degradation measurements on Al stabilized $\text{Li}_7\text{La}_3\text{Zr}_2\text{O}_{12}$	66
5.5.1	Experimental	66
5.5.2	Results and Discussion	68
5.5.3	Conclusion	76
5.6	Li-ion conductivity fluctuations within $\text{Li}_7\text{La}_3\text{Zr}_2\text{O}_{12}$ solid electrolytes and their relation to local stoichiometric changes	77
5.6.1	Experimental	77
5.6.2	Results	81
5.6.3	Conclusion	91
5.6.4	Supplementary	92
5.7	Effects of annealing	94
5.8	Degradation of LLZO garnet material	100
5.8.1	Proton exchange	101
5.8.2	Site occupation	101
5.8.3	Preparation	103
5.8.4	Results	104
6	Summary	107
7	Acknowledgment	109
8	Curriculum Vitae	111
9	Bibliography	115

Chapter 3

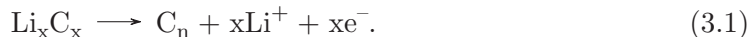
Introduction

During the last decades, technological advancements such as electrical cars, smartphones or tablets and the need for large-scale energy storage has made research in the field of batteries on the one side very attractive and on the other side very challenging. Challenging, because the requirements in terms of safety, cycling behavior or lifetime are constantly growing. The lithium ion battery (LIB) is the most frequently used type of battery in portable devices as well as in vehicles due to its high energy density (energy stored per mass or volume).

A LIB is a secondary cell, meaning that after discharge the cell can be recharged by electric current. Lithium as mobile ion holds some advantages against other competitors, since it is the third lightest element and it has the lowest reduction potential of any element (-3.04 eV against SHE) [1]. Therefore, LIBs excel in gravimetric ($150 - 190 \text{ Wh kg}^{-1}$) and volumetric energy density ($250 - 380 \text{ Wh L}^{-1}$), making it the best power supply for numerous applications [2]. Compared to the lead acid battery, which was developed in the 19th century, LIBs are a relatively young battery type with first concept development in the 1970s by Whittingham [3]. Twenty years later, Sony presented the first commercially available lithium ion battery in 1991 [3, 4].

A LIB is composed of an anode (source for lithium), a cathode (sink for lithium) and an electrolyte separating the electrodes. If the battery is discharged, the Li containing

carbon anode is oxidized



Li^+ -ions then move through the electrolyte to the cathode and electrons are directed through an external circuit. Carbon is used as anode material, because it is relatively cheap, has a low delithiation potential vs Li, a high electrical conductivity and a low volume change during lithiation/delithiation [5–8]. Other possible anode materials are $\text{Li}_4\text{Ti}_5\text{O}_{12}$ and alloying materials such as Si, Ge, Sn storing lithium ions [9–14]. Li^+ -ions move through an electrolyte consisting of a lithium salt like LiBF_4 , LiPF_6 , LiCF_3SO_3 solved in an organic solvent such as ethylene carbonate or dimethyl carbonate [15–19]. On the cathode side, Li^+ -ions and e^- enter the oxide according to



and thus formally neutral Li is intercalated. Typical cathode materials are LiFePO_4 and LiMO_2 ($M = \text{Ni}, \text{Mn}, \text{Co}$) which is the most commonly used electrode [20–26]. Organic electrolytes are highly flammable and thus are a safety risk in LIB. Reasons for catching fire or even explosion are overcharging with oxygen evolution from the cathodes and internal short-circuits, e.g. due to production faults or damage. Moreover, Li metal can not be used as a high capacitance anode since it is prone to dendrite formation during charging and thus leading to internal short circuits. Moreover, the reactivity of organic electrolytes with Li will lead to a permanent loss of capacity. A possible way out is the use of a solid state electrolyte, as it is non flammable and can be chemically inert against lithium metal. In order to stay economically competitive to common LIBs, a few criteria have to be met by solid electrolytes:

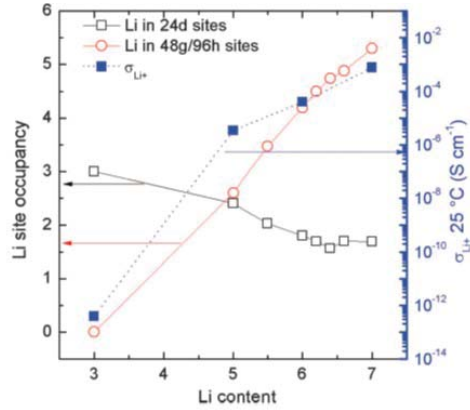
- high ionic conductivity (preferably $\approx 10^{-3} \text{ S cm}^{-1}$).
- chemical stability against Li electrodes
- chemical stability against high voltages ($> 5 \text{ V vs Li}$)
- mechanical and thermal stability

- low interface resistance between electrolyte and electrodes
- low costs and the usage of environmental friendly elements
- accessible by thin film preparation techniques

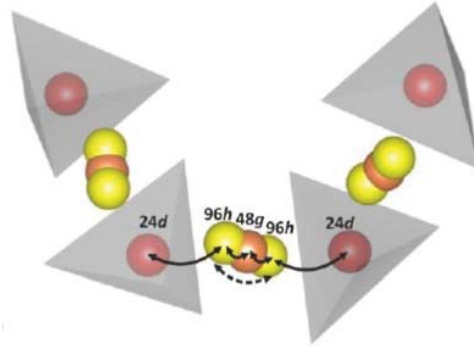
Numerous types of Li-conducting solid electrolytes are known so far (perovskites - $\text{La}_{2/3-x}\text{Li}_{3x}\text{TiO}_3$, oxides with the structure of NASICON - sodium super ionic conductors, Li- β -alumina) [27–30]. Each of them has drawbacks like a high grain boundary resistance, instability against lithium metal or a poor electrochemical stability.

One promising candidate is the garnet based cubic $\text{Li}_7\text{La}_3\text{Zr}_2\text{O}_{12}$ (LLZO) solid state electrolyte [31–33]. Its basic crystal structure is written as $\text{A}_3\text{B}_2(\text{CO}_4)_3$. The garnet structure provides three different sites: tetrahedral, octahedral and dodecahedral sites. Tetrahedral sites are energetically speaking, the most favorable sites for Li-ions and can be occupied by a maximum of three lithium ions. For La on the A site and Zr on the B site the adjustment to the total cation charge requires further incorporation of lithium ions. Those will occupy octahedral sites. As a result, the garnet becomes a lithium ion conductor. A garnet inheriting more than 3 Li-ions pfu is referred to as Li-stuffed garnet. The first study on Li-stuffed garnets was published by Thangadurai *et al.* 2003 in which a cubic garnet specimen with the chemical formula of $\text{Li}_5\text{La}_3\text{M}_2\text{O}_{12}$ ($\text{M} = \text{Nb}, \text{Ta}$) (Li-5 phases) was investigated [33]. The garnet showed an ionic conductivity of $10^{-6} \text{ S cm}^{-1}$ and a chemical stability against molten lithium. In subsequent years, research activities were focused on understanding the role of site occupation, conductivity mechanism, sintering conditions and so on.

The occupation of tetrahedral (24d) and octahedral (48g, 96h) sites turned out to be a pivotal point to enhance the ionic conductivity of the garnet. O’Callaghan *et al.* showed for $\text{Li}_3\text{Ln}_3\text{Te}_2\text{O}_{12}$, that the Li-ions on tetrahedral sites are less mobile and therefore not responsible for the improved conductivity of Li-stuffed garnets [35]. Rather the creation of vacancies on tetrahedral sites due to site occupation of octahedral sites lead to an improved ionic conductivity. Figure 3.1 a) illustrates the effect how Li incorporation increases the site occupation of octahedral sites and enhances ionic conductivity [33, 35–39]. Theoretically, the upper limit of Li concentration is 7.5 pfu, and suggesting that



(a) Occupation and conductivity



(b) Site diffusion

Figure 3.1: a) The occupation of tetrahedral and octahedral sites for Li-stuffed garnets. A high amount of lithium goes along with enhanced ionic conductivity [34].
 b) Diffusion path of Li-ions between octahedral and tetrahedral sites.

the ionic conductivity can not continuously be improved by simply adding more lithium ions into the garnet [39].

In 2007, Murugan proposed a garnet that hosts 7 lithium atoms pfu, however the garnet transformed into a lower conductive tetragonal structure ($I4_1\bar{a}cd$ - see Figure 3.2 a) [41, 42]. At temperatures above 750 °C, Percival *et al.* observed the transition from tetragonal to cubic structure and it seemed as if the cubic structure was only an entropy driven high temperature modification of the garnet [43, 44].

In the tetragonal phase, there are three different sites Li^+ can occupy:

- 8a - tetrahedral
- 16f - octahedral
- 32g - octahedral

For a total amount of 56 Li-atoms in a unit cell and 56 available sites, Li ions are ordered and this reduces the electrostatic energy between tetrahedral and octahedral sites. Since vacancies on tetrahedral sites are missing, the ionic conductivity drops by two orders of magnitude, compared to cubic LLZO [45].

In the cubic structure (see Figure 3.2 b) the following sites are available:

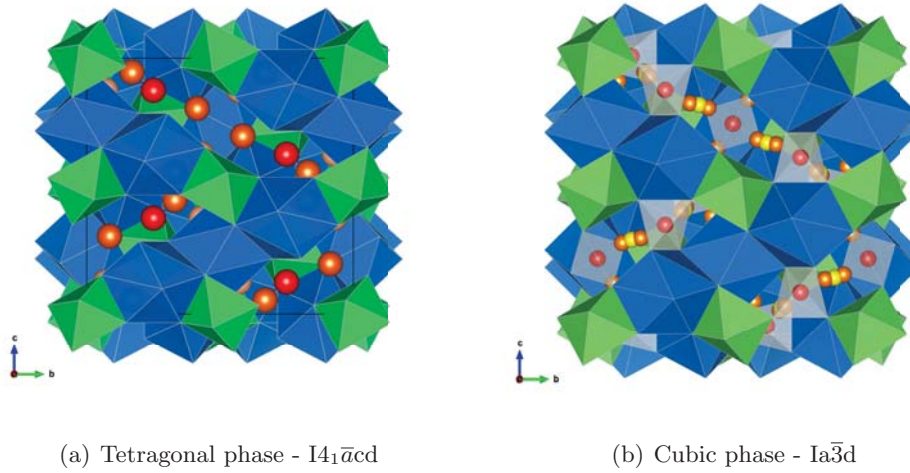


Figure 3.2: Crystal structure of tetragonal und cubic LLZO. Green octahedra (16a) are occupied by Zr^{4+} , blue dodecahedra by La^{3+} (24c). a) Ordered distribution of Li-ions occupying sites 8a, 16f and 32g. b) Li-ions partially occupy 24d (red - spheres), 48g (orange) and 96h (yellow) sites [40].

- 24d - tetrahedral
- 48g - octahedral
- 96h - octahedral

The number of available sites in cubic structure is 120 and thus numerous unoccupied sites exist and enable high conductivity. The distribution and occupation of Li-ions follows some rules but generally speaking they are disordered. Compared to the tetragonal phase, the distance between sites in a cubic structure is shorter. Therefore coulomb interaction between Li-ions becomes a determining factor in site occupation. For example, if a tetrahedral site (24d) is occupied, the nearest site (from the shared octahedra) 48g can no longer be occupied due to coulomb repulsion. Instead the ion has to move on to the next available site (96h) instead. The mechanism also works the other way around, if the 48g position is occupied the 96h and the 24d position have to be empty. Figure 3.1 b) illustrates the possible diffusion paths between tetrahedral and octahedral sites. When taking account of the repulsive coulomb interaction, the number of available

octahedral sites is reduced to 48 and the total number of available lithium sites drops down to 72 [46].

Based on these 72 sites, the site occupation preference is also of great interest. Awaka *et al.* proposed a 100 % occupation of tetrahedral sites for Li₇-stuffed LLZO [47]. However, recent nuclear magnetic resonance or neutron powder experiments measured the level of tetrahedral occupation to be about 50 % and 90 % for octahedral positions [39, 48, 49]. Stabilizing the cubic phase at room temperature happened at first by accident. First investigations revealed an inadvertent incorporation of aluminium from the Al crucible the sample was placed in for annealing. Later on, different research groups confirmed the role of Al in stabilizing the cubic phase at room temperature and the new chemical composition of the garnet was Li_{7-x}Al_xLa₃Zr₂O₁₂, with aluminium substituting lithium [50–52]. Subsequently, research groups tried to find other elements for the A, B and C site of the garnet suitable to stabilize the cubic phase at room temperature. Table 3.1 shows the different elements, for which the cubic phase could be stabilized successfully and the site they occupy. Regardless of the stabilizing ion the formation of Li vacancies is essential to stabilize the cubic structure at RT. The level of aliovalent doping does not have to be particularly high, 6.5 - 6.6 Li pfu should already be sufficient to gain the cubic phase [53, 54].

The introduction of these elements raises new questions, like their preferred site occupation. The occupation of aluminium has been investigated by Rettenwander *et al.*, where he could show, using density functional theory (DFT) and nuclear magnetic resonance (NMR), that aluminum preferentially occupies 24d-tetrahedral sites as well as 96h-octahedral sites [55]. The same is true for gallium stabilized LLZO, but interestingly the ionic conductivities obtained by gallium incorporation are by a factor of three higher than by aluminium incorporation [56].

Another highly debated topic is the stability of LLZO in ambient air. At the surface, reaction with moisture and carbon dioxide leads to the formation of lithiumhydroxide (LiOH) and carbonate (Li₂CO₃) [57–68]. CO₂ and H₂O are not only important for normal operation mode, also the preparation may be affected by water and CO₂. Both of them can trigger a low temperature cubic phase transformation through the substitution

of Li^+ by H^+ . Further heating reverses the Li^+/H^+ reaction and the original garnet is reestablished [43, 59, 69, 70].

Up to now, much knowledge has been collected on different material properties of LLZO. A lot of publications are related to aluminium stabilized LLZO, simply because it was the first element found to stabilize the cubic structure. However, published data on bulk conductivities vary significantly although preparation processes and aliovalent levels of doping are comparable. For example, bulk conductivities reported for Al stabilized LLZO between 0.17 and 0.35 pfu vary in the range of $10^{-4} \text{ S cm}^{-1}$ to more than $10^{-3} \text{ S cm}^{-1}$. Effective sample conductivities were lower, varying between 1.4 and $5.7 \times 10^{-4} \text{ S cm}^{-1}$ (see Table 3.2 for details). Some differences can be related to different preparation routes such as hot isostatic pressing (HIP) or field assisted sintering technique (FAST) resulting in very high densities ($> 96\%$). Nevertheless, samples with a high density and an exceedingly high bulk conductivity ($1.35 \times 10^{-3} \text{ S cm}^{-1}$ [71]) suffered from high grain boundary resistances resulting in a lower effective conductivity.

These variations despite apparently identical sample compositions, and also the severe dependence of the conductivity on the specific stabilizing (dopant) ion are still not understood and require further studies.

In this thesis several factors affecting the Li-ion conductivity of LLZO are therefore analyzed in detail. Among others, the conductivities of 44 LLZO samples with Al^{3+} contents of 0.20 Al pfu were investigated to clarify whether different conductivities are largely a result of laboratory-specific processing or if they also occur for samples with nominally identical preparation. The electrochemical homogeneity of numerous samples was then further investigated by a combination of stepwise geometric size reduction and impedance spectroscopy. These measurements revealed the existence of strong conductivity scattering within one and the same sample. Despite the same preparation route is applied, distinct conductivity variations were found in many samples. The effects of the substitutional element and its amount on the temperature dependent conductivity is described in Chapter 5.1.

To further investigate the origin of conductivity fluctuations, microelectrodes are the perfect tool. Impedance spectroscopic studies on circular microelectrodes with diame-

Table 3.1: Substitutional elements stabilizing the cubic structure at room temperature.

Site	Substitution element	Ref.
Li	Zn ²⁺ , Al ³⁺ , Ga ³⁺ , Fe ³⁺	[50, 51, 55, 76–83]
La	Ce ⁴⁺	[84]
Zr	Ta ⁵⁺ , Nb ⁵⁺ , Bi ⁵⁺ , Sb ⁵⁺ Mo ⁶⁺ , Te ⁶⁺ , W ⁶⁺	[40, 81, 85–94]

ters of a few micrometers can reveal the bulk conductivity of a similarly sized region beneath and are also very sensitive to high or low conductive zones near-surface [72–75]. For the first time this tool was applied to LLZO samples. Comparisons are made between the overall performance of Al stabilized samples and local Li-ion conductivities, obtained by ionically blocking microelectrodes (\varnothing : 20 – 300 μm). A scattering of local conductivities within one and the same sample was found. In addition, changes of the spectra measured by microelectrodes before and after long-time exposure to ambient air revealed the degradation of near-surface regions in such measurements (Chapter 5.5). In order to investigate the effects of compositional gradients on the ionic conductivity, a combination of microelectrode impedance spectroscopy and LA-ICP-OES was employed. Circular microelectrodes with diameters of 100 μm were used for microelectrode impedance spectroscopic studies. Afterwards, the areas beneath the electrodes were analyzed by laser ablation inductively coupled plasma optical emission spectrometry (LA-ICP-OES) and revealed information on the correlation between Al or Li content and the ionic conductivity (Chapter 5.6). Together with results of several other experiments, all these data significantly improved the understanding of Li-ion conduction in LLZO.

Table 3.2: Conductivities of LLZO samples with similar Al^{3+} contents reported in literature. * calculated value

Composition	T_{sint} [°C]	Time	Preparation route	σ_{bulk}	σ_{eff} [S cm^{-1}]	T_{meas}
$\text{Li}_{6.49}\text{Al}_{0.17}\text{La}_3\text{Zr}_2\text{O}_{12}$	1160	2h	HIP	9.90×10^{-4}	2.42×10^{-4}	25 °C [95]
$\text{Li}_{6.49}\text{Al}_{0.17}\text{La}_3\text{Zr}_2\text{O}_{12}$	950	10 min	NFS & FAST	-	3.30×10^{-4}	25 °C [96]
$\text{Li}_{6.49}\text{Al}_{0.17}\text{La}_3\text{Zr}_2\text{O}_{12}$	1180	36 h		4.38×10^{-4}	2.99×10^{-4}	25 °C [97]
$\text{Li}_{6.40}\text{Al}_{0.19}\text{La}_3\text{Zr}_2\text{O}_{11.8}$	1200	36 h	Sol Gel	3.10×10^{-4}	1.40×10^{-4}	25 °C [49]
$\text{Li}_{6.40}\text{Al}_{0.20}\text{La}_3\text{Zr}_2\text{O}_{12}$	1230	6 h		-	3.00×10^{-4}	25 °C [98]
$\text{Li}_{6.40}\text{Al}_{0.20}\text{La}_3\text{Zr}_2\text{O}_{12}$	1200	2 h		3.41×10^{-4}	-	25 °C [99]
$\text{Li}_{6.40}\text{Al}_{0.20}\text{La}_3\text{Zr}_2\text{O}_{12}$	950	10 min	NFS & FAST	-	3.10×10^{-4}	25 °C [96]
$\text{Li}_{6.37}\text{Al}_{0.21}\text{La}_3\text{Zr}_2\text{O}_{12}$	1000	36 h		2.40×10^{-4}	1.40×10^{-4}	30 °C [100]
$\text{Li}_{6.34}\text{Al}_{0.22}\text{La}_3\text{Zr}_2\text{O}_{12}$	1230	36 h		-	2.40×10^{-4}	25 °C [101]
$\text{Li}_{6.24}\text{Al}_{0.24}\text{La}_3\text{Zr}_2\text{O}_{12}$	1000	4 h		4.00×10^{-4}	-	RT [77]
$\text{Li}_{6.28}\text{Al}_{0.24}\text{La}_3\text{Zr}_2\text{O}_{12}$	-	-		-	3.00×10^{-4} *	25 °C [102]
$\text{Li}_{6.25}\text{Al}_{0.25}\text{La}_3\text{Zr}_2\text{O}_{12}$	1075	10 h		5.00×10^{-4}	-	RT [103]
$\text{Li}_{6.27}\text{Al}_{0.25}\text{La}_3\text{Zr}_{1.96}\text{Pt}_{0.036}\text{O}_{12}$	1200	24 h		-	4.48×10^{-4}	25 °C [68]
$\text{Li}_{6.25}\text{Al}_{0.25}\text{La}_3\text{Zr}_2\text{O}_{12}$	1150	3 min	FAST	1.35×10^{-3}	5.56×10^{-4}	20 °C [71]
$\text{Li}_{6.25}\text{Al}_{0.25}\text{La}_3\text{Zr}_2\text{O}_{12}$	1000	3 min	FAST	-	3.32×10^{-4}	RT [104]
$\text{Li}_{6.25}\text{Al}_{0.25}\text{La}_3\text{Zr}_2\text{O}_{12}$	1150	10 min	FAST	-	5.70×10^{-4}	25 °C [105]
$\text{Li}_{6.25}\text{Al}_{0.25}\text{La}_3\text{Zr}_2\text{O}_{12}$	1300	1 h		3.10×10^{-4}	2.10×10^{-4}	25 °C [106]
$\text{Li}_{6.19}\text{Al}_{0.27}\text{La}_3\text{Zr}_2\text{O}_{12}$	1050	-	HIP	3.40×10^{-4}	-	20 °C [107]
$\text{Li}_{6.10}\text{Al}_{0.30}\text{La}_3\text{Zr}_2\text{O}_{12}$	1200	24 h		2.11×10^{-4}	-	25 °C [108]
$\text{Li}_{6.10}\text{Al}_{0.30}\text{La}_3\text{Zr}_2\text{O}_{12}$	1200	24 h		-	2.25×10^{-4}	RT [109]
$\text{Li}_{6.10}\text{Al}_{0.30}\text{La}_3\text{Zr}_2\text{O}_{12}$	1100	6 h		-	2.30×10^{-4}	RT [110]
$\text{Li}_{5.61}\text{Al}_{0.33}\text{La}_3\text{Zr}_{1.95}\text{O}_{11.70}$	1100	6 h		2.30×10^{-4}	-	25 °C [111]
$\text{Li}_{5.95}\text{Al}_{0.35}\text{La}_3\text{Zr}_2\text{O}_{12}$	1100	1 h	HIP	4.10×10^{-4}	3.70×10^{-4}	RT [112]

Chapter 4

Experimental

4.1 Overview

Most experiments of this study were performed on LLZO samples of many different compositions prepared at the University of Salzburg. Al, Ga, Mo, Nb, Ta, Fe and Bi were used as substitutional elements, amounts were varied in a wide range, e.g. from 0.1 to 0.4 pfu for Al and 0.125 to 2 for Nb. Also different sintering temperatures and sample thicknesses were employed. Details on the sample preparation can be found in a publication of Wagner *et al.* [113] and more specific information is also given in the corresponding parts of the Results and Discussion section. The effective sample conductivities were determined by electrochemical impedance spectroscopic measurements. Details on these measurements and on the impedance analysis are also given in the specific Results and Discussion parts.

Electrode optimization took place prior to all these studies and the results are in detail discussed below (Chapter 4.2.2). Moreover during the thesis the electrochemical measurement set-up was optimized to allow impedance measurements at very high frequencies; this is described in Chapter 4.3.2. Many studies were also performed by microelectrodes on the LLZO samples and details on the problems and optimization of microelectrode measurements are shown in Chapter 4.4.

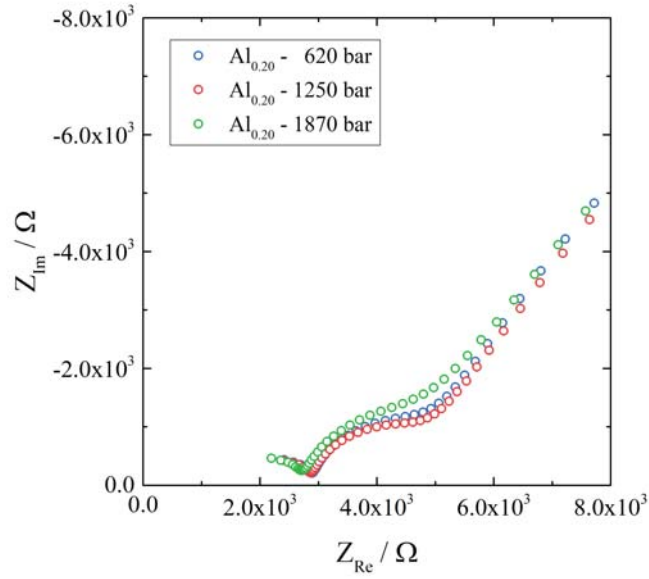
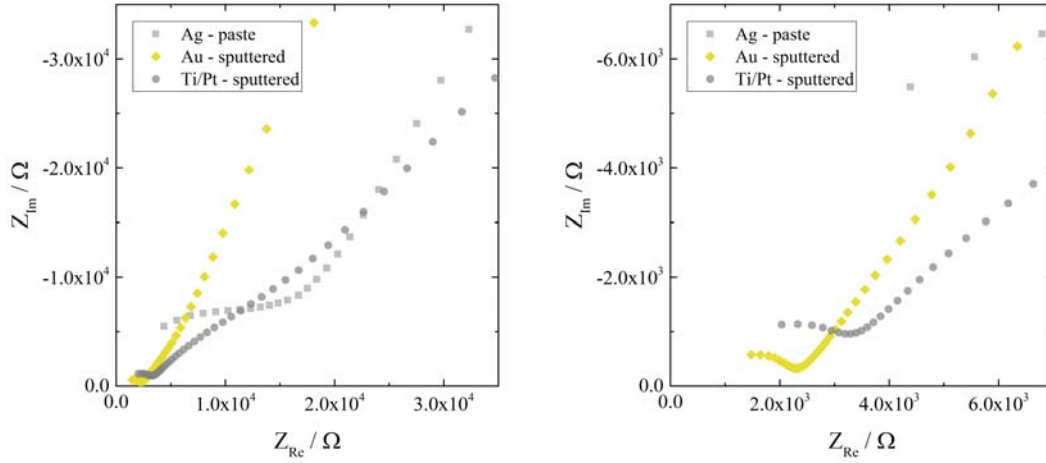


Figure 4.1: Impedance spectra of three samples (measured at 23.7 °C) for which pellets were pressed under different pressures to improve sample densification. No effect of the pressure on the final performance of the samples was found.

4.2 Macroelectrodes

4.2.1 Variations of pressure during sample preparation

With the intention to improve the density of samples, annealed LLZO powder was pressed to pellets under different pressures. The colleagues at University of Salzburg had an uniaxial press, but the maximum pressure they could apply was 1250 bar. Therefore, calcinated powder was sent to TU Wien to isostatically press pellets under different pressures to see whether this aids sample densification upon annealing. The geometry of all samples was similar, so just based on the impedance spectra shown in Figure 4.1 the absence of any significant effective conductivity differences can be concluded. Interestingly a pronounced second arc is found in these samples. Most likely the extra shipment between Salzburg and Vienna led to more pronounced degradation (LLZO powder is strongly affected by moisture), since samples were not stored under inert atmosphere. Based on the capacitance, the second semicircle might be attributed to grain boundaries,



(a) Impedance measurements at 23.9 °C - three different electrode materials (b) Enlargement of the high frequency range

Figure 4.2: Impedance spectra of an aluminium stabilized sample ($\text{Li}_{6.40}\text{Al}_{0.20}$) measured with different ionically "blocking" electrodes. The silver paste was not suitable as it lead to a high impedance in the bulk relaxation frequency range, compared to silver and gold.

which are rarely measurable if the whole sample preparation took place at the University of Salzburg. Accordingly, all other polycrystalline LLZO samples used in this thesis were completely prepared in Salzburg.

4.2.2 Optimization of electrode material

In search for an electrode material best suited for impedance measurements on polycrystalline LLZO samples, three options were tested: Au, Pt, Ag. Silver paste electrodes were brushed and as shown in Figure 4.2 a) the impedance in the high frequency arc is much larger compared to sputtered Au and Pt as electrodes. Probably residues from the organic solvent reacted at the interface and this hinders charge transport.

Sputtered Ti/Pt and Au layers were flat and dense. Both are highly inert and do not show indications of a highly resistive interlayer at the interface. Details on the interpretation of impedance spectra are given in Chapter 5.1. The shapes of both impedance spectra look rather similar, the key aspect is the separation between the high frequency bulk

part and the electrode contribution. Ideally, the response from the electrode is solely in the imaginary regime caused by a double layer capacitance of Li-ions and electrons at the electrode/electrolyte interface. Although the slope of Au sputtered electrodes is steeper than for Ti/Pt, neither electrode shows an ideal ion-blocking behavior. The Ti/Pt sputtered impedance spectrum also yields a small shoulder in the mid frequency range. The different slope and the additional shoulder might be attributed to the additional Ti-layer. Ti-targets were stored in ambient air and are therefore covered by an oxide layer. Before Ti is sputtered onto the sample, a preablation step is ushered to get rid of the TiO₂ layer. However, if this preablation step is not long enough TiO₂ is sputtered, which more likely intercalates Li-ions than a pure layer of gold. Moreover, some TiO₂ may also form after Ti sputtering.

Au as well as Pt are good electronic conductors, so differences of the high frequency bulk impedance are not expected for similar sample geometries. However, those measurements were upon the first samples measured in this thesis and back then the surface was polished mechanically by a diamond paste. The diamond paste partly contains water and therefore enhances the formation of LiOH which could form a passivating layer on top of the sample and thus increases the total impedance. Later on, samples were polished by hand using dry sandpaper.

The pivotal point in deciding which electrode material is more suitable to work with was the adhesion of Au and Ti/Pt. During lithography for microelectrode preparation, it is necessary to put the sample into a liquid, at least for a few seconds. If the adhesion of the electrode is bad, it detaches from the sample as soon as the sample is immersed in a liquid. Pictures of this phenomenon are shown in Figure 4.9. Sputtered Pt and Au without adhesion layer could be rubbed off by hand easily. Therefore, a thin layer of TiO₂ was sputtered to improve the adhesion of Pt. Alternatively, the adhesion of gold can be improved by chromium, however Ti/Pt yielded more stable results and was therefore chosen as the electrode material to work with.

4.3 Optimization of the macro-measurement set-up

4.3.1 Motivation for new set-up

Measuring LLZO at different temperatures allows to obtain the activation energy of electrochemical processes, here of the bulk conduction process. Analysis of this bulk conductivity requires separation of bulk and electrode impedance contributions. Information on the bulk impedance is only available at high frequencies and the required frequency range increases with increasing conductivity. In our case, samples are thus cooled to low temperatures, because heating would increase the peak frequency and as a result we lose information on the high frequency bulk semicircle. To maximize the measurable frequency range of the bulk contribution, the sample has to be cooled down as much as possible. The theoretical minimum of the used thermostat is -20°C . Due to a large distance between thermostat and measurement stage, the lowest temperature in our set-up was -7°C . Due to the condensation of water at lower temperatures, critical parts such as electric contacts and sample stage were protected by a flow of dry nitrogen. Typical bulk conductivities of Al stabilized LLZO are about $3 \times 10^{-4} \text{ S cm}^{-1}$. This conductivity can be well resolved within the used frequency range ($3 \times 10^6 - 10 \text{ Hz}$). Further on, cooling to lower temperature helped to nearly fully resolve the high frequency arc as can be seen in Figure 4.3 a). If the sample has a higher conductivity, however, (e.g. $6 \times 10^{-4} \text{ S cm}^{-1}$), only a few points are left from the high frequency semicircle at RT. An appropriate fit of the RT impedance spectrum shown in Figure 4.3 b) is hardly possible.

Still the visible high-frequency range improves upon cooling and by using the activation energy of the bulk process, the bulk conductivity (σ_{bulk}) at RT can be extrapolated. However, if σ_{bulk} is in the range of $10^{-3} \text{ S cm}^{-1}$, even lower temperatures have to be reached in order to obtain enough information on the first semicircle.

To improve cooling, the measurement stage was placed into a polystyrene box. The box could be closed and was equipped with an additional cooling system. The external cooling was provided via a silicon oil which was cooled down by fluid nitrogen. The improvements resulted in a new temperature minimum of -9.8°C . However, these im-

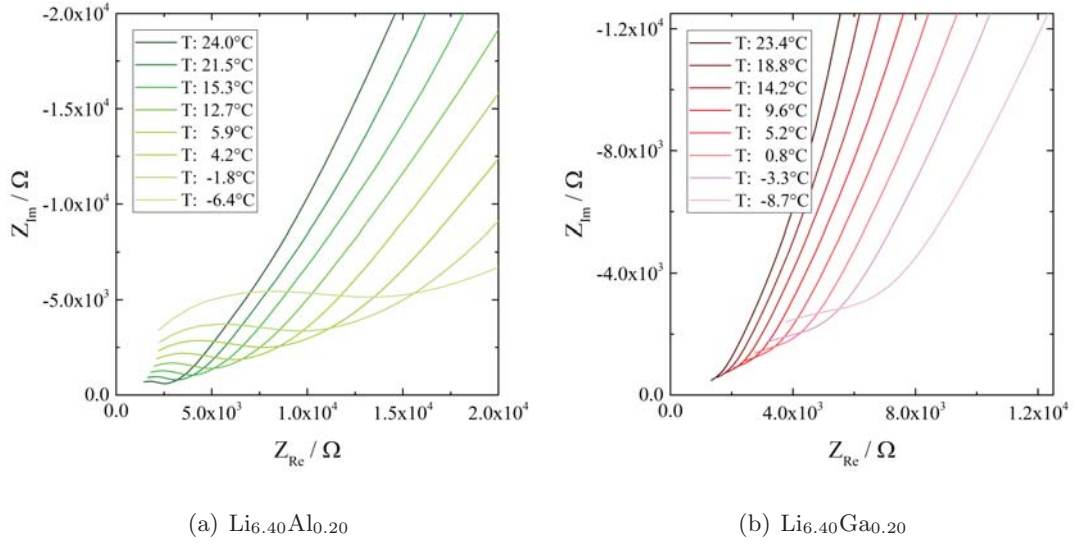


Figure 4.3: Temperature dependent impedance measurements on LLZO with a) $\text{Li}_{6.40}\text{Al}_{0.20}$ b) $\text{Li}_{6.40}\text{Ga}_{0.20}$. The impedance of the high frequency semicircle increases as the temperature drops. The conductivity of gallium stabilized LLZO is too high to resolve the high frequency semicircle even at low temperatures.

improvements still weren't sufficient to measure σ_{bulk} in the range of $10^{-3} \text{ S cm}^{-1}$. To overcome these issues, a completely new measurement setup was therefore planned, still using the thermostat as a source for cooling and heating.

4.3.2 Realization of improved macro-measurement set-up

Based on the experiences with the first measurement setup, the new setup should be improved in terms of cooling/heating efficiency and expanding the frequency range at which impedance data can accurately be measured.

Cooling efficiency

To reduce heat dissipation through pipes they were simply eliminated by placing the whole sample holder in the oil bath. The sample holder is covered by a tube of borosil-

icate glass. Based on these improvements, the new temperature minimum of the measurement setup is -12°C .

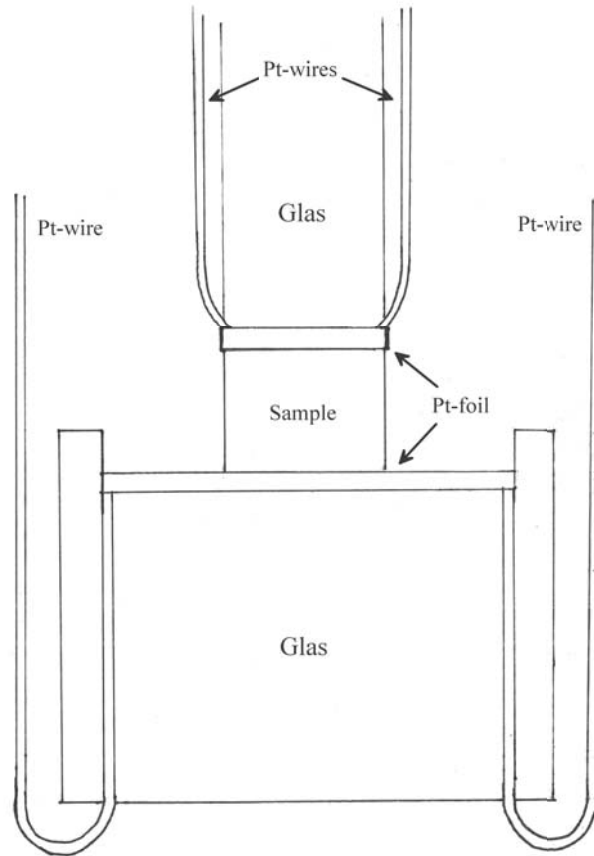


Figure 4.4: Sketch of the new samle holder.

Frequency range

In order to improve the precision for low impedance measurements, the measurement method was changed from a two point measurement to a "quasi" four point method. The four point measurement method allows to get rid of cable induced inductances and resistances. "Quasi" means that directly at the sample Pt-wires were connected to a Pt-foil as it is shown in Figure 4.4.

Besides influences from the measurement setup, also the Alpha-Analyzer has limits in

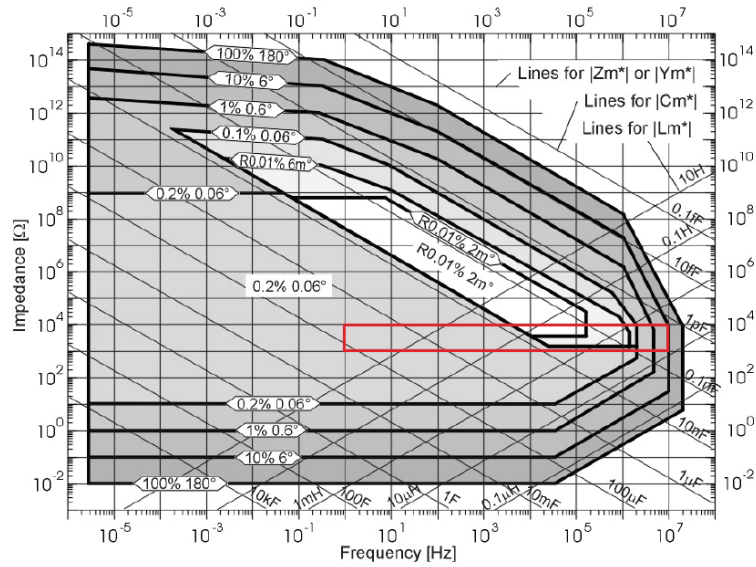


Figure 4.5: Accuracy specification of the impedance measurement. The red rectangle indicates region of interest when measuring LLZO.

measuring impedances. Novocontrol has defined different areas of accuracy based on parameters like capacitance, frequency and so on. Figure 4.5 is a sketch from the manual of a Novocontrol Alpha-A impedance analyzer. The area of interest for bulk measurements on LLZO is highlighted by a red rectangle. At 10^7 Hz the error of the total impedance is largest with $\pm 10\%$ and phase angle deviations of 6° .

Before impedance measurements can be started, the whole system has to be calibrated. Novocontrol provides three possibilities:

Reference calibration

This calibrates the current to voltage converter of a test interface and is used for sample impedances above $1 \text{ k}\Omega$. For LLZO samples, the impedance is mostly larger than $1 \text{ k}\Omega$ therefore this calibration is highly recommended to be done regularly and especially before low impedance and low capacitance calibrations. Measurements can be also performed without using the reference, however then the accuracy is limited to 0.2% and decreases especially at higher frequencies.

Low impedance calibration

This is necessary to calibrate the current to voltage converter to a sample impedance below 1 k Ω . In this calibration, properties of the measurement stage like wires and contacts are included. Before the calibration, the frequency range of interest has to be set. Then a 100 Ω resistor is attached into the measurement stage. A SMD (surface mounted device) resistor with an error of $\pm 1\%$ was used. Small silver plates were attached on both sides to ease contact between resistor and metal contacts from the measurement stage. For the last step of the calibration procedure, contact electrodes are short circuited. Afterwards, the calibration data can be used for further measurements. To determine the quality of calibration, the 100 Ω resistor can be measured in the desired frequency range and compared to a reference measurement from Novocontrol.

Low capacitance open calibration

This allows to eliminate stray capacities in the range of 30 fF, mostly caused by electrical parts. The capacitance of macro-samples, however, is about 3 orders of magnitude higher than the stray capacity, therefore the influence is negligible.

Calibration software

It is highly recommended to perform calibrations in WinDeta or any other software program provided by Novocontrol.

Figure 4.6 a) shows two impedance spectra of Ga 0.20 stabilized LLZO samples. Interestingly, although they are nearly equally conductive the resolution in the high frequency range is different. Impedance data from the red curve seem to be a bit shifted compared to the blue curve where the semicircle looks more ideal. The difference between these two samples is the thickness and as a result the bulk capacitance. The accuracy of impedance measurements significantly improves, if the capacitance of an investigated sample is larger than 20 pF. Therefore the sample geometry was optimized to surpass 20 pF by increasing the surface area and decreasing thickness. The change in capacitance is only 2 pF, therefore I suspect the improved accuracy is related to a change of a reference

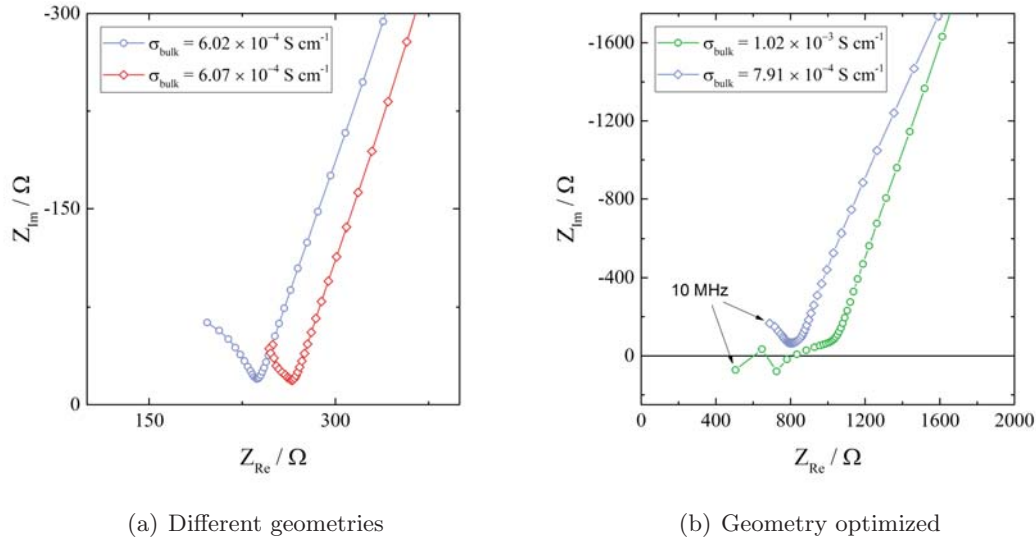


Figure 4.6: Impedance measurements on Ga 0.20 pfu stabilized LLZO samples at RT. a) Similar conductivities are found but the thick sample (red) can not be measured as accurate as the thin (blue) sample. b) Impedance spectra for optimized sample geometry by reducing thickness and extending the diameter.

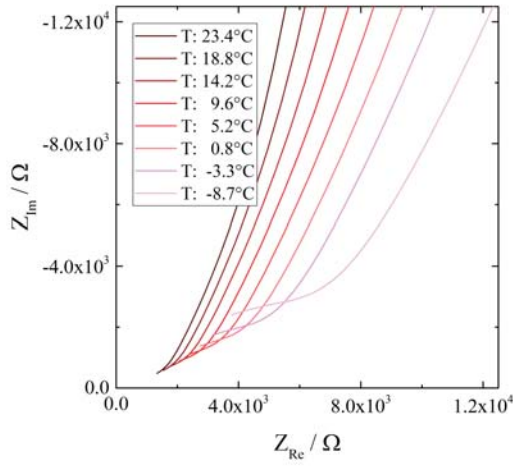
capacitor. WinDeta allows to select reference capacitors manually, however switching between different reference capacitors did not have an effect.

After calibrations and geometry optimizations were done, Ga 0.20 pfu stabilized LLZO samples could be measured and analyzed properly for the first time. Figure 4.6 b) shows the impedance spectra of two samples at RT, yielding typical conductivity values for this type of dopant. The first two points in the impedance spectrum of the higher conductive sample ($1.02 \times 10^{-3} \text{ S cm}^{-1}$) are not accurately measured, however the rest of the spectrum seems to be fine and allows an accurate fit.

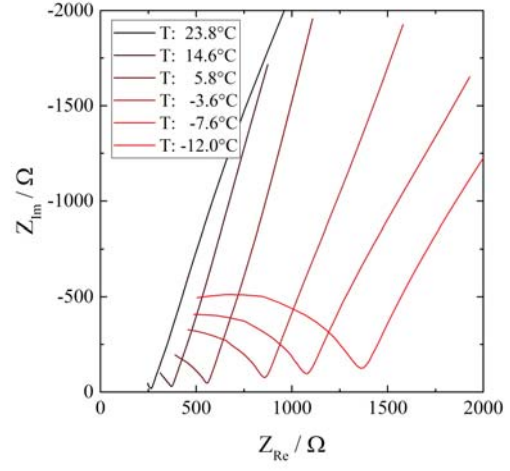
Figure 4.7 visualizes the improvements made by changing the measurement method and redesigning the measurement setup.

4.4 Microelectrodes

Local conductivities were measured by means of microelectrodes. Using photolithographic techniques in combination with ion beam etching, circular electrodes with di-



(a) Old measurement setup



(b) New measurement setup

Figure 4.7: Impedance spectra of Ga 0.20 pfu stabilized LLZO at different temperatures measured in the a) old measurement setup and b) new measurement setup.

ameters of 20 – 300 μm were prepared from the macroscopic Pt/Ti thin films on top of the samples. In the following, some details on the preparation procedure are given.

Sputtering

Before sputtering, samples were polished and cleaned by a flow of nitrogen to keep the surface as clean as possible. To avoid contaminations from sputter targets, a preablation step was performed. 10 nm of Ti and 200 nm of Pt were then sputtered. If the surface were ideally flat, also thinner layers might be sufficient. However, intraparticle porosity and the inability to use mechanical grinding machines (to avoid water) resulted in a "hilly" surface. The idea behind sputtering 200 nm was to fill up potential craters and establish a dense and connected Pt thin film.

The adhesion quality of sputtered layers can be easily determined by trying to rub off the electrode. If the electrode is well attached nothing will happen.

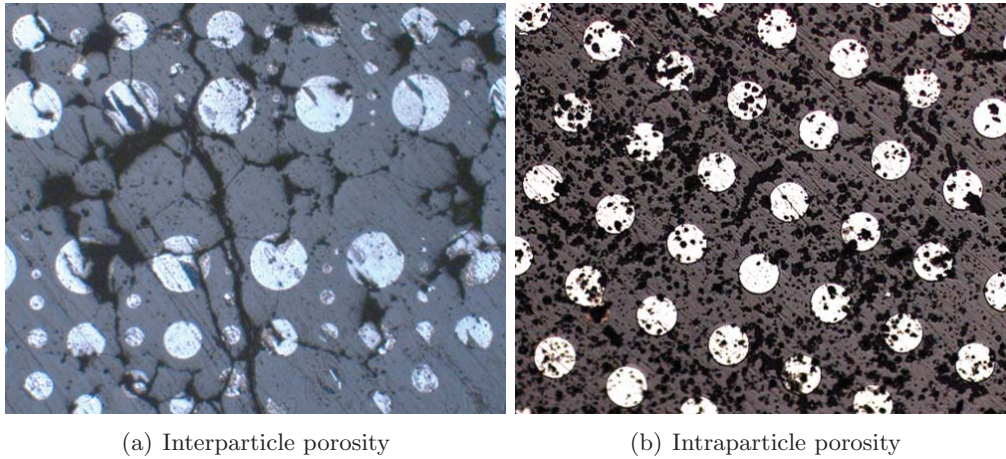


Figure 4.8: a) Interparticle porosity - large gaps between the grains. b) Intraparticle porosity - excavations on top indicated by dark spots.

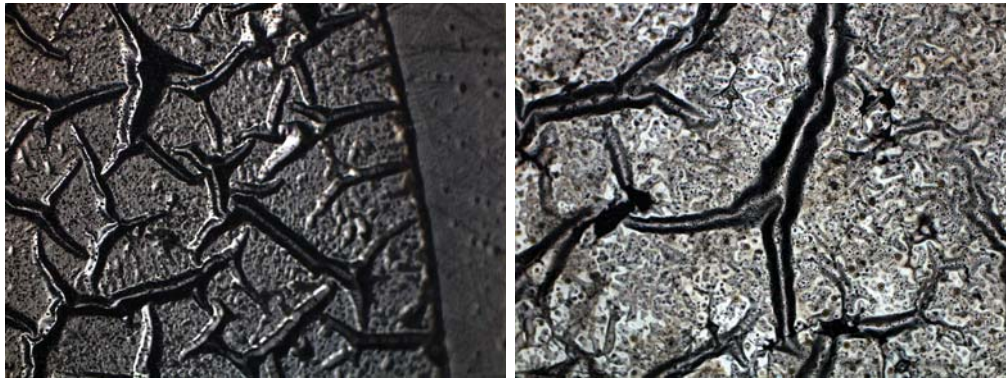
Lithography

When it comes to prepare microelectrodes on LLZO samples, four major steps can be distinguished:

1. Application of the photoresist on a spin coater (100 ml, 50 rps for 25 s)
2. Hardening the photoresist on a heating plate (100 °C - 2 min)
3. Shadow mask and sample are placed under an UV-lamp (40 sec)
4. Developer removes photoresist of non illuminated areas (\approx 30 s)

The first step is to apply a layer of photoresist onto a sample, therefore an acceptable sample density is required. At the beginning of the project, intergranular porosity was a major concern (Figure 4.8 a). Dense layers could not be sputtered on top and therefore photoresist could flow into the gaps. Under these circumstances, microstructuring the electrode is nearly impossible. However, as the density could be increased within the corresponding project the problem was more or less solved.

Besides the intergranular porosity, there is also the intraparticle porosity. Gas filled inclusions within a grain are formed during sintering and are responsible for the crater-rich surface (Figure 4.8 b). These inclusions show up upon grinding and are a major



(a) Sample immersed in water

(b) Veins filled with water

Figure 4.9: a) As soon as a sample is immersed in water, intermediate spaces are filled with it. b) The enlarged picture reveals vein like structures, preferably formed at grain boundaries, lifting the Ti/Pt layer.

issue when it comes to the preparation of microelectrodes. In Figure 4.8 b) a lot of microelectrodes have black dots. These spots are small holes caused by small holes on the surface interrupting the sputtered metal layer. As long as size and number of these black dots remain small within a microelectrode, impedance measurements still yield reasonable results.

Hardening the photoresist and applying UV-light is rather straightforward. The last step is to develop the photoresist. Therefore, the sample is immersed in a developer solution, which solves the parts of the photoresist not affected by the UV-light. To stop the developer from working, the sample is immersed in water for a short period of time (1-2s). As water likes to react with LLZO it is advisable not to remove the thin Ti/Pt layer at the side of the sample as it acts like a protection layer against water and can be used later on to contact the counter electrode.

When the sample is immersed in water or the developer solution, one can immediately observe whether the Ti/Pt layer is well attached to the surface. If not, vein like structures will start to form, as shown in Figure 4.9. Most likely empty intermediate spaces between sample and electrode are filled up with a liquid and lift off the Ti/Pt layer. The structural integrity of the layer is therefore compromised and won't sustain the next process steps. The best solution here is to start all over again.

An exact reason behind this phenomenon can not be given. From my experience the rate of success is higher if the time between polishing, sputtering and lithography is minimized as much as possible. However, if the interparticle porosity is too high, those vein like features will always occur and undermine the metal layer on top. Basically the time the Ti/Pt layer can sustain the developing process is limited. After one minute immersed, the metal layer will most likely detach from the sample.

Another method to prepare microstructures is called "lift-off". In this case, microstructuring is done before electrodes are sputtered on top. However, due to the rough surface and adsorbates like LiOH and Li₂CO₃, this kind of microstructuring was not possible for our LLZO samples.

Ion beam etching

The last step in preparing microelectrodes was the ion beam etching. Ti/Pt layers uncovered by photoresist should be removed after 20 minutes (Beam 3 kV, Extractor 3 kV, $I_{\text{multi}} \approx 2.4 \text{ mA}$). The remaining photoresist can be removed by acetone. In some cases the photoresist sticks rather strong to the microelectrodes. If so, one can try to simply apply more force when cleaning or looking if the contact needle can penetrate the layer of the photoresist anyway. It is not recommended to use the ultrasonic bath, as the sample is going to be degraded by Li⁺/H⁺ exchange reactions.

Chapter 5

Results and Discussion

5.1 The origin of conductivity variations in Al-substituted $\text{Li}_7\text{La}_3\text{Zr}_2\text{O}_{12}$ ceramics

5.1.1 Experimental

Large parts of this chapter are submitted to Solid State Ionics, 2017 [114].

Sample preparation

44 samples with nominal composition $\text{Li}_{6.40}\text{Al}_{0.20}\text{La}_3\text{Zr}_2\text{O}_{12}$ were investigated. The synthesis route is based on the procedure described by Wagner *et al.* [115]. Li_2CO_3 (99%, Merck), Al_2O_3 (99.5%, Aldrich), La_2O_3 (99.99%, Roth), and ZrO_2 (99.0%, Roth) were weighed to reach the intended stoichiometry. To compensate Li-loss during heat treatment, an excess of 10 wt % Li_2CO_3 was added with respect to the stoichiometrically required amount of Li_2CO_3 . The reagents were ground and mixed in an agate mortar under addition of isopropyl alcohol and subsequently pressed into pellets. The pellets were heated to 850 °C with a rate of 5 °C min⁻¹ and calcinated for 4 h. The resulting pellets were again ground in an agate mortar and ball-milled for 1 h under isopropyl alcohol (FRITSCH Pulverisette 7, 800 rpm, 2 mm ZrO_2 balls). After drying, the powder was pressed again into pellets and put into an alumina crucible. To avoid undesired incorporation of Al^{3+} from the crucible and to suppress evaporation of lithium from

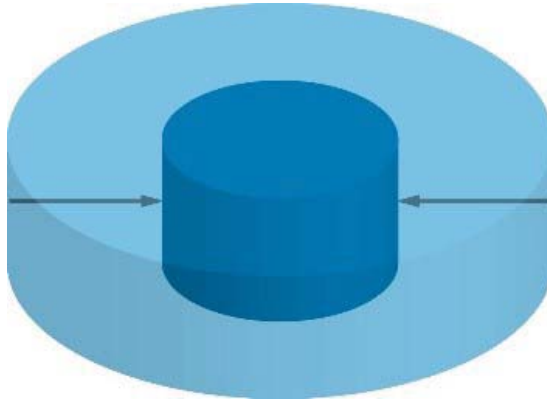


Figure 5.1: Schematic picture showing the diameter reduction by grinding. The thickness of the sample remains unchanged.

the sample, the actual pellets were always placed between two pellets of stoichiometric $\text{Li}_7\text{La}_3\text{Zr}_2\text{O}_{12}$. The final sintering step was performed under different conditions. Samples were heated with a rate of 5°C min^{-1} and either sintered at 1150°C for 12 h (10 samples) or at 1230°C for 6 h (34 samples). The resulting 44 samples had a diameter of 4.9 – 9.1 mm and a thickness between 0.9 – 2.0 mm. The density of the samples was measured by a He-pycnometer from Brand GmbH. Samples sintered at 1230°C showed a density of about 92 % and 1150°C lead to a density of 87 %. Phase analysis was performed by XRD experiments on a Panalytical X'Pert MPD with Cu K_α radiation [116]. The pattern was analysed with HighScore, a program provided by Panalytical. The 2θ scan range was between 5° and 120° with a step size of 0.026° .

Electrochemical impedance spectroscopy

The ionic conductivity of each sample was measured by electrochemical impedance spectroscopy (EIS). Samples were polished by SiC grinding paper (#4000) before thin films of Ti (10 nm) and Pt (200 nm) were deposited on top and bottom as ionically blocking electrodes, whereby Ti acts as adhesion layer for Pt. For the EIS measurements, a Novo-control Alpha Analyzer was used in the frequency range of $3 \times 10^6 - 10$ Hz with a rms amplitude of 100 mV. The temperature was controlled by a Julabo F-25 HE thermostat. A set temperature of 25°C lead to $T_{\text{eff}} = 25.2^\circ\text{C}$ measured by a thermocouple located near the sample. In order to investigate the conductivity of different sample areas, the

diameter of 10 samples was mechanically reduced step by step, using a SiC grinding paper (#500). The thickness was kept constant during the whole process, see Figure 5.1. After each diameter reduction step the conductivity was measured by EIS.

For laser ablation inductively coupled plasma mass spectrometry (LA-ICP-MS) a commercially available laser ablation system (New Wave 213, ESI, Fremont, CA) with a frequency quintupled 213 nm Nd:YAG laser and a fast-washout ablation cell was used. The laser ablation device was coupled to a quadrupole ICP-MS instrument (Thermo iCAP Qc, ThermoFisher Scientific, Bremen, Germany) using PTFE tubing. Data acquisition was performed using Qtegra software provided by the manufacturer of the instrument. For cell washout helium was used as carrier gas, which was mixed with argon make-up gas upon introduction into the plasma. Before each experiment, the measurement parameters concerning the MS instrumentation were optimized using NIST 612 trace metals in glass standard (National Institute of Standards and Technologies, Gaithersburg, MD) for maximum ^{115}In signal.

Sample ablation was carried out using line scan patterns with adjoining lines to scan the sample surface. A laser beam diameter of $60\ \mu\text{m}$ and a scan speed of $180\ \mu\text{m s}^{-1}$ were used for all documented imaging experiments in this study. In order to get the information of bulk regions, i.e. to avoid analysis of surface effects such as contamination or segregation of phases, a pre-ablation step consisting of a similar line scan pattern with a laser beam diameter of $250\ \mu\text{m}$ was carried out prior to the distribution measurements. Elemental distribution images were created from the recorded time resolved intensities for the measured isotopes using the software ImageLab (v.1.90, Epina GmbH, Pressbaum, Austria). To compensate instrumental drifts during measurement time and differences in material ablation, all recorded signals were normalized to the intensity of the isotope ^{90}Zr .

5.1.2 Results and Discussion

Conductivity measurements

Examples for impedance spectra of pristine LLZO samples, sintered at different temperatures and measured at $25.2\ ^\circ\text{C}$, are shown in Figure 5.2. Both impedance spectra show

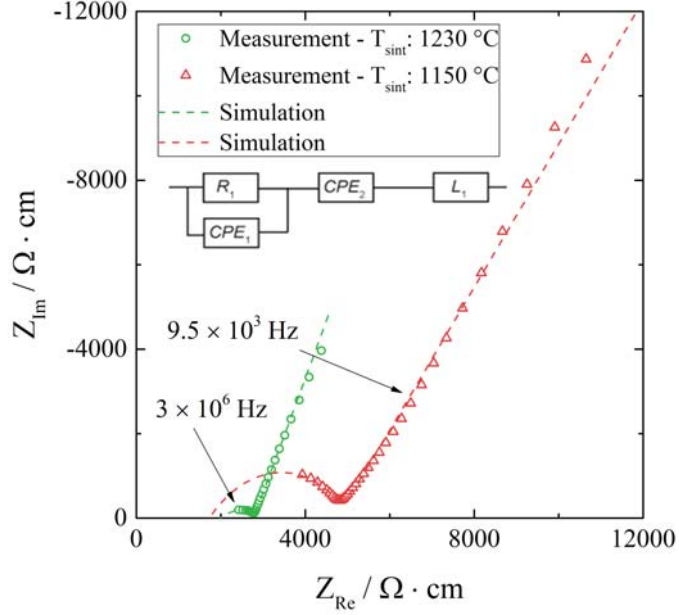


Figure 5.2: Impedance spectra of two Al-substituted LLZO samples prepared at different sintering temperatures, measured at 25 °C. The dashed spectra were simulated based on the equivalent circuit shown in the inset.

parts of a high frequency semicircle followed by a low frequency contribution coming from the ionically blocking electrodes (Ti/Pt). There is no indication of an additional arc due to grain boundaries or interface related effects. In agreement with earlier studies we attribute the high frequency feature to the ion conduction in the bulk [40]. To quantify the impedance spectra properly, a resistor in parallel to a constant phase element ($R_1 || CPE_1$) is used for the bulk contribution, followed by a CPE_2 element in series representing the blocking electrodes. Furthermore, an inductive element (L_1) has to be taken into account due to wiring. The equivalent circuit illustrated in Figure 5.2 leads to a reliable fit of the impedance spectra (dashed lines).

It has to be pointed out that the real axis intercept at high frequencies does not indicate an additional semicircle close to the origin but is simply caused by the inductance L_1 . Accordingly, the bulk conductivity (σ_{bulk}) was determined from R_1 by

Table 5.1: Calculated bulk conductivities, capacitances and permittivities, based on the fit data obtained by using the equivalent circuit shown in Figure 5.2.

T_{sint} [°C]	R_1 [Ω]	σ_{bulk} [S cm^{-1}]	CPE_1 [pF s^{n-1}]	n_1	C_1 [pF]	ϵ_r
1230	1352	3.6×10^{-4}	43.3	0.92	1.23	68
1150	1385	2.2×10^{-4}	95.3	0.89	1.36	47

$$\sigma_{\text{macro}} = \frac{h}{A \times R_1} [\text{S cm}^{-1}] \quad (5.1)$$

with A as the sample area and h representing the sample thickness. Table 5.1 shows the fit data for the two spectra in Figure 5.2, including the conductivity and also the relative permittivity ϵ_r , which was calculated from the sample capacitance [117]

$$C_1 = (R_1^{(1-n)} CPE_1)^{\frac{1}{n}} \quad (5.2)$$

The ϵ_r value is within the expected range for the LLZO bulk, which supports our interpretation of the high frequency arc in terms of a bulk property [118].

Effective conductivities of 34 samples sintered at 1230 °C

34 nominally identical LLZO samples with an Al content of 0.20 pfu sintered at 1230 °C were investigated by EIS. In Figure 5.3 the measured bulk conductivities of the samples in their pristine state (before diameter reduction) are shown. The variation in conductivity of pristine samples covers almost two orders of magnitude. A trend, whether bulk conductivity increases or decreases with ongoing sample production is not observable. Clearly some changes can be attributed to specific batches (samples sintered at the same time in the oven) which resulted in very high or very low conductivities. However, even if we consider conductivities lower than $5 \times 10^{-5} \text{ S cm}^{-1}$ as an exception rather than the rule, the variations are still very pronounced. These variations may be related to the poorly controllable loss of lithium during sintering and its effect on the other cations and the anions. Laser induced breakdown spectroscopy (LIBS) has already shown

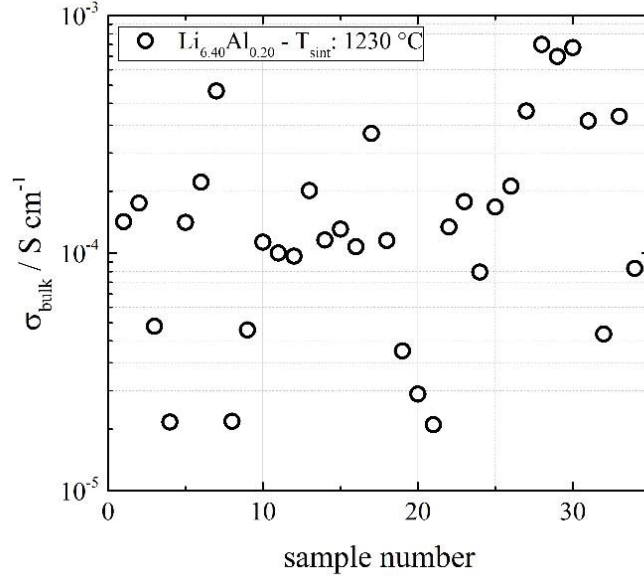


Figure 5.3: The ionic bulk conductivities of samples prepared by nominally identical preparation route, measured at 25 °C, vary over two orders of magnitude. (Experiment 1)

the existence of an inhomogeneous elemental distribution near the surface [119]. Here however, larger sample parts have to be affected, because effective sample conductivities vary distinctly.

Effect of sintering temperature

To investigate the effect of the sintering conditions on the overall performance, 10 samples were manufactured and sintered at 1150 °C in parallel to the last batches of 14 samples sintered at 1230 °C. Conductivity measurements showed the same picture as in Figure 5.2, a large scatter in conductivity was observed, regardless of sintering conditions (Figure 5.4). Even though the highest conductivities were reached for samples sintered at 1230 °C, the conductivity of samples sintered at 1150 °C is also partly far above average ($> 5 \times 10^{-4} \text{ S cm}^{-1}$), despite their lower density. Hence, we conclude that the substantial scatter is not caused by more Li evaporation at higher sintering temperatures (except possibly for the samples with very low ionic conductivities).

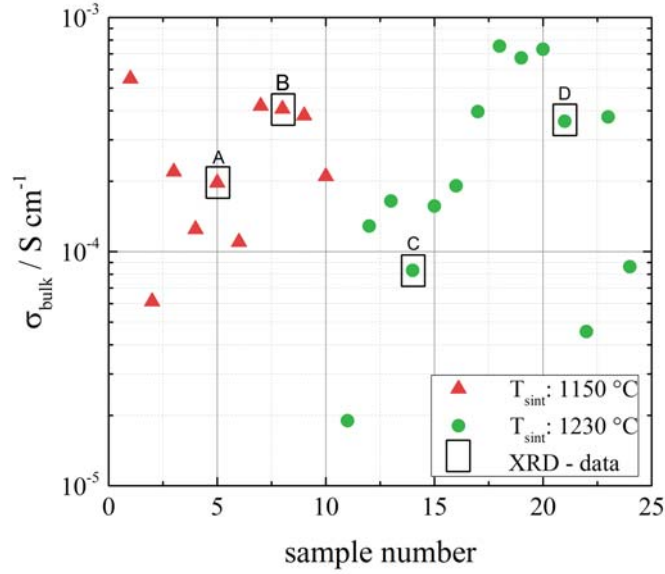


Figure 5.4: Bulk conductivities of samples sintered at 1150 °C (red) and 1230 °C (green). For both sintering temperatures, the conductivity values scatter strongly. (Experiment 2)

Influence of sample size reduction on the ionic conductivity

Ten randomly selected samples from experiment 2 were used to continue the investigation about the influence of inhomogeneities on the ionic conductivity. The sample diameter was gradually reduced by grinding, as sketched in Figure 5.1. As expected, the reduction leads to an increase in the overall impedance. In most cases, however, also the effective ionic conductivity changed significantly. For example, the effective conductivity of one sample (sintered at 1150 °C) drops from $\sigma_{\text{start}} = 2.2 \times 10^{-4}$ to $\sigma_{\text{end}} = 8.8 \times 10^{-5} \text{ S cm}^{-1}$, indicating inhomogeneous conduction within a single sample. In this case it means that the remaining central part is less conductive than the whole sample average of $2.2 \times 10^{-4} \text{ S cm}^{-1}$. The trends of the conductivity changes upon diameter reduction by grinding for all 10 samples are summarized in Table 5.2.

Detailed parameters of four exemplary samples are displayed in Figure 5.5. Samples sintered at 1150 °C (red) show lower conductivities after each geometric reduction step, indicating that the peripheral parts of the sample show a higher conductivity than the

central parts. For the seven samples sintered at 1230 °C the situation was less clear, as in one case the conductivity even increased with size reduction and reached exceptional high values of $7.55 \times 10^{-4} \text{ S cm}^{-1}$ for Al-stabilized LLZO (Figure 5.5).

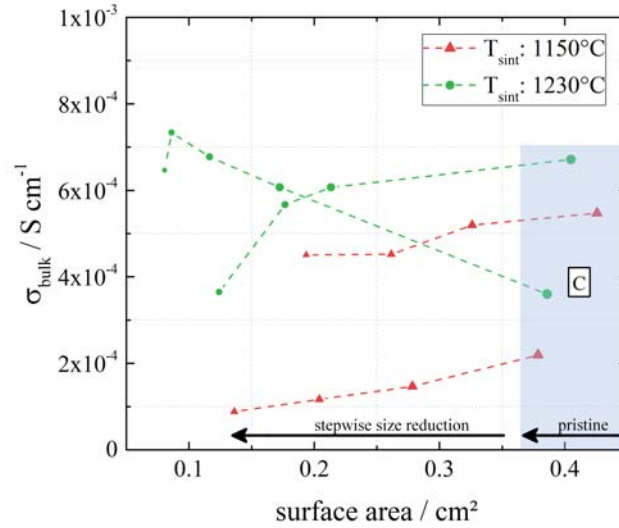


Figure 5.5: Development of conductivity upon systematic diameter reduction of the samples by grinding. In all displayed cases the conductivity changes.

From the measured resistances before R_1 and after R_2 size reduction, the conductivity of the removed part can be approximated by

$$\sigma_{\text{removed}} = \left| \frac{1}{R_1} - \frac{1}{R_2} \right| \times \frac{d}{A_1 - A_2}. \quad (5.3)$$

For some removed regions, the calculated conductivities resulted in more than $10^{-3} \text{ S cm}^{-1}$, indicating that sample conductivities of $7.55 \times 10^{-4} \text{ S cm}^{-1}$ are still not the limit for Al stabilized LLZO samples.

The existence of highly conductive sample parts raises the question of the origin of high and lower conducting regions within one and the same LLZO sample.

Four $\text{Li}_{6.40}\text{Al}_{0.20}\text{La}_3\text{Zr}_2\text{O}_{12}$ samples named as A, B, C, D in Figure 5.4 were therefore investigated in terms of inconsistencies in present phases, phase composition, and struc-

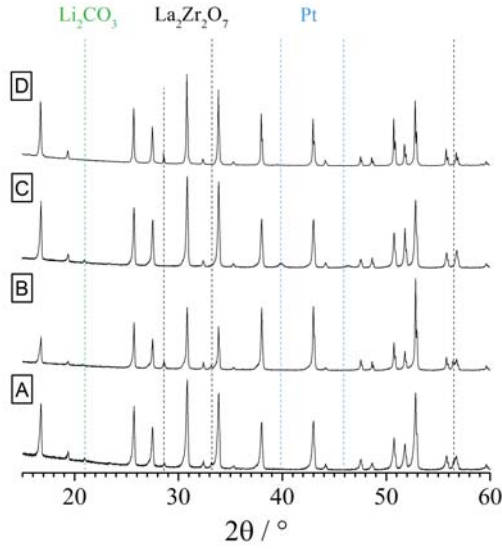


Figure 5.6: XRPD patterns of samples, sintered at 1150 °C (A, B) and 1230 °C (C, D). Dashed lines indicate the position of impurity phases such as Li₂CO₃, La₂Zr₂O₇ and Pt (from electrode). Letters (A, B, C, D) refer to the samples in the conductivity plot in Figure 5.4.

Table 5.2: Trends in conductivity upon diameter reduction by grinding. Green – increase, grey – constant, red – decrease in conductivity.

Sinter temperature	1150 °C	1230 °C
Conductivity trend	↓↓↓	↓↓↓↑ / / ↓

ture as possible reasons (see Figure 5.6). All samples show reflexes indicating cubic garnet structure and small contents of Li₂CO₃ and La₂Zr₂O₇, which are common extra phases of LLZO. In addition, reflexes of platinum coming from the electrode are observed. Significant differences between XRPD patterns of high and low conductive samples, however, are not found, suggesting that unintended compositional differences rather than second phases may play an important role.

It is beyond the scope of this study to finally resolve this, however, preliminary results on the elemental distribution of an Al-substituted LLZO sample, measured by LA-ICP-MS, indicate a possible correlation.

Morphological, chemical, and compositional analysis

After size reduction, the remaining part of a sample (C) was investigated by spatially resolved LA-ICP-MS. As presented in Figure 5.5, the sample showed an increased conductivity in the central region. Figure 5.7 illustrates the cross section of the pristine sample as well as the elemental distribution of Li, La, and Al. To compensate differences in material ablation and instrumental drifts during measurement time, all intensities were normalized to the Zr signal. It can be assumed that Zr is evenly distributed within the samples since in contrast to Li changes of the Zr content during the sintering caused by evaporation is very unlikely to occur.

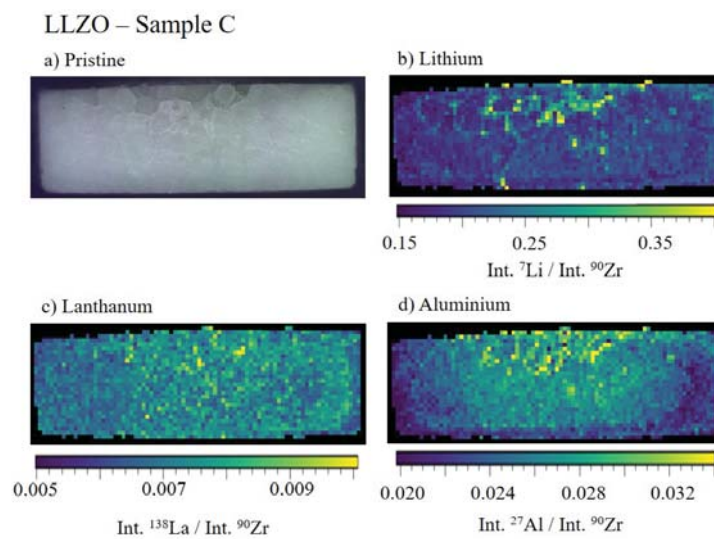


Figure 5.7: LA-ICP-MS measurements on an Al stabilized LLZO sample sintered at 1230 C. Letter C references to the same sample as marked in Figure 5.4, Figure 5.5 and Figure 5.6. After size reduction, the sample was cut into two pieces and the distribution of b) lithium, c) lanthanum and d) aluminium is shown normalized on the zirconium signal.

Although exact quantification is not possible without suitable reference materials, this method enables the determination of local variations of the chemical composition. Li, and La have a rather homogenous distribution, whereby the outer rims and the bottom of the remaining sample seems to contain about 25 % less Al (darker colour) compared to the centre part. Since Al occupies Li-sites, the varying Al content should be linked

to variations of the Li content. No such correlation is observable, but this might be due to the relative differences being below the precision of the method. These measurements indicate that local variations of the Al content may play an important role in understanding the large scatter of conductivity data. A proceeding study will further investigate the effect of these elemental variations on the ionic conductivity analyzed by microelectrode impedance spectroscopy [120].

5.1.3 Influence of sample's height

In the beginning of this project, the geometry of the samples was not considered to be a relevant parameter in order to optimize their overall performance. So the height of LLZO samples varied between 1 and 5 mm. In Figure 5.8 the pristine bulk conductivity of 50 samples is plotted over their height. Samples are divided into thick (> 2.75 mm) and thin (< 2.75 mm). Although the amount of thick samples (17) is smaller than for thin samples (37), it can still be concluded that much less samples show a very low conductivity.

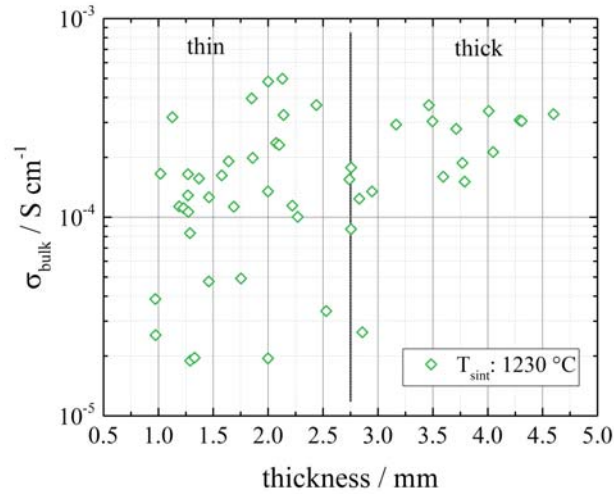


Figure 5.8: The effective ionic conductivity at room temperature of different samples, correlated with their height. Samples were divided into two groups: thin and thick (> 2.75 mm) samples.

To further investigate this phenomenon, thick samples (0.36 - 0.41 mm) were prepared

under different conditions regarding temperature and duration. Detailed values on sintering conditions and density are listed in Table 5.3.

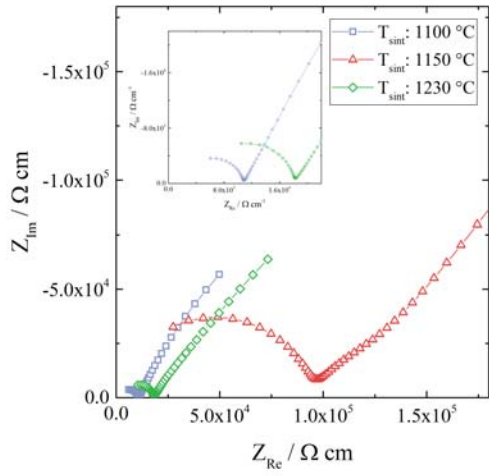
Table 5.3: Sinter conditions and density of newly prepared thick samples.

Temperature [°C]	Duration [h]	Density	Conductivity trend
1100	17	-	↓↓↓↓
1150	12	81 %	↓↓↓
1230	6	87 %	↓↓↓ /

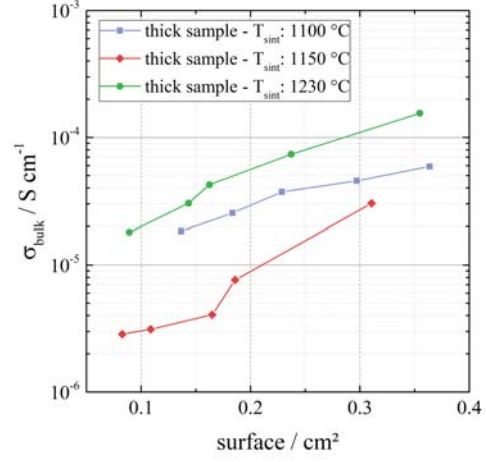
In their pristine state, samples looked optically dense and without second phases. There were no signs of large voids or cracks, the only difference was the color of the samples sintered at 1150 °C, which was bright yellow. Impedance measurements were performed at 25.1 °C, see Fig. 5.9 a). The high frequency contribution, attributed to the bulk, is followed by a response from the electrodes. One impedance spectrum yielded a small shoulder after the first semicircle (1150 °C - red) which is possibly due to grain boundaries. Impedance spectra were fitted, based on the equivalent circuit shown in Figure 5.2 a). The bulk conductivity of each sample was rather low, ranging between 3.0×10^{-5} and $1.6 \times 10^{-4} \text{ S cm}^{-1}$.

In order to analyze the samples in terms of their spatially homogeneous conductivity, the diameter was reduced systematically by grinding, similar to the measurements described above. The systematic removal of peripheral parts led to pronounced losses in effective ion conductivity. Figure 5.9 b) shows the development of σ_{bulk} upon size reduction. After each geometric reduction the measured effective ionic conductivity became lower, indicating that the peripheral parts were better conducting than the central parts.

The final state of the samples partly revealed the reason behind these variations. Figure 5.10 shows the remaining parts of samples sintered at a) 1100, b) 1150 and c) 1230 °C. Panel a) shows canyon like structures in the core of the sample, so the ionic conductivity had to become worse upon the size reduction. Also the sample sintered at 1230 °C shows a brown stain and an undefined phase. Interestingly the samples sintered at 1150 °C did not show any kind of structural flaws, despite their slightly different color. After the grinding experiments, electrodes were removed and the sample was investigated by



(a) Nyquist-plot



(b) Geometric reduction

Figure 5.9: a) Nyquist plot of thick samples, prepared by different sintering temperatures, measured at 25.1 °C. b) Development of conductivity upon systematic diameter reduction of the samples by grinding. In all displayed cases the conductivity dropped.

XRD to test if those non-idealities could have been seen right from the beginning. Each of the investigated samples showed reflexes indicating a cubic LLZO structure and some secondary phases (LiOH, $\text{La}_{0.18}\text{Zr}_{0.82}\text{O}_{1.91}$, Pt - electrode material). However, it was not possible to detect these inhomogeneities within the pristine sample by XRD probably because the X-ray source is too weak and so the penetration depth too short (Cu - $\text{K}\alpha \approx 5 \mu\text{m}$).

It can be concluded that the preparation of thick samples did not improve the overall performance due to the formation of holes, porosity, etc. Reasons, behind these phenomena are unknown yet. Possibly areas near the core are partly exposed to different temperatures or chemical potentials than peripheral parts. These differences lead to compositional gradients, forming irregular structures inside and the intended cubic structure on the outside. Although these deviations can not be detected by Cu - $\text{K}\alpha$ radiation, they should be detectable by density measurements.

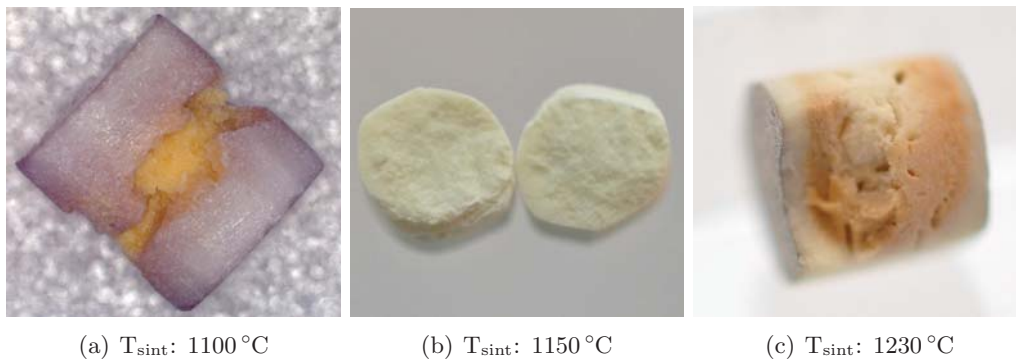


Figure 5.10: Morphological effects found within thick samples upon systematic removal of peripheral parts, explaining their low overall performance and their significant conductivity loss upon size reduction.

5.1.4 Conclusion

Numerous Al-substituted LLZO samples with identical Al contents were prepared by a nominally identical solid state route and sintered at 1150 °C and 1230 °C, respectively. In the best case, effective sample conductivities near $8 \times 10^{-4} \text{ S cm}^{-1}$ were obtained, which is among the highest values ever reported for Al stabilized LLZO. In other cases, effective values with less than $10^{-4} \text{ S cm}^{-1}$ were found. XRPD measurements could not resolve reasons for these variations.

The diameter of several samples was changed by grinding and the samples were repeatedly analysed using EIS, which revealed pronounced spatial inhomogeneities in the ionic conductivity. In most cases the peripheral parts showed higher conductivities and we suspect a gradient in the distribution of elements to be responsible for the inhomogeneities in ionic conductivity. This assumption is supported by elemental distribution images, obtained by LA-ICP-MS, which revealed an Al gradient. Unintended changes of the composition during preparation may thus also be the reason for large variations of the effective ionic conductivity of nominally identical LLZO samples.

5.2 The temperature dependent conductivity of LLZO with different composition

In addition to the detailed investigation of sample conductivities for LLZO stabilized by Al (0.20 pfu), many other LLZO compositions with numerous different stabilizing ions were measured, mostly at different different temperatures. Spectra looked very similar to those presented in chapter 5.1 and impedance analysis was done in the same manner. In this chapter, all results are summarized.

Table 5.4: An overview of bulk conductivity (σ_{bulk}), relative permittivity (ϵ_r) and activation energy (E_a) of LLZO samples with different compositions. The given conductivity value (σ_{bulk}) refers to measurements at T_{set} : 25 °C. Elements with a reference number are further discussed in a publication.

Aluminium					Gallium				
[pfu]	σ_{bulk} [S cm ⁻¹]	ϵ_r	E_a [eV]		[pfu]	σ_{bulk} [S cm ⁻¹]	ϵ_r	E_a [eV]	
0.10	3.78×10^{-5}	43	-		0.15	6.49×10^{-4}	-	0.14	
0.15	2.08×10^{-4}	66	0.42		0.20	1.02×10^{-3}	57	0.34	
0.20	1.58×10^{-4}	37	0.43		0.30	9.04×10^{-4}	73	0.31	
0.30	2.50×10^{-4}	58	0.37		0.40	4.34×10^{-4}	61	0.28	
0.40	1.14×10^{-4}	47	0.41						

Aluminium & Gallium [98]

[pfu]	σ_{bulk} [S cm^{-1}]	ϵ_r	E_a [eV]
0.05 & 0.15	1.06×10^{-3}	-	0.26
0.10 & 0.10	6.30×10^{-4}	-	0.28
0.15 & 0.05	3.80×10^{-4}	-	0.28

Molybdenum - pristine [40]

[pfu]	σ_{bulk} [S cm^{-1}]	ϵ_r	E_a [eV]
0.10	7.78×10^{-5}	44	0.46
0.20	2.81×10^{-4}	59	0.48
0.25	2.20×10^{-4}	46	0.44
0.30	2.94×10^{-4}	68	0.52
0.40	3.30×10^{-4}	52	0.43

Niobium

[pfu]	σ_{bulk} [S cm^{-1}]	ϵ_r	E_a [eV]
0.125	1.06×10^{-4}	80	1.08
0.250	2.56×10^{-4}	45	0.49
0.375	4.67×10^{-4}	39	0.50
0.500	6.72×10^{-4}	82	0.53
0.625	1.36×10^{-4}	116	0.53
0.750	4.87×10^{-5}	72	0.62
1.000	2.05×10^{-4}	45	0.47
1.250	1.35×10^{-4}	69	0.66
1.500	6.48×10^{-5}	46	0.61
1.750	3.14×10^{-4}	46	0.50
2.000	2.81×10^{-5}	49	0.63

Tantalum

[pfu]	σ_{bulk} [S cm^{-1}]	ϵ_r	E_a [eV]
0.25	4.63×10^{-4}	40	0.49
0.50	4.31×10^{-4}	-	0.38
0.75	-	-	-
1.00	2.14×10^{-4}	70	0.45
1.25	1.23×10^{-4}	31	0.52
1.50	9.36×10^{-5}	46	0.52
1.75	6.18×10^{-5}	44	0.69
2.00	5.27×10^{-5}	53	0.78

Tetragonal LLZO (Chapter 5.3)

[pfu]	σ_{bulk} [S cm^{-1}]	ϵ_r	E_a [eV]
-	7.54×10^{-7}	49	-

Single crystal - Tantalum (Chapter 5.4)

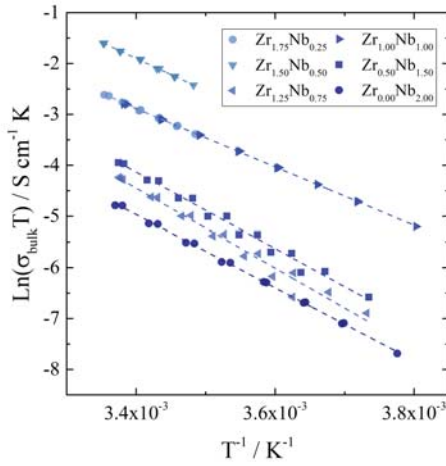
[pfu]	σ_{bulk} [S cm^{-1}]	ϵ_r	E_a [eV]
1.00	1.69×10^{-4}	48	0.53

Iron [121]

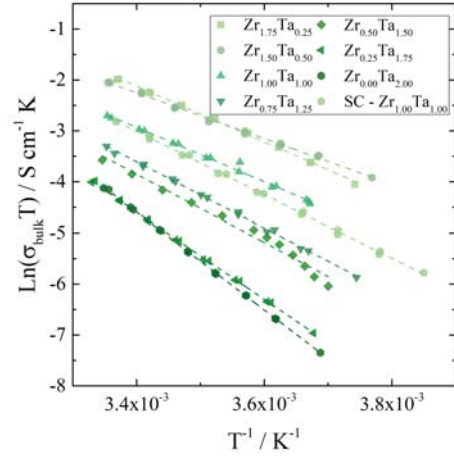
[pfu]	σ_{bulk} [S cm^{-1}]	ϵ_r	E_a [eV]
0.18	9.35×10^{-4}	55	0.31
0.20	2.65×10^{-4}	-	0.45
0.25	1.38×10^{-3}	80	0.30

Bismut [113]

[pfu]	σ_{bulk} [S cm^{-1}]	ϵ_r	E_a [eV]
0.25	3.35×10^{-4}	60	0.50
0.50	3.31×10^{-4}	64	0.50
0.75	4.19×10^{-4}	69	0.47



(a) Niob



(b) Tantal

Figure 5.11: Arrhenius graph of a) Nb and b) Ta stabilized LLZO samples with different compositions. SC denotes the single crystal.

Table 5.4 lists numerous LLZO ceramics with different compositions, their bulk conductivity, relative permittivity and activation energy. Some compositions are marked with references to a certain chapter of this thesis or a publication for further information. The listed values do not necessarily represent the best conductivity, since in many cases only one sample was investigated at different temperatures. The relative permittivity was always calculated based on the impedance spectrum measured at the lowest temperature, since more information on the first semicircle was available.

Nb and Ta are two elements for which conductivities around $10^{-3} \text{ S cm}^{-1}$ have already been published in literature [90, 122]. These values could not be achieved in this study. The highest bulk conductivity was found for Nb 0.50 pfu with $6.72 \times 10^{-4} \text{ S cm}^{-1}$. For Ta stabilized LLZO, from literature the highest conductivities were expected for Ta 0.6 pfu, unfortunately a successful preparation of such a sample was not possible. Figure 5.11 shows the Arrhenius graph for different compositions of a) Nb and b) Ta stabilized LLZO samples. Temperature cycles between 25 and -6°C were usually measured three times. For a better overview, only the last measurement cycle and a few compositions are displayed. Also data for the Ta stabilized single crystal are included and the conductivities are very similar to those of the polycrystalline sample with the same composition.

Measurements on Bi stabilized LLZO samples have to be considered critically. The listed bulk conductivities are obtained from impedance measurements on newly prepared samples. However, the overall performance started to decrease due to storage in ambient air. As it turned out, Bi stabilized LLZO is highly reactive against moisture and therefore not suitable for further battery related applications. Further information can be found in the publication of Wagner *et al.* [113].

5.2.1 Mid-frequency contributions

Some samples yielded a second semicircle in the mid-frequency range, for example some Mo or Al stabilized LLZO. Fig. 5.12 shows two impedance spectra measured at a) 23.4°C and at b) -6.6°C . Near room temperature a second semicircle becomes visible, but as both semicircles overlap an accurate fit is rather difficult. Cooling down to lower

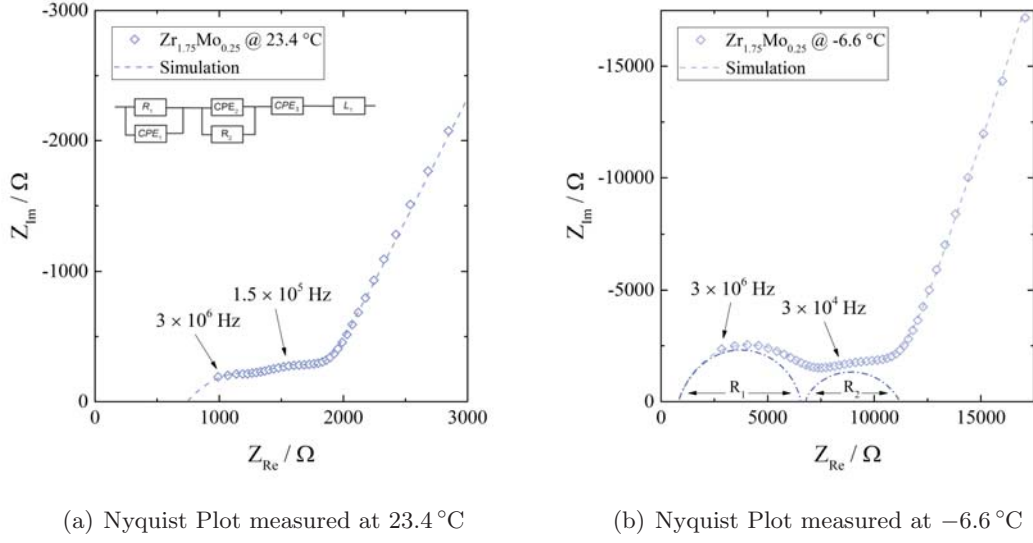


Figure 5.12: Impedance measurements on Mo stabilized LLZO at a) 23.4 °C and b) -6.6 °C. The second semicircle can only be separated at low temperature.

temperatures better reveals the first arc and separates these two semicircles and as a result the fit quality improves. An additional $R_2||CPE_2$ element has to be added (Figure 5.12 a) to the equivalent circuit used for other spectra.

In order to investigate the origin of this semicircle, parts of the sample are removed by sand paper and the electrodes are renewed on both sides. Measuring the impedance lead to changes in the second semicircle, the peak frequency however didn't shift, indicating the resistive region is not exclusively located near the interface. A calculation of the corresponding thickness (d_2), using the capacitance C_2 and the bulk permittivities, lead to values between 10 and 20 μm . Such effects could be more accurately analyzed when using reversible electrodes, as ionically blocking electrodes tend to overlap with the intermediate frequency arc.

If R_2 is the grain boundary resistance, the grain boundary thickness δ_{gb} can be calculated by

$$\delta_{\text{gb}} = \frac{d_2 L_g}{d} \quad (5.4)$$

with L_g as the grain size length and d the sample thickness. The resulting thickness of a grain boundary is approximately $1 \mu\text{m}$. This is significantly larger than typically found for oxides (in the range of nm) and grain boundary effects are considered as not very probable. An explanation could be the formation of second phases over time, due to water incorporation from ambient air.

Annealing

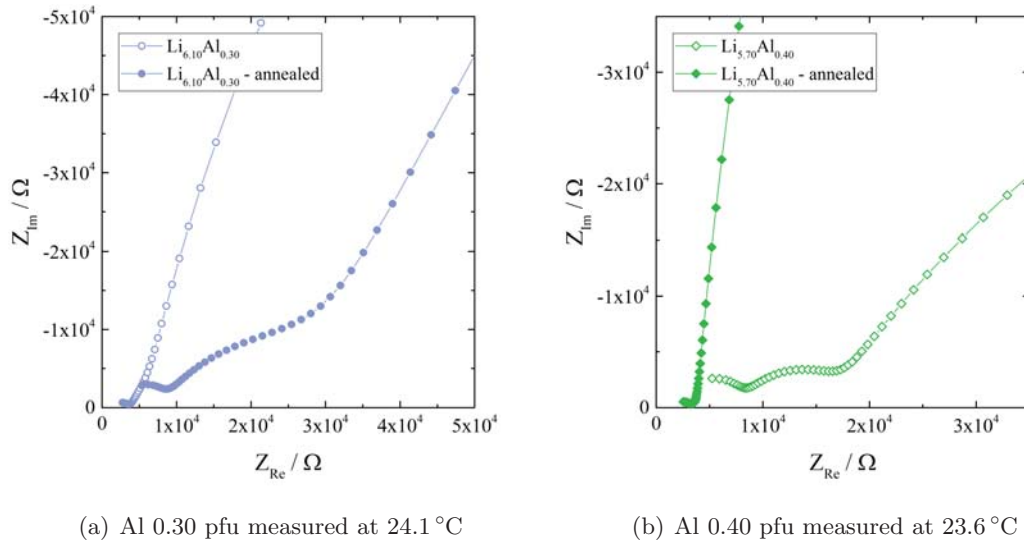


Figure 5.13: Impedance spectra of Al stabilized LLZO were measured before and after heat treatment at room temperature. a) Annealing reduces the size of the second semicircle, for b) Al 0.40 pfu the second arc appears after the annealing step.

One idea to get rid of unwanted phases or water exchanged regions, was to heat the sample for one hour at $700 \text{ }^\circ\text{C}$ and thus to remove residuals of H_2O and Li_2CO_3 . Figure 5.13 displays the Nyquist plot of an a) Al 0.30 and b) Al 0.40 pfu sample at RT. For Al 0.30 pfu the impedance spectrum shows a high frequency semicircle followed by a narrow shoulder. After annealing, the shoulder became very pronounced and had to be fitted using an additional $R||CPE$ element. The behavior of Al 0.40 pfu is inverted, as it showed two semicircles in its pristine state (Figure 5.13 b). Annealing, however, led

to the disappearance of the mid frequency contribution.

A calculation of the grain boundary thickness, using equation 5.4 yielded $0.5\ \mu\text{m}$. As for the Mo stabilized sample, this would be unusually large for a typical grain boundary.

Based on these inconsistent impedance measurements, I would only recommend annealing for samples with a pronounced second semicircle like in Figure 5.13 b) for the pristine sample. In any other situation I would dissuade from annealing because up until now it has not been fully understood how the sample is changed. A more detailed analysis on the effects of annealing is shown in chapter 5.7.

Table 5.5: Calculated value of the ideal capacitances and the thickness, based on the impedance spectra shown in Figure 5.13.

Li _{6.10} Al _{0.30}		pristine		annealed	
R _{bulk}	[Ω]	3980		7986	
R ₂	[Ω]	-		22233	
CPE ₁ n ₁	[F s ⁿ⁻¹] -	1.42 × 10 ⁻¹⁰	0.82	1.39 × 10 ⁻¹¹	0.94
C _{bulk}	[F]	6.18 × 10 ⁻¹²	-	5.13 × 10 ⁻¹²	-
d ₁	[cm]	0.40		0.40	
CPE ₂ n ₂	[F s ⁿ⁻¹] -	-	-	4.10 × 10 ⁻⁸	0.64
C ₂	[F]	-	-	7.57 × 10 ⁻¹⁰	-
d ₂	[μm]	-	-	20.1	

Li _{5.80} Al _{0.40}		pristine		annealed	
R _{bulk}	[Ω]	7977		3381	
R ₂	[Ω]	9170		-	
CPE ₁ n ₁	[F s ⁿ⁻¹] -	2.28 × 10 ⁻¹¹	0.91	5.97 × 10 ⁻¹⁰	0.73
C _{bulk}	[F]	4.58 × 10 ⁻¹²	-	5.24 × 10 ⁻¹²	-
d ₁	[cm]	0.40		0.40	
CPE ₂ n ₂	[F s ⁿ⁻¹] -	2.81 × 10 ⁻⁸	0.70	-	-
C ₂	[F]	8.09 × 10 ⁻¹⁰	-	-	-
d ₂	[μm]	10.8			

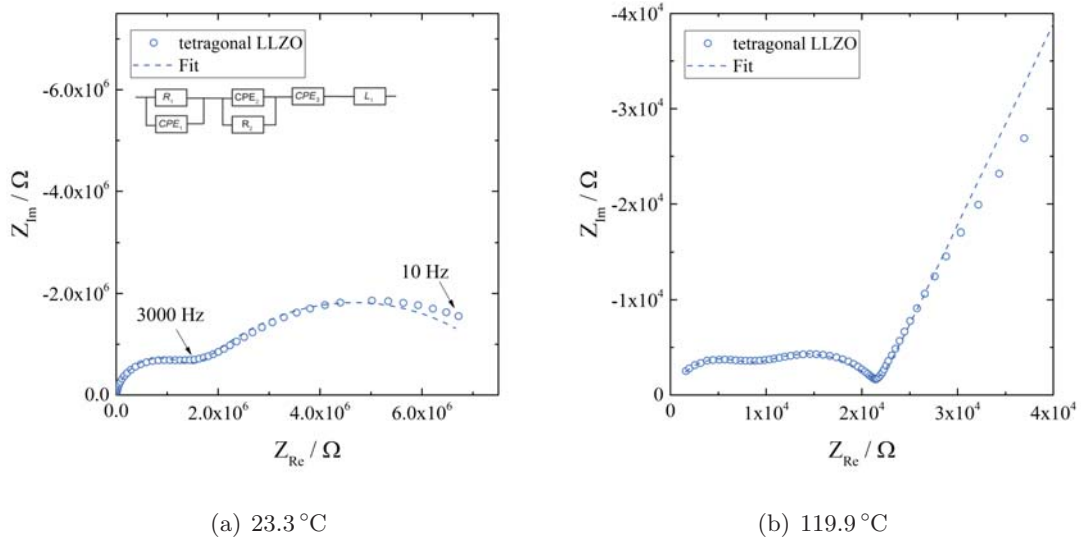


Figure 5.14: Impedance spectrum of a tetragonal LLZO sample, measured at a) 23.3 °C and b) 119.2 °C. The spectrum is fitted using the equivalent shown in plot a). The CPE₃ element becomes necessary at higher temperatures.

5.3 Electrochemical investigation of a tetragonal LLZO sample

A tetragonal LLZO ($\text{Li}_7\text{La}_3\text{Zr}_2\text{O}_{12}$) sample was prepared in the group of Prof. Sakamoto (University of Michigan, USA) by hot isostatic pressing (HIP). The sample was sintered at 1100 °C for one hour with 6 kN leading to a density of 90.3 %. Subsequently, it was attempted to investigate the phase transition from tetragonal to cubic phase. So far, there have been some publications investigating when and how effects of the phase transition occur [38, 51, 61, 123]. Larraz *et al.* investigated a tetragonal sample stored in ambient air, for which she could show, by the usage of XRD, a coexistence of cubic and tetragonal phases at 150 °C [59]. Upon further heating the cubic phase disappeared temporarily before it was reestablished at 700 °C. When cooling down to room temperature the phase of the sample became tetragonal again. Reasons behind the formation of this low temperature cubic phase are probably related to moisture from ambient air. Larraz has performed the same experiment with a sample protected from ambient air, for which she could not observe a low temperature phase transition.

Table 5.6: Fit parameters, obtained from the equivalent circuit shown in Figure 5.14 a) to simulate the impedance spectra.

R_1 [Ω]	σ_g [$S\text{ cm}^{-1}$]	CPE_1 [$F\text{ s}^{n-1}$]	n_1	C_1 [F]	ϵ_r
1.40×10^6	5.38×10^{-7}	1.19×10^{-11}	0.95	4.90×10^{-12}	74
R_2 [Ω]	σ_{gb} [$S\text{ cm}^{-1}$]	CPE_2 [$F\text{ s}^{n-1}$]	n_2	C_2 [F]	
6.07×10^6	1.91×10^{-7}	2.42×10^{-9}	0.70	3.82×10^{-10}	

Table 5.7: Data on conductivity and activation energy obtained from literature for tetragonal LLZO. * Current work, ** total conductivity

Temp. [$^{\circ}C$]	σ_g [$S\text{ cm}^{-1}$]	σ_{gb} [$S\text{ cm}^{-1}$]	E_{total} [eV]	Density	Reference
27	1.63×10^{-6}	5.59×10^{-7}	0.55	60%	[42]
25	2.00×10^{-6} **		0.44	-	[50]
25	4.40×10^{-7}	2.80×10^{-7}	0.35	-	[124]
25	$\approx 10^{-6}$	$\approx 10^{-7}$	0.56	-	[125]
20	2.09×10^{-6}	3.32×10^{-6}	0.53	73%	[126]
RT	2.30×10^{-5} **		0.43	98%	[127]
RT	$\approx 1 \times 10^{-7}$ **		0.54	93%	[61]
23	5.38×10^{-7}	1.91×10^{-7}	-	90%	*

Ongoing to the lack of access to proper equipment for protecting the sample from ambient air, the phase transition was investigated with the premise that water may affect the sample. Impedance spectra were measured in the temperature range where the phase transition was expected.

Impedance measurements were performed by using Ti/Pt as ionically "blocking" electrodes. The sample was investigated between 23.3 °C and 171.2 °C. The highest temperature was determined by the limit of the thermostat. Figure 5.14 shows an impedance spectrum measured at 23.3 °C. Two distinctly separated semicircles can be fitted, based on the denoted equivalent circuit. The evaluation of the high frequency semicircle results in a capacitance value that gives an ϵ_r value of 74. This indicates that this part of the impedance spectra can be attributed to ionic transport within the bulk. The capacitance CPE_2 of the second semicircle, which is three orders of magnitude larger than CPE_1 is attributed to grain boundaries within the polycrystal. At temperatures above 90 °C, the equivalent circuit requires an additional CPE_3 element, due to the appearance of the capacitive response coming from the electrodes as shown in Figure 5.14 b). Using equation 5.1, a bulk conductivity of $5.38 \times 10^{-7} \text{ S cm}^{-1}$ and a σ_{gb} value of $1.91 \times 10^{-7} \text{ S cm}^{-1}$ were obtained: The effective σ_{gb} was calculated from the total sample thickness rather than from the unknown grain boundary thickness. Published data on tetragonal LLZO present a variety of bulk and total conductivities ranging $2.30 \times 10^{-5} \text{ S cm}^{-1}$ to $4.40 \times 10^{-7} \text{ S cm}^{-1}$. With $5.38 \times 10^{-7} \text{ S cm}^{-1}$ the investigated sample yielded one of the lowest bulk conductivities published so far. Two other publications prepared a tetragonal LLZO by HIP, reaching relative densities of 93 % and 98% [61, 127]. Interestingly the difference in total conductivity between those samples was two orders of magnitude, suggesting density is not the main parameter for higher total ionic conductivity.

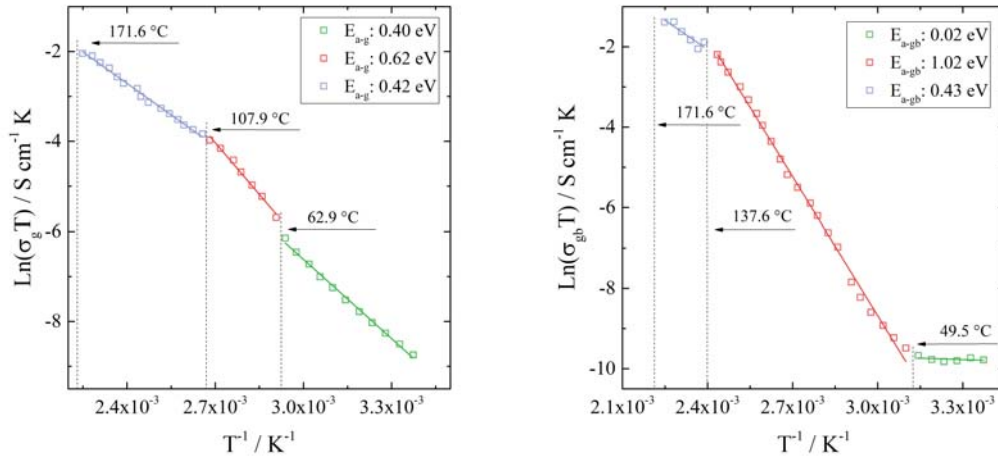
Phase transformation

In order to investigate the phase transition, a temperature cycle with steps of 5 °C was measured. To assure thermal equilibrium, the sample was kept at the respective temperature for 30 minutes. After this equilibration time, a set of three impedance

Table 5.8: Activation energies for grain and grain boundary and their changes upon heat treatment, subdivided in three sections.

		E_{a-g} [eV]			E_{a-gb} [eV]		
		I	II	III	I	II	III
1st cycle	heating	0.40	0.62	0.42	0.02	1.02	0.43
2nd cycle	heating	0.55	0.50	0.46	0.64	0.63	0.63
	cooling	0.48	0.92	0.44	0.58	0.99	0.68

spectra was measured. The results are plotted in an Arrhenius graph in Figure 5.15, distinguishing between a) grain and b) grain boundary contributions. Temperature dependent measurements revealed three different activation energies for both processes. The obtained activation energies for grain (E_{a-g}) and grain boundary (E_{a-gb}) are listed in Table 5.8. They are indicated as "1st cycle" and the different sections are numbered by the letters I, II and III. Upon heating, E_{a-g} changed from 0.40 eV to 0.62 eV and



(a) Arrhenius graph - grain

(b) Arrhenius graph - grain boundary

Figure 5.15: Arrhenius graphs showing the different conductivities of a) grain and b) grain boundary. Three different activation energies were found, the temperature at which they change, however, is different for grain and grain boundary.

back to 0.44 eV. The activation energy of section I and III are rather similar and a significant increase could only be measured in section II. Therefore we assume the phase transformation happened in section II between 63 – 108 °C. Other studies did observe the phase transition only at higher temperatures [38, 51, 61, 123].

Wang *et al.* as well investigated tetragonal LLZO and a phase transition using impedance spectroscopy. Because they could not separate grain and grain boundary, they obtained activation energies based on the total conductivity (0.69 eV, 1.29 eV, 0.58 eV). Like Larraz, they observed the phase transition between 150 and 210 °C. However, Larraz has shown that the phase transition is connected to moisture from ambient air, so maybe after a long storage time the effect of the exchange reaction accumulates, destabilizing the tetragonal garnet structure and allowing to rearrange a cubic structure at even lower temperatures.

In this first cycle, impedance measurements were only done during heating, but not during cooling. In a subsequent cycle, impedance measurements were performed during the heating and cooling process. The second experiment is referred to as "2nd" cycle in Table 5.8. When comparing the obtained activation energies of the "1st" and "2nd" cycle, one can observe an overall change.

In the "2nd" cycle, a separation into three sections was more difficult since transitions were less pronounced. This can be seen in the obtained activation energies for grain and grain boundary as differences between them have become much smaller upon heating. Upon cooling, the section II exhibited higher activation energies for grain (0.92 eV) and grain boundary (0.99 eV). It looks as if the heat treatment had triggered some sort of transformation process for both of them and so the "1st" cycle can be considered as a transition state. Maybe duration and temperature of the impedance measurements have induced microstructural changes, leading to a different modification of lithium ion diffusion paths.

Another interesting effect is the variation in ionic conductivity depending on the pre-treatment of the sample. For example, upon cooling down, the ionic conductivity of grain and grain boundary was partly slightly higher than upon heating. This is shown for the temperature range marked by a dotted rectangular in Figure 5.16. The effect

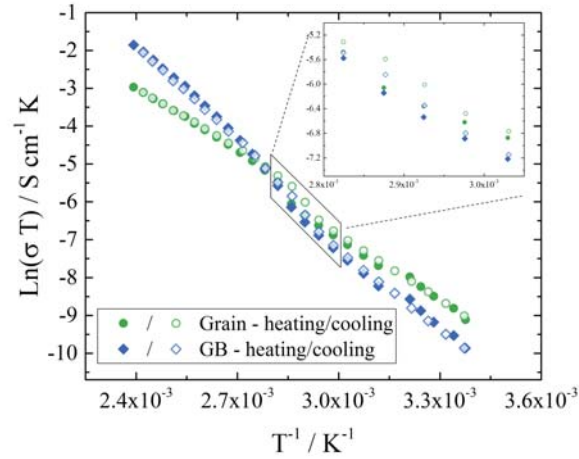


Figure 5.16: The Arrhenius graph shows the behavior of grain and grain boundary (GB) conductivities upon heating (full symbols) and cooling (open symbols). In the highlighted area the conductivities are different indicating a small hysteresis effect.

occurs at approximately 80 °C, that is also the temperature at which the phase transition was observed in the "1st" cycle.

The impedance measurements still reveal a possible phase transition between 63 °C and 108 °C for the grains. If we assume the garnet phase transformed from a tetragonal to a cubic phase, the question remains what happens above 108 °C when the activation energy changes again. Could the cubic phase be established or did it disappear again? Based on these considerations the hysteresis effect, observed upon cooling could be explained by a slow phase change. However, XRD measurements are required to further analyze these impedance spectroscopic observations.

5.4 Properties of a Ta-stabilized LLZO single crystal

Sample preparation

At the Leibniz Institute for Crystal Growth, a single crystal with a nominal composition of $\text{Li}_6\text{La}_3\text{Zr}_1\text{Ta}_1\text{O}_{12}$ was grown by the Czochralski technique [128]. Li_2CO_3 (+10 %

Table 5.9: Conductivity and capacitance of a pristine LLZO single crystal and a polycrystalline LLZO sample.

	σ_{bulk} [S cm^{-1}]	CPE_1 [F s^{n-1}]	n_1	C_1 [F]	ϵ_r
single crystal	1.69×10^{-4}	1.26×10^{-10}	0.90	2.14×10^{-11}	48
polycrystal	2.14×10^{-4}	9.82×10^{-10}	0.71	5.39×10^{-12}	70

excess), La_2O_3 , ZrO_2 , Ta_2O_5 as starting materials were uniaxial pressed (2800 kbar) and sintered at 1100 °C for 16 hours in air. As usual, the pellet was covered with mother powder to contain the loss of lithium as far as possible. The sintered LLZO pellet was melted by radio frequency induction heating, using a 25 kW microwave generator. To initialize the growing process, an iridium seed in a dinitrogen atmosphere was used. The stoichiometry of the single crystal was confirmed by ICP-OES. Further information about structural characterization and Li diffusion can be found in the work of Stanjesc *et al.* [129].

Impedance measurements

A single crystal, as well as a polycrystal of the same composition, were investigated by macroelectrode measurements. Figure 5.17 a) shows an impedance measurement of a pristine single crystal (green) and a polycrystal (blue). Both samples were investigated by using Ti/Pt electrodes. Only one high frequency semicircle is visible, followed by a capacitive increase caused by the ionically blocking electrodes. In both cases the first semicircle is attributed to ionic bulk conductivity. For the single crystal this high frequency feature is very well separated from the electrode. Both spectra could be simulated based on the equivalent circuit shown in Figure 5.17 a). Bulk conductivity of the single crystal was $1.69 \times 10^{-4} \text{ S cm}^{-1}$ and for the polycrystal it was $2.14 \times 10^{-4} \text{ S cm}^{-1}$. Further data like capacitances and relative permittivities are listed in Table 5.9.

Temperature dependent changes of σ_{bulk} are displayed in an Arrhenius graph in Figure 5.17 b). The single crystal lead to an activation energy of 0.51 eV and the polycrystal to 0.45 eV. Temperature dependent measurements did not reveal an additional semicircle for the polycrystalline sample. Hence, we can conclude that there are no blocking grain

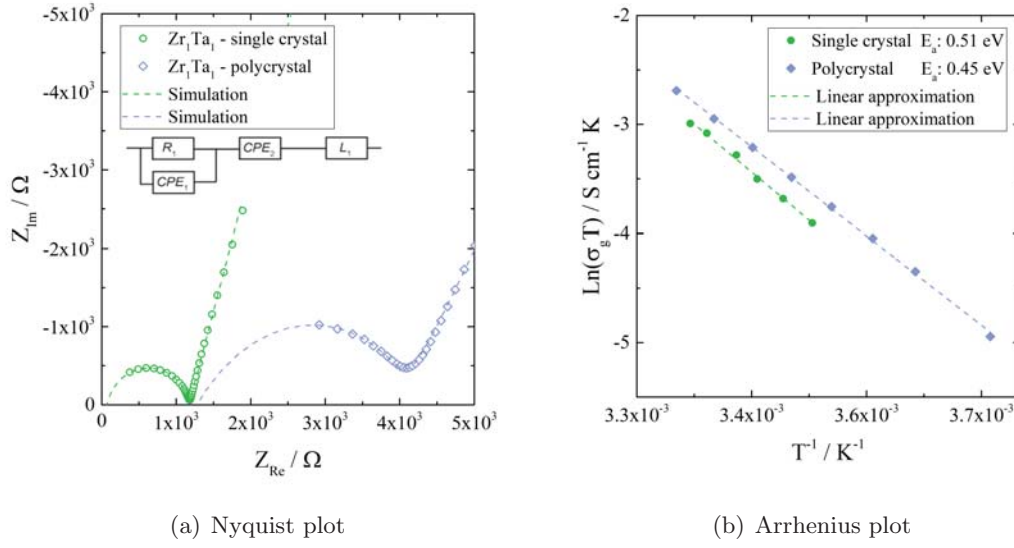


Figure 5.17: a) Nyquist plot of a single crystal and a polycrystal sample with nominal identical composition ($\text{Li}_6\text{La}_3\text{Zr}_1\text{Ta}_1\text{O}_{12}$). Impedance spectra were simulated using the equivalent circuit shown inside. b) The Arrhenius graph for both samples with the linear approximation.

boundaries within the sample. Similar results for conductivity and activation energy were obtained by Buschmann *et al.* for a polycrystal of the same composition [89]. In a subsequent experiment, the single crystals were tested in terms of stability against different solutions and different atmospheres by means of impedance spectroscopy.

Degradation in liquids

Four different single crystals were immersed in distilled water (H_2O - dest), 0.1 M HCl, LiCl and 1M LiOH for 30 days. The solutions were heated to 50°C to enhance reaction kinetics. Samples were investigated by impedance spectroscopy in their pristine state, after 7 days and after 30 days. The conductivity of the samples was investigated by impedance measurements at 25°C (T_{set}) using Pt-paste as electrode material. Electrodes were removed after impedance measurements. Figure 5.18 a-d) shows the impedance spectra of each single crystal in its pristine state. Some samples yielded an additional semicircle in the mid-frequency range b, c). Since these contributions could only be

Table 5.10: Ionic conductivity of single crystals before and after degradation in different atmospheres (CO₂, wet N₂) and liquids (HCl, LiOH, ...). Degradation in atmospheres were additionally performed on samples without an electrode (El*). The ionic conductivities listed represent bulk conductivities [S cm⁻¹].

Degradation	Pristine	Fluid		Gas
		7d	30d	9d
H ₂ O - dest	1.71×10^{-4}	1.32×10^{-4}	1.50×10^{-4}	-
HCl	1.69×10^{-4}	1.16×10^{-4}	1.83×10^{-4}	-
LiCl	2.44×10^{-4}	1.89×10^{-4}	0.77×10^{-4}	-
LiOH	1.68×10^{-4}	1.43×10^{-4}	1.67×10^{-4}	-
wet N ₂				
with El*	2.44×10^{-4}	-	-	2.40×10^{-4}
without El*	2.11×10^{-4}	-	-	2.01×10^{-4}
CO ₂				
with El*	2.74×10^{-4}	-	-	2.30×10^{-4}
without El*	2.30×10^{-4}	-	-	2.89×10^{-4}

found in two measurements, it is very likely that they are caused by the Pt-paste. The bulk conductivity of these four samples ranged from 1.68×10^{-4} to 2.44×10^{-4} S cm⁻¹. (Although 2.44×10^{-4} S cm⁻¹ seems to be an outlier, the difference to the others is not very large.)

After seven days immersed in different liquids, impedance measurements were repeated to record the actual state of the samples regarding their overall performance. Measured bulk conductivities are listed in Table 5.10 and each of them became slightly smaller. After 30 days, the experiment ended and bulk conductivities were measured again. In comparison to the values obtained from the pristine state, the changes are not very large, except for the sample which was immersed in the LiCl solution. For this sample, a drop from the highest value 2.44×10^{-4} to 0.77×10^{-4} S cm⁻¹ was observed. Only the sample immersed in HCl achieved a slightly higher ionic conductivity by the treatment. Measurements after seven days apparently represented an intermediate state of samples, but are not necessarily representative for further changes.

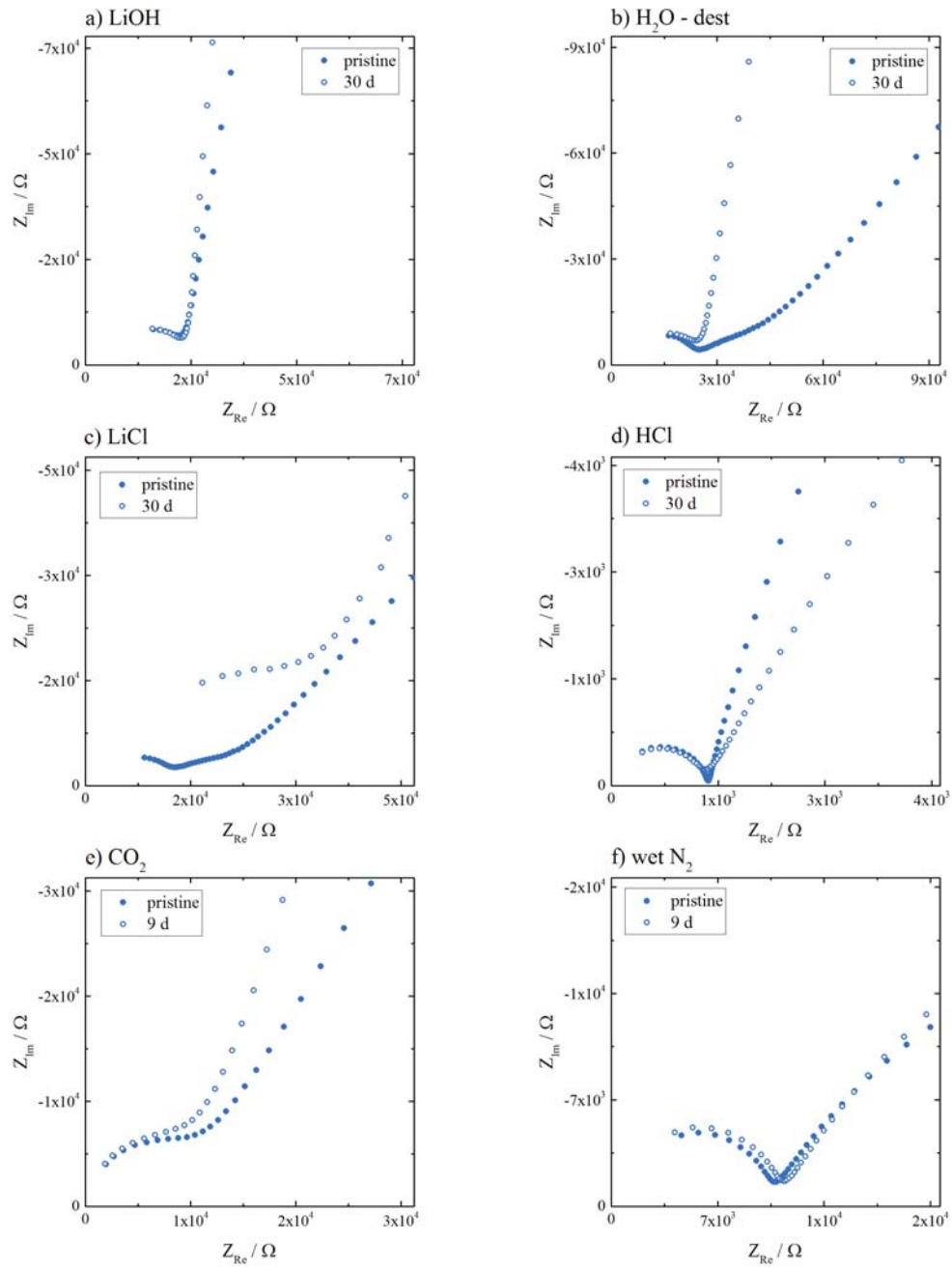


Figure 5.18: Impedance spectra of single crystals measured at 23.7 °C in their pristine state and in their final state after 30 days immersed at 50 °C in a) LiOH, b) distilled H₂O, c) LiCl, d) HCl, and after 9 days in e) CO₂ and f) humidified N₂ at room temperature.

The exchange reaction of Li^+/H^+ is an issue for each sample immersed in aqueous solutions. The extent of this reaction should be represented by the conductivity changes upon immersion in distilled water. A comparison of bulk conductivities between the beginning, 7 days and 30 days shows a decrease after 7 days, but after 30 days, it was nearly as high as in its pristine state. Under the premise the single crystal is not chemically inert against the incorporation of protons, a lower ionic conductivity could be explained by the formation of a protonated shell. Over time, protons will equally distribute in the grain and establish a H^+ and Li^+ conduction mechanism. Since the ionic conductivity does not have to decrease upon garnet protonation it is difficult to estimate the extent of Li^+ exchange based on impedance measurements. At least ion exchange would explain why each immersed sample obtained lower bulk conductivities after 7 days, than in its pristine state.

Similar to the effect of pure water, HCl solution should also protonate the garnet structure as follows:



Protons are incorporated and released Li leads to a solution of LiCl. We expect, given enough time, LiCl also forms a passivating layer on the sample's surface. Just like for pure H_2O , the extent of the incorporation can not be determined by impedance spectroscopy. The fact that the bulk conductivity increased should not be overinterpreted, since changes are in the range of 3%.

Some publications claimed the protonation of a garnet can be reversed, by immersing a sample in LiOH solution [65, 130–132]. Based on the impedance measurements, it can at least be said that the sample is stable in LiOH and does not undergo severe changes in bulk conductivity.

The most significant changes in bulk conductivity were observed upon immersion in LiCl. Beside effects due to protonation, LiCl should not react with the garnet. Adsorbents on the surface are not an issue since the sample is polished before electrodes were applied for impedance measurements. To explain this behavior, further analytical methods are

necessary.

Degradation in different atmospheres

Single crystals were investigated in two different atmospheres for several days, namely in humidified N_2 and CO_2 . The electrode material of choice was Pt-paste, since its porosity still allows the surface to be in contact with the atmosphere. In addition to a sample which was continuously investigated by impedance spectroscopy, another sample was placed within the measurement chamber. This additional sample was without electrodes, to assure each side is equally affected. All degradation measurements were done at room temperature.

Nitrogen was used as a carrier gas, because nitrogen itself should not affect the samples performance in any given way. Instead moisture can affect Li-ion diffusion. After more than 8 days in wet atmosphere σ_{bulk} changed from $2.44 \times 10^{-4} \text{ S cm}^{-1}$ to $2.40 \times 10^{-4} \text{ S cm}^{-1}$, which is negligible. Impedance spectra are shown in Figure 5.18 e) and the only observed effect upon moisture exposure was the formation of an additional mid-frequency contribution, most likely caused by a reaction between Pt-paste, water and LLZO. The reference sample confirmed the trend: After the exposure, electrodes were added and showed that the bulk conductivity hardly changed (from 2.11 to $2.01 \times 10^{-4} \text{ S cm}^{-1}$ - see Table 5.10).

Figure 5.19 a) illustrates the development of σ_{bulk} over eight days. There are fluctuations reaching a minimum at $2.24 \times 10^{-4} \text{ S cm}^{-1}$ and a maximum at $2.79 \times 10^{-4} \text{ S cm}^{-1}$. However, those fluctuations were rather small and might partly come from slight temperature variations. They confirmed the single crystal's chemical stability against water, just like shown for solution based degradation measurements. Only the very first sharp drop might be a true conductivity decrease due to unknown reasons.

In addition to degradation in wet N_2 , the effect of CO_2 on the ionic performance of single crystals was investigated over time. Again, one sample was continuously investigated by means of impedance spectroscopy, the other one was placed beside it without electrodes. After 180 h in CO_2 , σ_{bulk} dropped from $2.74 \times 10^{-4} \text{ S cm}^{-1}$ to $2.30 \times 10^{-4} \text{ S cm}^{-1}$. Again rather small changes are found, possibly induced by small temperature variations. The

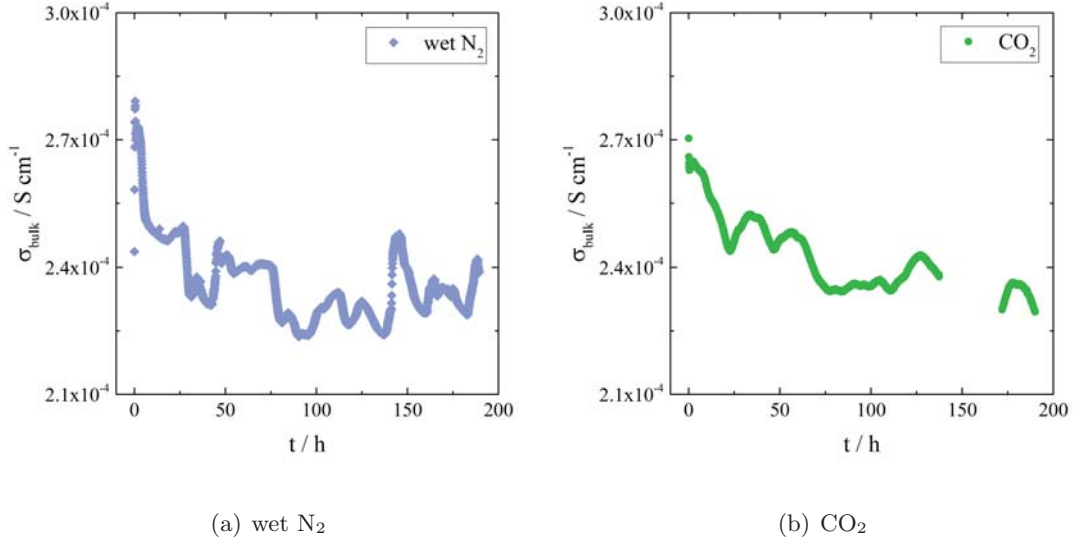


Figure 5.19: Development of σ_{bulk} during degradation in a) wet N_2 and b) CO_2 at room temperature.

reference sample showed a reverse trend where the ionic conductivity slightly improved from $2.30 \times 10^{-4} \text{ S cm}^{-1}$ to $2.89 \times 10^{-4} \text{ S cm}^{-1}$. With regard to the duration of the experiment, those were only slight changes. Impedance measurements showed no additional intermediate frequency features, only bulk and electrode were not well separated (Figure 5.18 e). Between 150 and 175 hours, data points are missing due to an error in the measurement software, however degradation went on.

Changes in ionic conductivity might be the result of the exchange reactions between the garnet and water/carbon dioxide, see below. Water can have a positive or a negative influence on ionic conductivity, as it is shown in chapter 5.8 for LLZO samples. In a CO_2 atmosphere, Li_2CO_3 can form on the surface of the sample. If the sample is free from water Li_2CO_3 may be formed according to:



Then Li can only be extracted from the garnet in form as Li_2O , due to the unavailability of electrons. So the extraction of Li goes along with oxygen, which would lead to the

formation of oxygen vacancies. This phenomena was recently investigated by Kubicek *et al.* [133], but the consequences of oxygen vacancies on ionic conductivities are unknown so far.

5.5 Microelectrodes for local conductivity and degradation measurements on Al stabilized $\text{Li}_7\text{La}_3\text{Zr}_2\text{O}_{12}$

5.5.1 Experimental

Large parts of this chapter are published in Journal of Electroceramics, 2016 [134].

Sample preparation

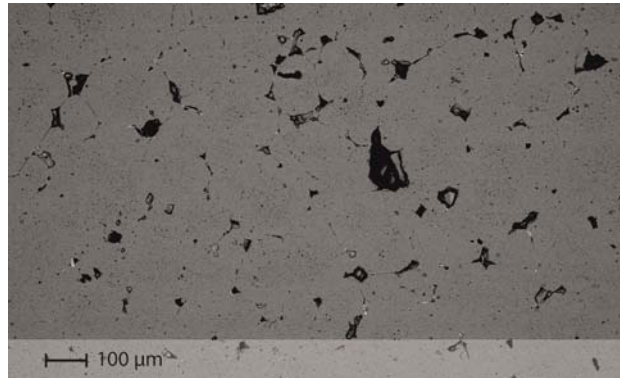


Figure 5.20: SEM image of an aluminium stabilized LLZO ($\text{Al} = 0.20$) garnet after sintering at $1230\text{ }^\circ\text{C}$ for 6 hours. Dark spots indicate the existence of some pores.

Samples with a nominal composition of $\text{Li}_{6.40}\text{Al}_{0.20}\text{La}_3\text{Zr}_2\text{O}_{12}$ were investigated. The synthesis route is based on the procedure described by Wagner *et al.* [115]. Li_2CO_3 (99%, Merck), Al_2O_3 (99.5%, Aldrich), La_2O_3 (99.99%, Roth), and ZrO_2 (99.0%, Roth) were weighed to reach the intended stoichiometry with an excess of 10 wt % Li_2CO_3 , with respect to the stoichiometric amount of Li_2CO_3 . The reagents were ground and mixed in an agate mortar under addition of isopropyl alcohol and then pressed into pellets. The pellets were heated to $850\text{ }^\circ\text{C}$ with a rate of $5\text{ }^\circ\text{C min}^{-1}$ and calcinated for 4 h. After cooling down, the pellets were again ground in an agate mortar and ball-milled for 1 h under isopropyl alcohol (FRITSCH Pulverisette 7, 800 rpm, 2 mm ZrO_2 balls). After drying, the powder was pressed into pellets and put into an alumina crucible. To avoid undesired incorporation of Al^{3+} from the crucible and to suppress evaporation of Li_2O from the material, the sample pellets were placed between two additional pellets of pure

$\text{Li}_7\text{La}_3\text{Zr}_2\text{O}_{12}$. The final sintering step was performed at 1230 °C for 6 h in ambient air. This results in a polycrystalline pellet with a diameter of about 7 mm, 4.6 mm thickness and typical LLZO-grain sizes of about 100 – 200 μm (Figure 5.20). The density of the sample, measured by a pycnometer (Brand GmbH), is 91 %.

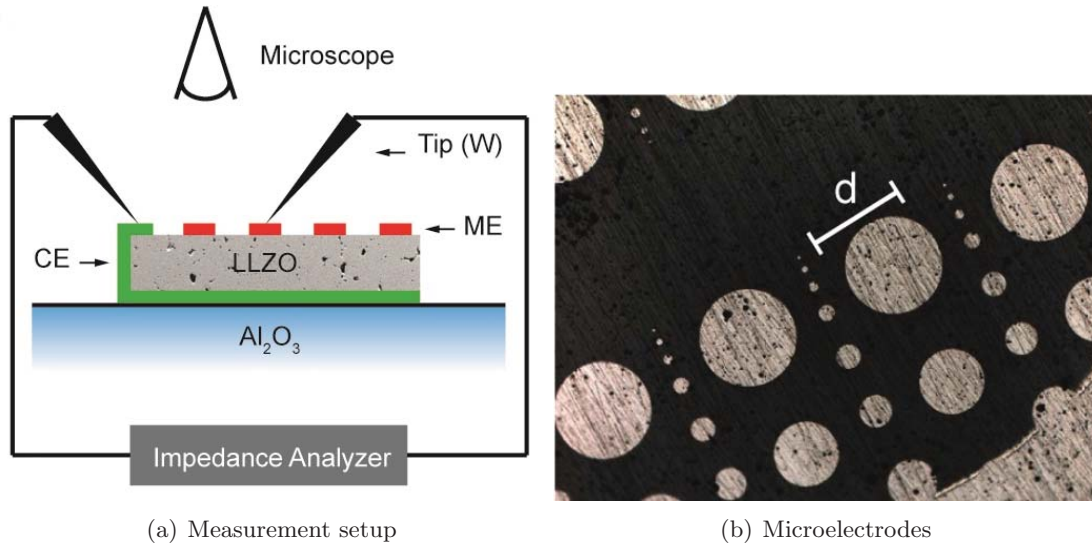


Figure 5.21: a) A scheme of the microelectrode measurement setup. b) The optical microscope image shows a part of the microelectrode array on top of a sample.

Electrical measurement

The ionic conductivity was measured by electrochemical impedance spectroscopy (EIS). For measurements of the effective conductivity of macroscopic samples (macroelectrode measurements), samples were polished by grinding paper (#4000), and thin films of Pt (200 nm) and Ti (10 nm) were deposited on top and bottom as ionically blocking electrodes. A thin film of titanium is required in order to improve the adhesion of platinum. For the EIS measurements, a Novocontrol Alpha Analyzer was used in the frequency range of $3 \times 10^6 - 10$ Hz. For such macroelectrode measurements the temperature was controlled by a Julabo F-25 HE thermostat, the exact temperature was 25.3 °C, determined by a thermocouple at the sample. Local conductivities were measured by

means of microelectrodes. Using photolithographic techniques in combination with ion beam etching, circular electrodes with diameters of 20 – 300 μm were prepared from the macroscopic Pt/Ti thin films on top of the samples. Microelectrode measurements were performed at ambient temperature ($T = 23.5^\circ\text{C}$). Tungsten needles were used to contact the microelectrodes under an optical microscope. The position of the needles was adjusted by mechanically controlled micromanipulators. Figure 5.21 a) illustrates the measurement setup and b) shows a part of the microelectrode array on top of the sample. Impedance measurements (Novocontrol Alpha Analyzer) were performed between a microelectrode and the counter electrode on the bottom side (Pt thin film with Pt paste at the sample edges for contact reasons).

5.5.2 Results and Discussion

Macroelectrode measurements

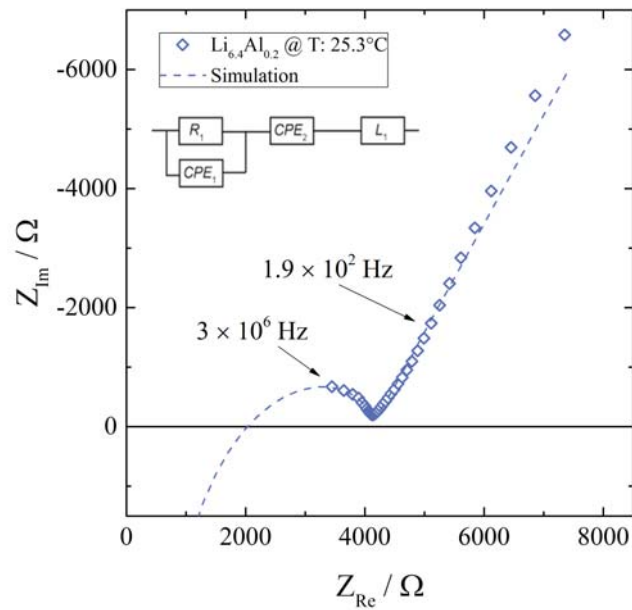


Figure 5.22: The impedance spectra of an aluminium stabilized LLZO sample at 25.3°C with measurement data (diamonds) and the simulation based on the fit to the equivalent circuit shown in the graph.

Before microelectrodes were prepared from the Pt thin film the samples overall performance was measured with the two macroscopic electrodes. The impedance spectrum of the Al stabilized LLZO garnet determined at 25.3 °C is plotted in Figure 5.22. It shows a part of a semicircle at high frequencies, followed by a well separated low frequency contribution which represents the impedance of the ionically blocking electrodes (Ti/Pt). In agreement with earlier studies we attribute the resistance of the high frequency feature to ion conduction in the bulk [40, 121].

In order to quantify the impedance spectrum properly, a resistor in parallel to a constant phase element ($R_1 || CPE_1$) is used for the bulk contribution, in series to a constant phase element CPE_2 describing the blocking electrodes. Additionally, an inductive element (L) is required due to wiring; this is responsible for the strong distortion of the bulk semicircle and the real axis intercept at finite Z_{Re} , rather than at $Z_{Re} = 0$. Hence, the intercept at 2000 Ω in Figure 5.22 is not an ohmic offset but the result of the serial inductance. The equivalent circuit shown in Figure 5.22 leads to a reliable fit (dashed line) of the impedance spectrum and relative permittivities ϵ_r calculated from CPE_1 are in the range of 70, which confirms the bulk character of this part of the spectrum. The fit parameters of the spectrum in Figure 5.22 are given in Table 5.11.

Table 5.11: Calculated value of the ideal bulk capacity [117] and the relative permittivity.

R_1 [Ω]	σ_{macro} [$S\ cm^{-1}$]	CPE_1 [$F\ s^{n-1}$]	n_1	C_1 [F]	ϵ_r
4082	3.26×10^{-4}	1.19×10^{-11}	0.95	4.90×10^{-12}	74

From the resistance R_1 , the effective bulk conductivity σ_{macro} can be calculated by

$$\sigma_{macro} = \frac{h}{A \times R_1} [S\ cm^{-1}] \quad (5.7)$$

with h being the sample thickness and A the surface area. In this specific case a bulk conductivity of $3.3 \times 10^{-4}\ S\ cm^{-1}$ results. This is within the range typically found for such LLZO samples stabilized with aluminium [49, 77, 99, 102, 104, 106, 111]. However, literature data reveal a large scattering of bulk or total conductivities, and in a separate

paper we will show that a substantial variation also exists between numerous nominally identical samples prepared in our labs [114]. Compared to all data of our extensive study, the sample shown here has a rather good effective ionic bulk conductivity, even though also two times higher values were measured [134].

Microelectrode measurements

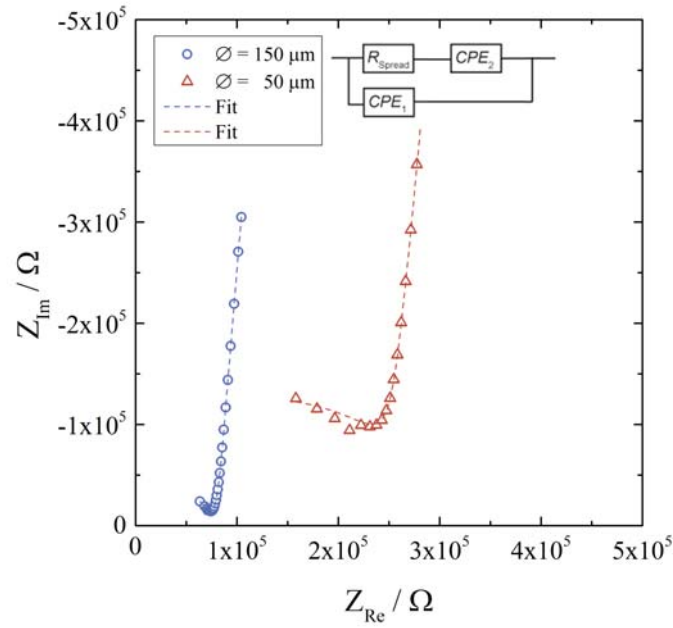


Figure 5.23: Impedance spectra of two Ti/Pt microelectrodes with different diameter d , and the corresponding fits (dashed line) based on the equivalent circuit shown above.

While macroscopic electrodes only yield mean sample conductivities, microelectrodes provide the possibility to measure spatially resolved conductivities. Based on the principle that most of the voltage between a microelectrode and an extended counter electrode drops very close to the microelectrode, the diameter of the electrode (d) determines the investigated volume beneath. The measured resistances are largely determined by the conductivity of a hemisphere with a radius of $2d$ [73]. An array of microelectrodes with different diameters (20 - 300 μm) was measured at room temperature. Figure 5.23

displays typical impedance spectra found in such microelectrodes measurements on the LLZO sample.

The high frequency arc corresponds to charge transport in the probed sample volume and is described by a resistive element (R_{Spread}) in the equivalent circuit. The low frequency capacitive increase is caused by the ionically blocking microelectrode and can be modelled by a constant phase element (CPE_2), in agreement with the macroscopic electrodes. In many cases, the electrode response of microelectrodes was even steeper than for macroelectrodes and thus the exponent of the CPE closer to 1. Since macro- and microelectrodes consist of the same material, this suggests the existence of some regions with very non-ideal ion blocking, distributed across the sample. The latter probably cause the less steep electrode response in the macroelectrode measurements. In parallel to R_{Spread} and CPE_2 , a stray capacitance (CPE_1) has to be introduced due to the measurement setup with a value in the range of 200 fF. This value is larger than what was expected for the bulk capacitance of most microelectrodes. Only for $d \geq 200 \mu\text{m}$ a geometrical bulk capacitance ($C = 2 \epsilon_r \epsilon_0 d$, $\epsilon_0 =$ vacuum permittivity) in the 200 pF range results from $\epsilon_r \approx 60$. However, adding the bulk capacitance to the equivalent circuit leads to an over parameterization and was therefore avoided here.

A fit of the impedance spectra to the equivalent circuit shown in Figure 5.23 (dashed line) reveals R_{Spread} values. If this spreading resistance R_{Spread} is only due to the charge transport in the bulk, it can be used to calculate the local conductivity, see below. In principle, grain boundary resistances or other interfacial resistances with parallel capacitances being smaller than the stray capacitance cannot be separated from the high frequency arc and may thus also contribute to R_{Spread} [135]. Grain boundary related effects could not be observed in macroscopic impedance spectra and we do not expect an effect in the microelectrode measurements either. However, additional interfacial resistances cannot be excluded, cf Sec. 5.5.2.

Figure 5.24 shows the resulting spreading resistances R_{Spread} of microelectrodes with a diameter of 100 μm (blue) and 200 μm (red). Variations are very moderate with standard deviations in the range of 9.5 %. From the spreading resistance R_{Spread} and the micro-

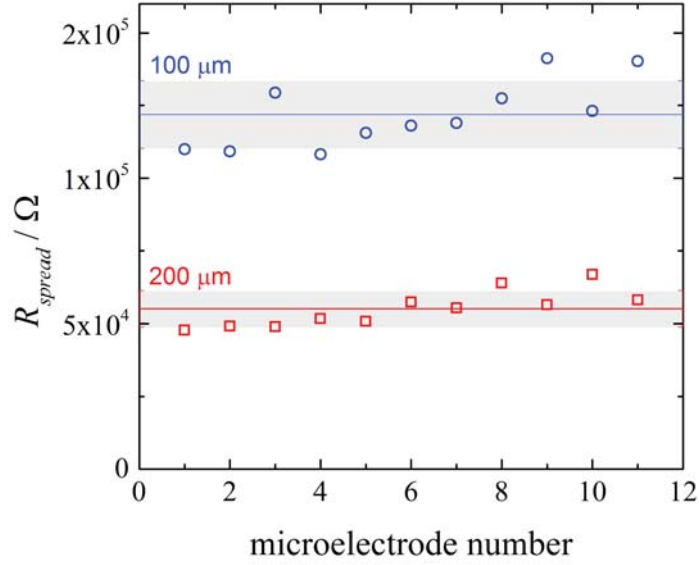


Figure 5.24: Statistical distribution of the spreading resistance for 100 and 200 μm sized electrodes.

electrode diameter d , a nominal bulk conductivity σ_{me} can be calculated [136] according to

$$\sigma_{\text{me}} = \frac{1}{2 d R_{\text{Spread}}} [\text{S cm}^{-1}]. \quad (5.8)$$

Provided the sample is homogeneous in the region beneath a microelectrode, this value reflects the true local Li-ion conductivity. Figure 5.25 displays nominal σ_{me} values for microelectrodes with different diameters. The solid line σ_{macro} represents the effective conductivity of the sample, measured with macroelectrodes before microelectrodes were prepared from the macroelectrode on top.

Within a factor of about two, macroscopic and microscopic conductivities agree. This indicates that local conductivity measurements using microelectrodes are meaningful and that microelectrode measurements are indeed possible on LLZO. However, the ionic conductivity from microelectrodes seems to depend on their diameter. The averaged local

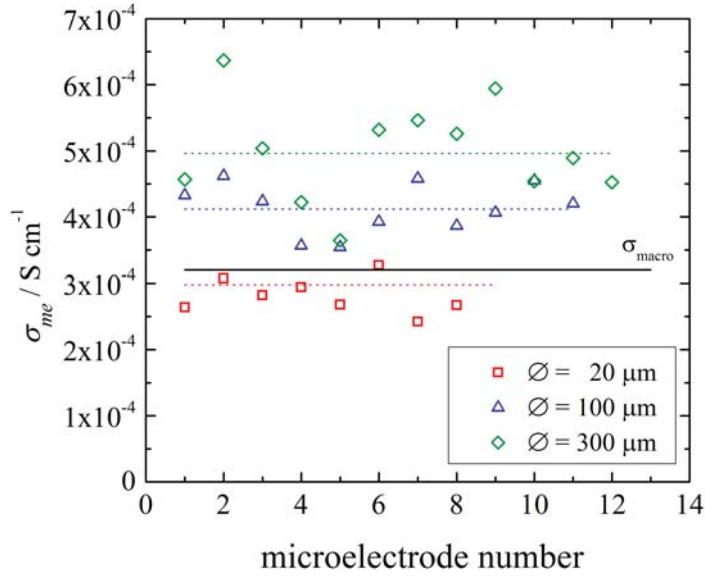


Figure 5.25: Local conductivities found for differently sized microelectrodes compared to the overall effective performance of the sample (σ_{macro}). The dotted lines represent the mean values of the microelectrodes.

conductivities found for 100 and 300 μm are $4.1 \times 10^{-4} \text{ S cm}^{-1}$ and $4.9 \times 10^{-4} \text{ S cm}^{-1}$ (Figure 5.26), respectively and thus somewhat larger than the mean conductivity of the sample ($3.3 \times 10^{-4} \text{ S cm}^{-1}$). The highest value found for a 300 μm microelectrode ($6.3 \times 10^{-4} \text{ S cm}^{-1}$) is even significantly higher than the values typically reported for LLZO stabilized with $\text{Al}_{0.20}$ ($\sigma_{macro} : 2.4 - 3.4 \times 10^{-4} \text{ S cm}^{-1}$) [49, 99, 100]. Plotting the averaged conductivity for every microelectrode diameter shows a clear trend (Figure 5.26): For the smallest microelectrodes the measured conductivities are smallest and even slightly below σ_{macro} .

As small microelectrodes are most sensitive to near-surface effects, this suggests that near to the surface less conductive regions exist. Possibly, local stoichiometric deviations near to the surface or the formation of impurity phases or secondary phases (e.g. $\text{La}_2\text{Zr}_2\text{O}_7$, LaAlO_3 , La_2O_3 , $\text{La}(\text{OH})_3$, Li_2CO_3 , LiOH), are responsible for the lower nominal conductivities σ_{me} [64, 68, 110, 137], since preparation as well as measurements include exposure to air. Hou et. al. investigated Al stabilized LLZO, sintered at 1100 $^\circ\text{C}$, by

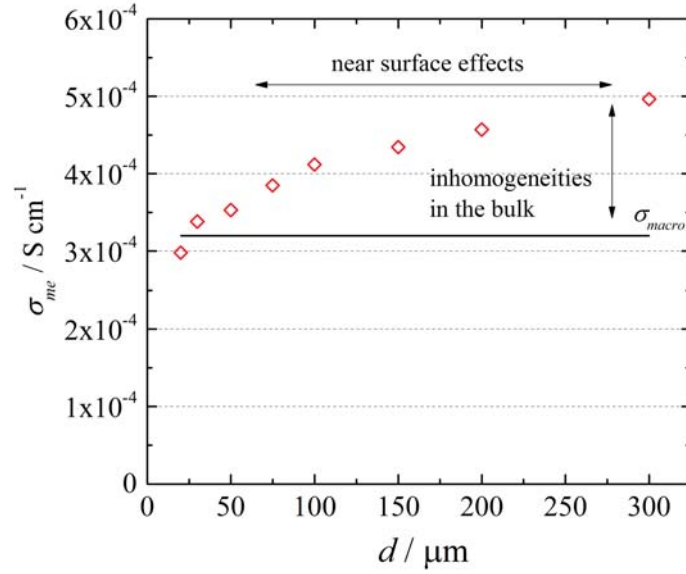


Figure 5.26: The averaged local conductivities of differently sized microelectrodes. The conductivity increases with the diameter of the electrode.

means of laser induced breakdown spectroscopy (LIBS) as a surface sensitive measurement method [119]. The maximum depth reached in that contribution was about $35 \mu\text{m}$, which is comparable to the range covered by microelectrodes with a diameter of $20 \mu\text{m}$. LIBS measurements detected aluminium and lithium rich phases in the first micrometres before the elemental distribution returns to a more or less equilibrated state. In addition, also misorientation angles may affect the ionic conductivity [110]. This could also contribute to the lower local conductivities found here.

The higher conductivity found for larger microelectrodes however, has to have a different reason. Most probably, the samples exhibit spatially inhomogeneous cation compositions and thus the effective conductivities from macroscopic measurements also include sample regions with smaller conductivity while the microelectrodes used in this study seem to be located on regions with higher conductivity. Indeed, in a related study on the scatter of effective sample conductivities of nominally identical samples we could identify significant conductivity variations not only from sample to sample but also within a given sample [114].

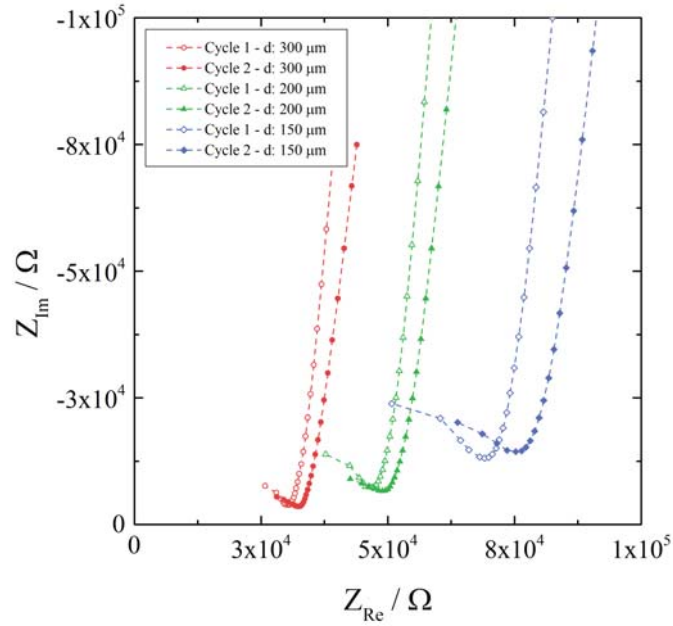


Figure 5.27: Impedance spectra of different microelectrodes measured in the pristine state (cycle 1) and after three weeks exposed to ambient air (cycle 2). A change in the impedance spectra indicates conductivity degradation.

Near-surface degradation

Owing to their near-surface sensitivity, microelectrodes can also be used to investigate degradation phenomena originating close to the surface. Here, the same microelectrodes were measured again after three weeks of storage in ambient air. The impedance spectra in Figure 5.27 display three different microelectrodes in their pristine state (cycle 1 - open symbols) and after long-time exposure to air (cycle 2 - filled symbols). Independent of the electrode diameter all impedance spectra indicate an increase in the resistance R_{Spread} compared to the pristine state.

These changes are probably related to near-surface degradation effects such as the formation of LiOH and Li_2CO_3 caused by a reaction with moisture and CO_2 from ambient air and the exchange of Li^+ by H^+ [60, 132, 137, 138]. Figure 5.28 summarizes the measurements and illustrates the resistive changes between the pristine and the degraded

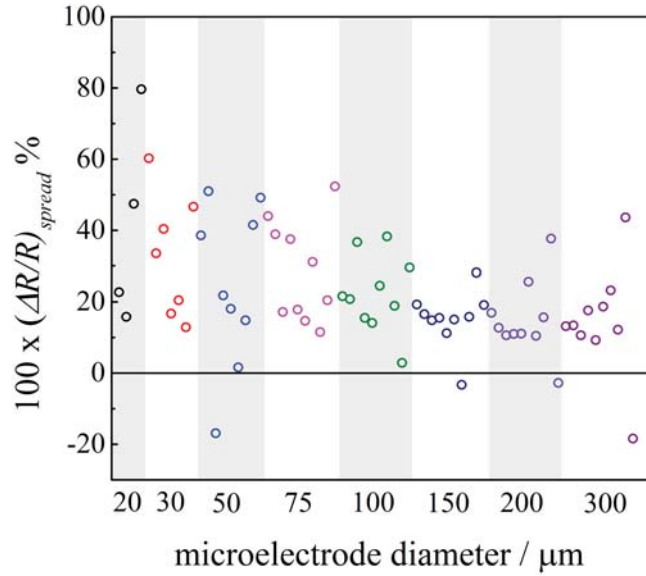


Figure 5.28: The relative change in resistance $R_{S_{\text{pread}}}$ for differently sized electrodes measured after 3 weeks exposure to ambient air.

state in dependence of the microelectrode diameter. Microelectrodes with a diameter of 20 - 50 μm show the largest changes with a maximum of 80 % resistance increase. With increasing diameter, the variations become smaller. This supports the assumption of near-surface degradation, which becomes less important as the probed volume beneath the electrode increases, i.e. as microelectrode diameters increase. Possibly a similar near-surface degradation already before the very first microelectrode measurements was also responsible for the low conductivities found for 20 μm microelectrodes on pristine samples (see Sec. 5.5.2 - Microelectrode measurements).

5.5.3 Conclusion

It was shown that microelectrodes (\varnothing : 20 – 300 μm) can be successfully applied to a polycrystalline LLZO garnet sample and allowed microelectrode impedance spectroscopy studies. Those resulted in local information on bulk ionic conductivities. A comparison between the effective conductivity of the overall sample and conductivities of local areas of the sample revealed differences. Locally, conductivities were up to twice the effective

bulk conductivity with a maximum local value of $6.3 \times 10^{-4} \text{ S cm}^{-1}$. Reasons behind these conductivity differences are most probably compositional variations in the sample. Moreover, smaller microelectrodes lead to smaller nominal conductivities which indicates that near to the surface less conductive regions exist. The sensitivity of microelectrodes towards near-surface resistive changes was also used to investigate how exposure to ambient air affects the properties of LLZO samples. A substantial degradation of the local conductivity was found, particularly for small microelectrodes.

5.6 Li-ion conductivity fluctuations within $\text{Li}_7\text{La}_3\text{Zr}_2\text{O}_{12}$ solid electrolytes and their relation to local stoichiometric changes

5.6.1 Experimental

Large parts of this chapter are submitted to Journal of The Royal Society , 2017 [120].

Sample preparation

Three nominally identical samples (A, B, C) with an intended composition of $\text{Li}_{6.40}\text{Al}_{0.20}\text{La}_3\text{Zr}_2\text{O}_{12}$ were investigated. The synthesis route is based on the procedure described by Wagner *et al.* [115]. Li_2CO_3 (99%, Merck), Al_2O_3 (99.5%, Aldrich), La_2O_3 (99.99%, Roth), and ZrO_2 (99.0%, Roth) were weighed to reach the intended stoichiometry with an excess of 10 wt % Li_2CO_3 , with respect to the stoichiometric amount of Li_2CO_3 . The reagents were grounded and mixed in an agate mortar under addition of isopropyl alcohol and then pressed into pellets. The pellets were heated to 850°C with a rate of 5°C min^{-1} and calcinated for 4 h. After cooling down, the pellets were again grounded in an agate mortar and ball-milled for 1 h under isopropyl alcohol (FRITSCH Pulverisette 7, 800 rpm, 2 mm ZrO_2 balls). After drying, the powder was pressed into pellets and put into an alumina crucible. To avoid undesired incorporation of Al^{3+} from the crucible and to suppress evaporation of Li_2O from the material, the sample pellets were placed between two additional pellets of pure $\text{Li}_7\text{La}_3\text{Zr}_2\text{O}_{12}$. The final sintering step was performed at 1230°C for 6 h in ambient air.

X-ray diffraction (XRD)

Phase analysis was performed by XRD experiments on a Panalytical X'Pert MPD with Cu K_{α} radiation [116]. The pattern was analyzed with HighScore, a program provided by Panalytical. The 2Θ scan range was between 5° and 120° with a step size of 0.026° .

Electrochemical impedance spectroscopy

The ionic conductivity was measured by electrochemical impedance spectroscopy (EIS). To measure the effective conductivity of macroscopic specimens (macroelectrode measurements), samples were polished by grinding paper (# 4000) to remove near surface reaction layers, and thin films of Pt (200 nm) and Ti (10 nm) were deposited on top and bottom as ionically blocking electrodes. A thin film of titanium is required in order to improve the adhesion of platinum. For the EIS measurements, a Novocontrol Alpha Analyzer was used in the frequency range of $3 \times 10^6 - 10$ Hz. In such macroelectrode measurements the temperature was controlled by a Julabo F-25 HE thermostat, the exact temperature was 25.4°C , determined by a thermocouple at the sample.

Local conductivities were measured by means of microelectrodes. Using photolithographic techniques in combination with ion beam etching, circular electrodes with diameters of $100\ \mu\text{m}$ were prepared from the macroscopic Pt/Ti thin films on top of the samples. Microelectrode measurements were performed at ambient temperature ($T = 23.5^{\circ}\text{C}$). Tungsten needles were used to contact the microelectrodes under an optical microscope. The position of the needles was adjusted by mechanically controlled micro-manipulators. Figure 5.29 a) illustrates the measurement setup and b) shows a part of the microelectrode array on top of the sample. Impedance measurements (Novocontrol Alpha Analyzer) were performed between a microelectrode and a counter electrode on the bottom side (Pt thin film with Pt paste at the sample edges for contact reasons).

LA-ICP-OES

All LA-ICP-OES experiments were performed using a NWR213 laser ablation system (ESI, USA) equipped with a frequency quintupled 213 nm Nd:YAG laser and a fast-washout ablation cell. The laser ablation device was coupled to an iCAP 6500 RAD

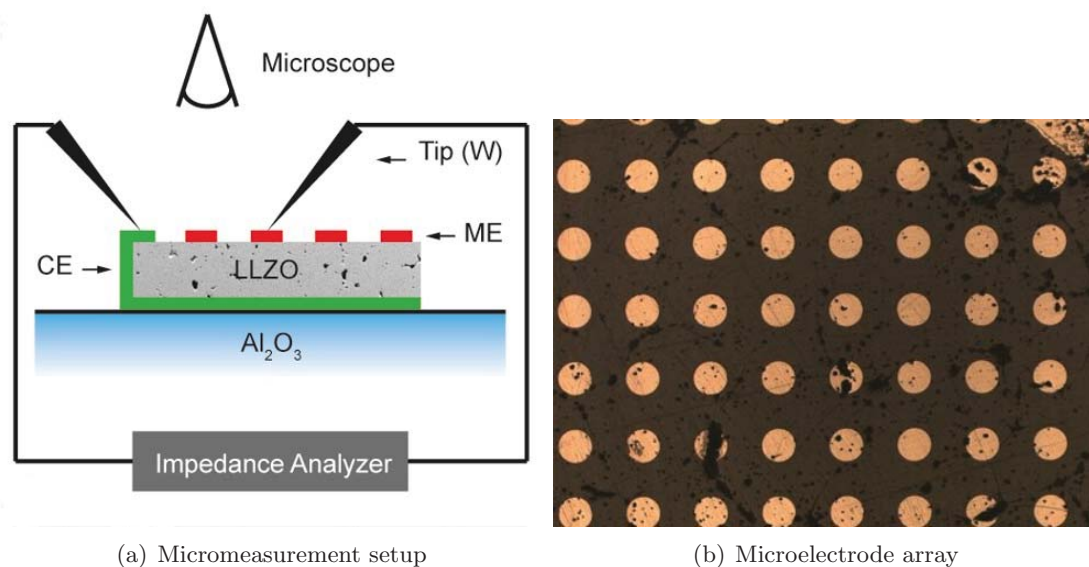


Figure 5.29: a) A scheme of the microelectrode measurement setup. b) The optical microscope image shows a part of the microelectrode array on top of a sample.

ICP-OES instrument (Thermo Fisher Scientific, USA) using PTFE tubing with an inner diameter of 0.4 mm. A plasma torch with a corrosion-resistant ceramic injector tube of 1.5 mm inner diameter was utilized for all experiments. Cell washout was performed using He as carrier gas, which was mixed with Ar make-up gas upon introduction into the plasma. For data acquisition iTEVA software (v.2.8.0.96) provided by the manufacturer of the instrument was used. The two most sensitive and non-interfered emission lines of Al, La, Li, and Zr were measured. For each element, only one emission line was used for signal quantification, the other one was used for quality control of the analysis.

Two-dimensional elemental distribution images of whole LLZO pellets were created using line scan ablation patterns with adjoining lines. For all documented experiments a laser beam diameter of $100\ \mu\text{m}$ and a scan speed of $100\ \mu\text{m}\ \text{s}^{-1}$ was used, which results in a lateral resolution of $100\ \mu\text{m}$. In order to remove surface contaminations as well as near-surface segregation phases (e.g., Li_2CO_3 due to air exposure) a pre-ablation step consisting of a similar line scan pattern with a laser beam diameter of $250\ \mu\text{m}$ was installed prior to the measurements. Using the obtained time-resolved signal intensities,

image processing was performed by the software ImageLab (v.2.41, Epina GmbH, Austria). Detailed information about the parameters used for the LA-ICP-OES experiments are given in the supplementary information.

For signal quantification, matrix-matched standards were prepared by isostatically pressing LLZO powders with different Al content into pellets. To obtain these powders, sintered LLZO pellets with various Al concentration were crushed, ground, and homogenized using an agate mortar. To determine their chemical composition, a part of each powder was digested using a borax fusion, dissolved in a HF/HCl/HNO₃ mixture, and analysed by conventional liquid ICP-OES.

Measurement of the pressed LLZO standards was performed directly before sample analysis, using the same instrumental parameters and laser settings. To ensure that the ablated material is representative for the whole pellet, multiple line scan patterns with adjoining lines were used for each standard. Per standard, four-line scan pattern with an area of about 0.4 mm² were applied on different positions of the pellet. Each pattern was ablated three times.

For the correction of variations in sample ablation and transport, as well as instrumental drifts, an internal standard-independent normalization technique presented by Liu *et al.* was adapted for LLZO samples [139]. Based on the consideration that the sum of all metal oxides in LLZO adds up to 100 wt%, this approach uses the intensities of all measured elements expressed as the corresponding oxides (Al₂O₃, Li₂O, La₂O₃, ZrO₂) for signal normalization.

The accuracy of the LA-ICP-OES analysis was estimated using the prepared LLZO standards for external validation. For the Al/La, Li/La, and Zr/La atomic ratio average relative deviations of 9.1%, 1.2%, and 0.8% were obtained, respectively. The comparably high deviation of the Al/La ratio is attributable to relatively low Al concentration.

Further information concerning the quantification of the described LA-ICP-OES measurements can be found in an upcoming publication [140].

Table 5.12: Thickness and surface of the investigated LLZO samples (A, B, C)

	Thickness [cm]	Area [cm ²]
A	0.41	0.34
B	0.46	0.35
C	0.10	0.45

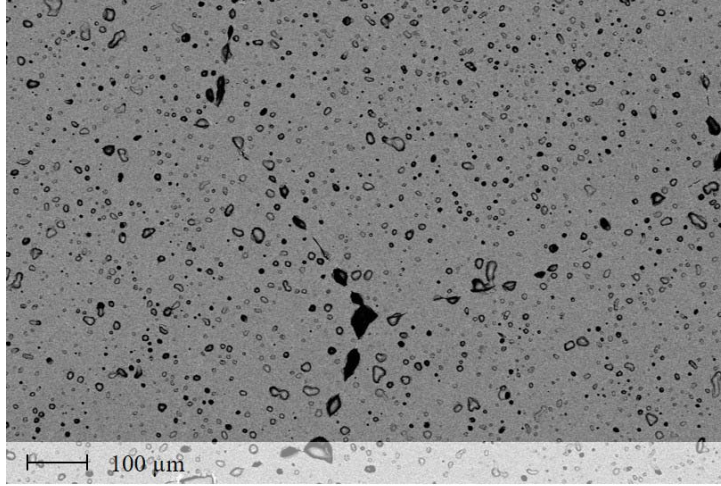


Figure 5.30: SEM image of an aluminium stabilized LLZO ($Al = 0.20$) garnet after sintering at $1230\text{ }^{\circ}\text{C}$ for 6 hours. Dark spots indicate the existence of some pores.

5.6.2 Results

Sample quality

The geometry of the resulted polycrystalline pellets are listed in Table 5.12. The typical LLZO-grain size is about $100 - 200\text{ }\mu\text{m}$ (Figure 5.30). The density of the samples, measured by a pycnometer (Brand GmbH), is about 91 %. The XRD analysis confirmed the cubic structure of the investigated samples (Figure 5.31). As a second phase, only lithium oxide was found on sample A.

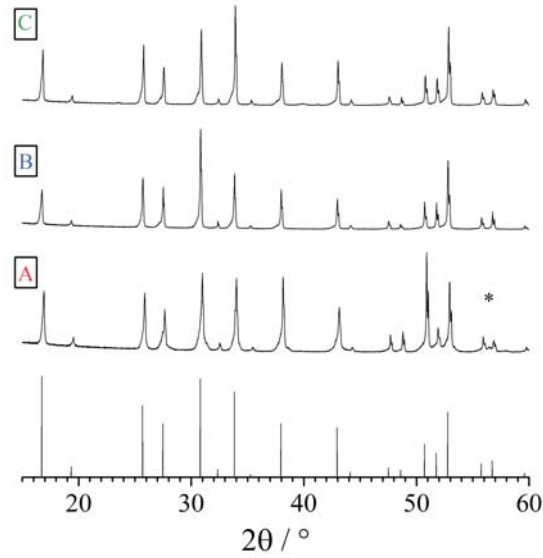


Figure 5.31: XRPD patterns of samples A, B and C as well as the cubic reference pattern. No secondary phases could be found, except for LiO_2 (*) in sample A.

Macroelectrode measurements

Before microelectrodes were prepared from the Pt thin film the effective conductivity of each sample was measured with two macroscopic electrodes. The normalized impedance spectra of the Al stabilized LLZO garnets determined at 25.3°C , are plotted in Figure 5.32. It shows a part of a semicircle at high frequencies, followed by a well separated low frequency contribution which represents the impedance of the ionically blocking electrodes (Ti/Pt). In agreement with earlier studies we attribute the resistance of the high frequency feature to ion conduction in the bulk [40, 121].

To quantify the impedance spectrum properly, a resistor in parallel to a constant phase element ($R_1 || \text{CPE}_1$) is used for the bulk contribution, in series to a constant phase element CPE_2 , describing the blocking electrodes. Additionally, an inductive element (L) is required due to wiring; this is responsible for the partly strong distortion of the bulk semicircle at higher frequencies; for samples with smaller resistivities this even causes a real axis intercept at finite Z_{Re} , rather than at $Z_{\text{Re}} = 0$. Hence, the intercept

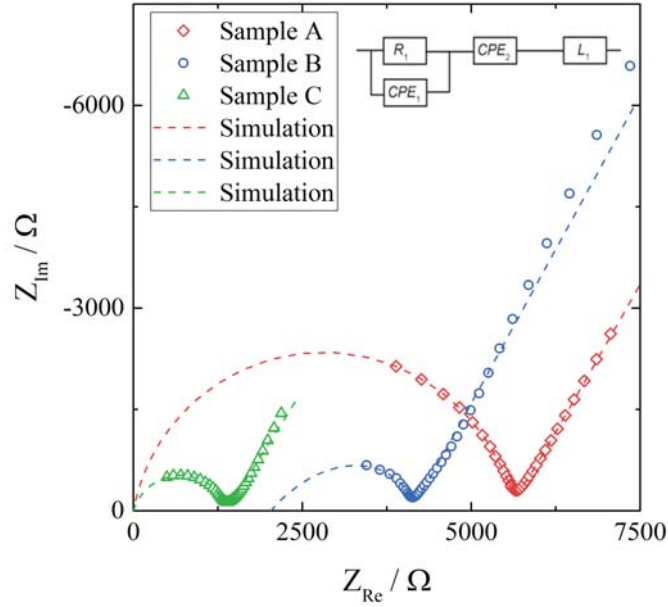


Figure 5.32: The impedance spectra of the aluminium stabilized LLZO samples at 25.3 °C with macroelectrode measurement data (diamonds) and the simulation based on the fit to the equivalent circuit shown in the graph.

at ca. 2000 Ω for sample A and B in Figure 5.32 is not an ohmic offset but the result of the serial inductance. The equivalent circuit shown in Figure 5.32 leads to a reliable fit (dashed line) of the impedance spectrum and relative permittivities (ϵ_r), calculated from CPE_1 are in the range of 45 – 75 [117]. This confirms the bulk character of this part of the spectrum. The fit parameters of the spectra in Figure 5.32 are given in Table 5.13.

From the resistance R_1 , the effective bulk conductivity σ_{macro} can be calculated by

$$\sigma_{\text{macro}} = \frac{h}{A \times R_1} [\text{S cm}^{-1}] \quad (5.9)$$

with h being the sample thickness and A the surface area. In this case the bulk conductivity lies between 1.65 and $3.26 \times 10^4 \text{ S cm}^{-1}$, which is within the range typically found

Table 5.13: Fit parameters, calculated bulk capacitance and relative permittivity values as well as conductivities of the macroscopic LLZO samples (A, B, C).

	R_1 [Ω]	σ_{macro} [mS cm^{-1}]	CPE_1 [10^{-11} F s^{n-1}]	n_1	C_1 [10^{-12} F]	ϵ_r
A	5600	0.213	3.31	0.88	4.14	56
B	4082	0.326	1.19	0.95	4.90	74
C	1370	0.165	39.6	0.82	18.1	46

for LLZO samples stabilized with aluminium [77, 99, 102, 104, 106, 111, 122].

Microelectrode measurement

With macroscopic electrodes only mean bulk conductivities can be obtained. Microelectrodes, on the other hand, provide a tool to measure spatially resolved conductivities. This becomes possible since most of the volt-age between the microelectrode and the counter electrode drops near to the microelectrode. When changing the diameter d of the microelectrode, the investigated volume beneath changes. The measured resistances are largely determined by the conductivity of a hemisphere with a radius of about $2d$ [35]. From the measured bulk-related resistance R_{spread} the local ionic conductivity can be calculated via

$$\sigma_{\text{me}} = \frac{1}{2 d R_{\text{spread}}} [\text{S cm}^{-1}] \quad (5.10)$$

provided the distance of the microelectrode to the counter electrode is much larger than the microelectrode diameter [99]. On each of the three investigated samples, an array of circular electrodes with a diameter of $100 \mu\text{m}$ was applied. Thus, our measurements are able to resolve local conductivity variations on the length scale of a few $100 \mu\text{m}$. However, these microelectrode measurements still average over a certain volume.

Figure 5.33 displays typical impedance spectra obtained when measuring with microelectrodes. The impedance spectra are analyzed by the simple equivalent circuit shown inside Figure 5.33. The resistive element R_{spread} describes the charge transport in the probed volume. The serial constant phase element (CPE_2) is attributed to the ionically

blocking electrode material just like for the macroelectrode measurement in Figure 5.32. Parallel to these two elements is a stray capacitance (CPE_1) with a value in the range of 200 fF. This is caused by the measurement setup, particularly by the capacitance between contacting needle and the counter electrode. Adding a very small LLZO bulk capacitance (about 100 fF) to the equivalent circuit leads to an overparameterization and was therefore avoided.

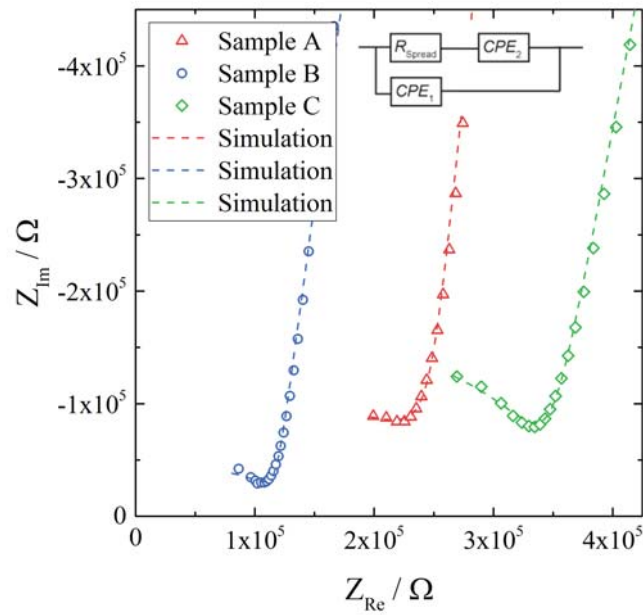


Figure 5.33: Impedance spectra obtained on Ti/Pt microelectrodes with a diameter d of $100\ \mu\text{m}$, on three different samples. Also included, the corresponding fits (dashed line) based on the equivalent circuit shown above.

Local conductivities

Figure 5.34 a) illustrates the location of the microelectrodes and the related conductivities beneath the investigated microelectrodes on sample A, using a colour map. Light colours (yellow, green) determine areas with a good ionic conductivity (above $2.0 \times 10^{-4}\ \text{S cm}^{-1}$) and cold colours (blue) represent low conductive areas (below $8.0 \times 10^{-5}\ \text{S cm}^{-1}$). In Figure 5.34 b), measurements of one row of microelectrodes from the

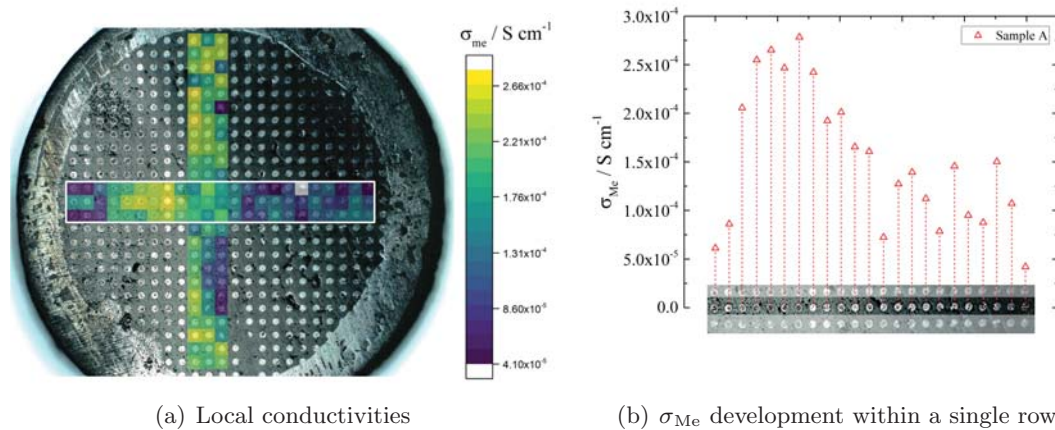


Figure 5.34: a) Local conductivities obtained from microelectrode measurements (sample A). Coloured areas mark the investigated areas of the sample and indicate the measured conductivity. b) The middle row of microelectrodes in the area, highlighted by a white rectangle, displays the change in conductivity from the left side of the sample to the right side.

left to the right side of the sample, show a gradient in conductivity. Values vary between 4.2×10^{-5} S cm⁻¹ on the right side to 2.8×10^{-4} S cm⁻¹ on the left hand side. Similar results were obtained for the rows above and beneath the highlighted row.

This demonstrates that parts of the sample exhibit higher conductivities than the effective σ_{macro} (2.1×10^{-4} S cm⁻¹) while others are less conductive. The existence of a gradient is in agreement with a previous study, where reducing the size of LLZO samples and repeatedly measuring σ_{micro} also revealed conductivity variations [114]. Measurements from top to the bottom of the sample (vertical coloured bar in Figure 5.34) did not reveal a clear trend as found for the horizontal measurements. The conductivity variations in this area are rather small and values are comparable to the value obtained from the macroelectrode measurement.

Similar local conductivity measurements were done on sample B (Figure 5.35). This sample was covered with differently sized microelectrodes (300 - 10 μm), but for the sake of comparability only electrodes with the diameter (100 μm), used on samples A and C, were investigated. The obtained conductivities are higher than for σ_{macro} (3.26×10^{-4} S cm⁻¹), but overall in good agreement with the macro measurement. Local conductivity mea-

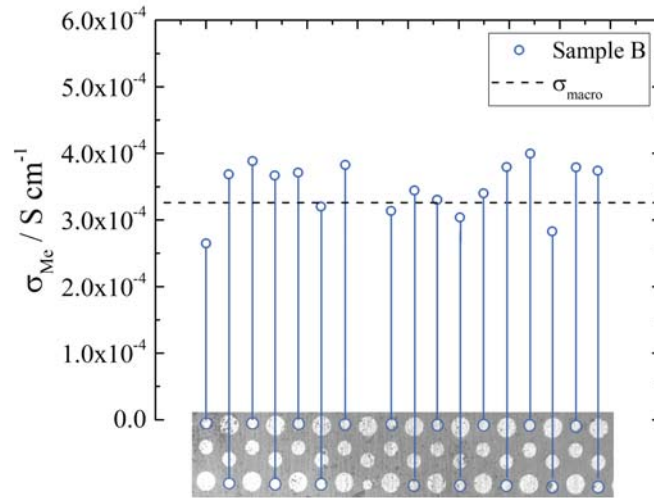


Figure 5.35: Local conductivity measurements obtained from sample B using $100\ \mu\text{m}$ electrodes. The local conductivity does not show very pronounced variations.

measurements did not yield strong inhomogeneities, as variations are minor. This rather good agreement of microelectrode and macroelectrode measurements is a strong argument in favor of microelectrode measurements, representing bulk related properties and therefore measured gradients (sample A) reflect real bulk inhomogeneities.

The macroelectrode measurement of sample C showed lower conductivity compared to sample A and B ($1.65 \times 10^{-4}\ \text{S cm}^{-1}$). Microelectrode measurements were performed on both sides of this sample. On *side one* (Figure 5.36 diamond) measured conductivities are largely similar or smaller than σ_{macro} but did not show any spatial trend. Compared to sample B much more scattering is present. Possible reasons are imperfect microelectrode geometries or adhesion or some degradation effects, for example induced by moisture or spots with higher porosity below some microelectrodes. The measurements on *side two* (Figure 5.36 circles) resulted in very similar conductivities, again some spots were less conductive, the majority, however, was close to the obtained macroelectrode value. Thus the lower overall conductivity is not caused by a very low conductive layer in series with sample parts of higher conductivity. Rather, the entire sample seems to

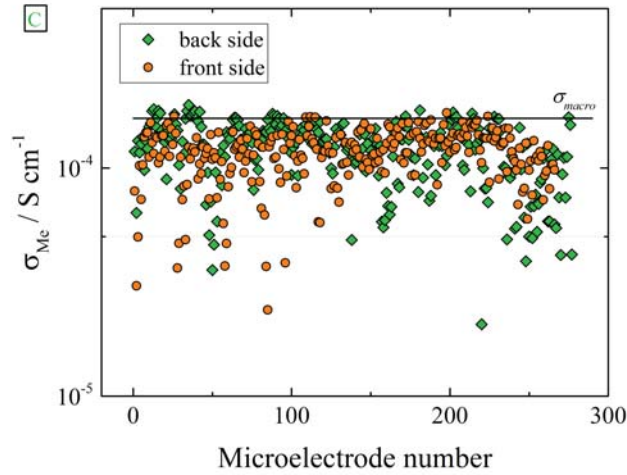


Figure 5.36: Microelectrode measurements on sample C from *side one* (diamonds) and *side two* (circles) of the sample.

be less conductive than A and B.

LA-ICP-OES

In order to find a reason behind the conductivity gradient in sample A, a local chemical analysis was performed using LA-ICP-OES. Figure 5.37 displays the results showing the content of a) Li, b) Zr and c) Al of sample A. Also sample B and C were analyzed, the measurements are shown in the supplementary information. The measurement data are not smoothed, each pixel represents the stoichiometry, calculated based on the measured atomic ratios (choosing 3 pfu La as the fixed-point).

The Zr signal shows very little variation and a homogeneous distribution across the sample, as well as a good agreement with the theoretical Zr content of 2.0 pfu. Li on the other hand shows enriched areas on the left side of the sample (6.40 - 6.60 pfu). For the rest of the sample the content of Li is in the range of 6.10 - 6.40 pfu. The experiments also show a correlation between the amount of Al and Li. Areas with a high amount of lithium exhibit less aluminium and vice versa in accordance with the idea of charge balancing. The sample seems to be more or less divided into a side with more (≈ 0.30 pfu) and less (≈ 0.15 pfu) Al and also the edges follow this trend. A clear reason for

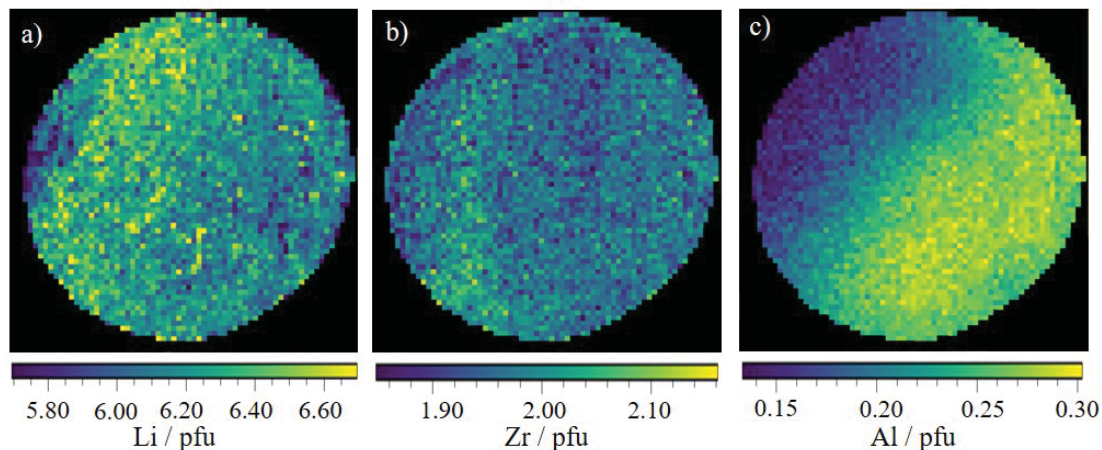


Figure 5.37: LA-ICP-OES measurements on sample A, illustrating the amount of a) Li, b) Zr and c) Al pfu in the sample.

these variations cannot be given yet, but possibly one edge of the sample exhibited a lower local lithium oxide activity in the gas phase. Thus stronger Li loss took place during sintering and created a driving force for Al diffusion. Having measured these elemental variations, it is now highly interesting to correlate it with the effects on ionic conduction.

In Figure 5.38 the content of a) Al and b) Li is plotted against the ionic conductivity. The dotted lines represent the expected amount of Al (0.20 pfu) and Li (6.40 pfu). On average, the measured Al content was higher and the measured Li content was lower than expected. A lower amount of lithium is not too surprising, due to its volatility during sintering. The behaviour of aluminium, however, is less straight forward to interpret. In other samples we found a correct overall Al content and thus we suspect that the local Al enrichment might be due to an inhomogeneous depth distribution of Al (Please note that our LA-ICP-OES method only probes the bulk composition near to the surface). When only considering sample A one might suspect a trend, i.e. a certain correlation between Al content and ionic conductivity with a maximum conductivity between 0.20 and 0.25 Al pfu. However, not only does this trend strongly scatter, it is also not reproduced by the other samples. The absence of a simple correlation between ionic conductivity and Al content is also supported by the fact that even for same Al content the conductivity

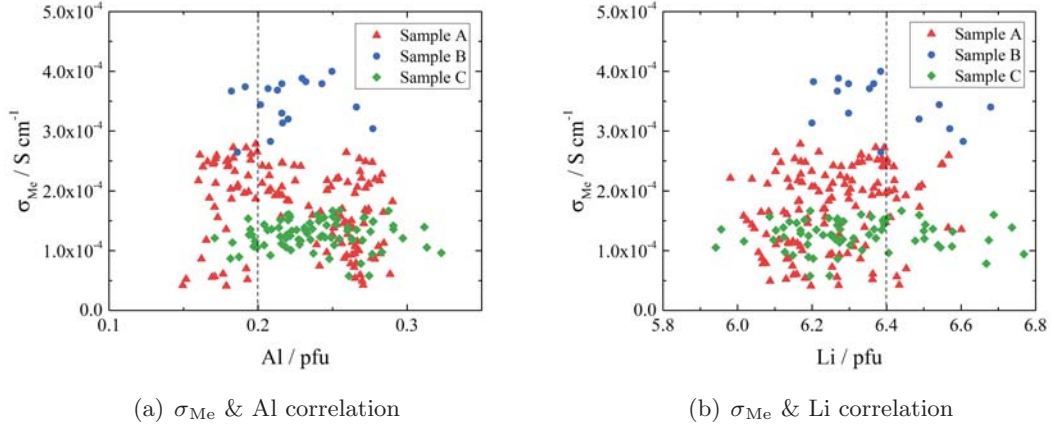


Figure 5.38: The conductivity of each measured microelectrode and the corresponding amount of a) Al and b) Li. The dotted line represents the intended composition, in the case of Al it was 0.20 pfu resulting in Li 6.40 pfu.

Table 5.14: Four different spots with two pairs of comparable stoichiometry but different ionic conductivities. The value for the oxygen is calculated based on charge balance considerations.

Spots	σ_{Me} [$S\text{ cm}^{-1}$]	Composition
Li enriched 1	1.87×10^{-4}	$\text{Li}_{6.43}\text{Al}_{0.20}\text{La}_3\text{Zr}_{1.96}\text{O}_{11.97}$
Li enriched 2	0.57×10^{-4}	$\text{Li}_{6.43}\text{Al}_{0.17}\text{La}_3\text{Zr}_{1.98}\text{O}_{11.93}$
Li poor 1	2.48×10^{-4}	$\text{Li}_{6.12}\text{Al}_{0.17}\text{La}_3\text{Zr}_{1.98}\text{O}_{11.69}$
Li poor 2	0.41×10^{-4}	$\text{Li}_{6.06}\text{Al}_{0.18}\text{La}_3\text{Zr}_{1.98}\text{O}_{11.76}$

can vary by almost an order of magnitude. Moreover, a high amount of lithium (> 6.40 pfu) does not lead to a higher conduction, as it was suggested in literature for a similar garnet composition [141].

This non-trivial composition conductivity relation is also obvious when comparing the conductivity and the stoichiometry of four different spots on sample A (Table 5.14). Two of them exhibited a rather high amount of 6.43 Li pfu, but achieved a low ($0.57 \times 10^{-4} S\text{ cm}^{-1}$) and an average ionic conductivity ($1.87 \times 10^{-4} S\text{ cm}^{-1}$). On the other hand, if the amount of lithium is too low (Li 6.06 - 6.12 pfu) the ionic conductivity can still be either moderate or five times lower. Overall, we thus conclude that there is yet no clear

trend observable how important the amount of Al and Li is for the ionic conductivity. Possibly details of the local crystallographic structure are much more important for the ionic conductivity than exact Al or Li contents. It is also worth mentioning that based on the measured cation concentration, the stoichiometric value of oxygen is calculated and is mostly below 12 pfu. This is in agreement with measurements using oxygen tracer exchange and secondary ion mass spectrometry (SIMS) which revealed the existence of oxygen vacancies [133]. Those may also affect the Li ionic conductivity.

5.6.3 Conclusion

Three different LLZO samples, stabilized with Al, were chemically and electrochemically characterized. Microelectrode measurements revealed the existence of distinct local conductivity variation within individual samples, but also differences between nominally identical samples. LA-ICP-OES was used to investigate the local chemical composition. Samples showed gradients in the Al and Li content and also deviations from the nominal values in near-surface regions (too much Al, too little Li). However, there is no clear trend visible how the elemental variation relates to the electrical performance. A high amount of Li does not lead to higher ionic conductivities than low amounts. It is very likely that another yet unknown parameter (e.g. local lattice or oxygen vacancies), has a higher impact on the ionic performance of LLZO than the local stoichiometry.

5.6.4 Supplementary

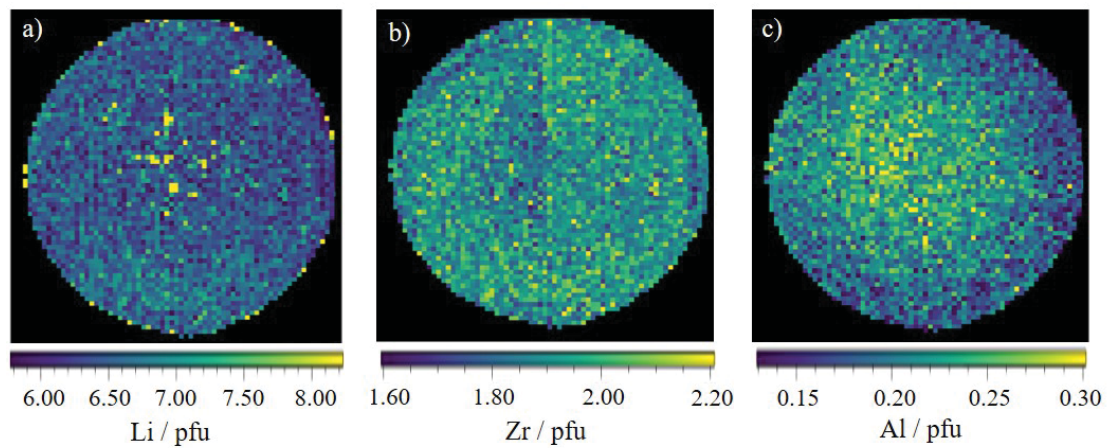


Figure 5.39: LA-ICP-OES measurements on sample B, illustrating the amount of a) lithium, b) zirconium and c) aluminium per formula unit in the sample.

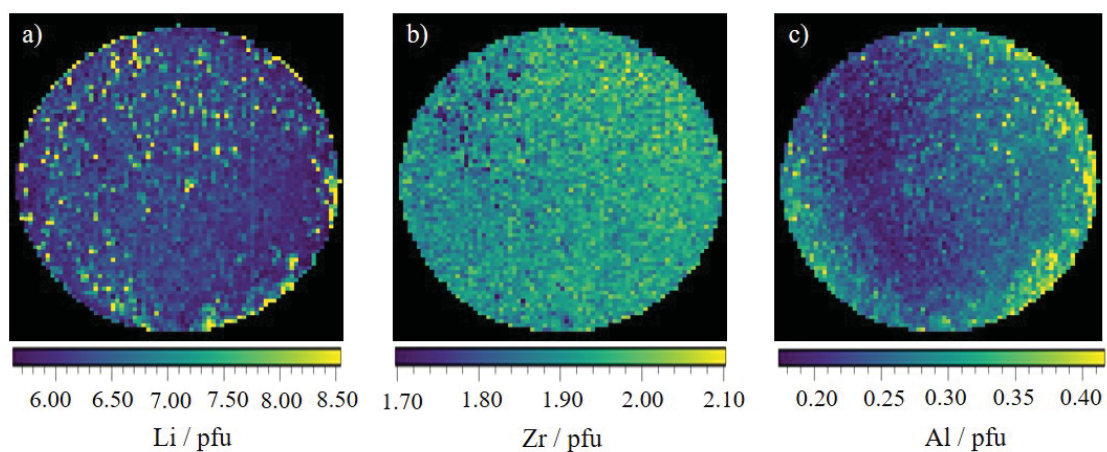


Figure 5.40: LA-ICP-OES measurements on sample C, illustrating the amount of a) lithium, b) zirconium and c) aluminium per formula unit in the sample.

Table 5.15: Parameters for the LA-ICP-OES measurement.

Laser ablation system	ESI NWR213	
Average fluence		
Pre-Ablation	2.50 J cm ⁻²	
Imaging	4.25 J cm ⁻²	
Laser diameter		
Pre-Ablation	250 μm	
Imaging	100 μm	
Scan speed		
Pre-Ablation	250 μm s ⁻¹	
Imaging	100 μm s ⁻¹	
Repetition rate	20 Hz	
Carrier gas flow (He)	0.6 l min ⁻¹	
Make-up gas flow (Ar)	0.8 l min ⁻¹	
ICP-OES instrumentation	Thermo iCAP 6500 RAD	
RF power	1200 W	
Radial observation height	12 mm	
Plasma gas flow	12 l min ⁻¹	
Auxiliary gas flow	0.5 l min ⁻¹	
Integration time	1 s	
Analytical wavelengths		
Al	309.271 nm	396.152 nm
La	261.034 nm	419.655 nm
Li	610.362 nm	670.784 nm
Zr	257.139 nm	274.256 nm

Table 5.16: Effective conductivities, obtained from macroelectrode measurements before and after heat treatment.

Atmosphere	Name	σ_{eff} [S cm ⁻¹]
AA	A	$2.27 \times 10^{-4} \rightarrow 5.92 \times 10^{-5}$
H ₂	B	$1.55 \times 10^{-4} \rightarrow 1.31 \times 10^{-4}$
N ₂	C	$2.20 \times 10^{-4} \rightarrow 2.27 \times 10^{-4}$
N ₂ wet	D	$1.66 \times 10^{-4} \rightarrow 2.31 \times 10^{-4}$

5.7 Effects of annealing

Macroelectrode measurements

In order to investigate the effects of annealing, Al (0.20 pfu) stabilized samples with sputtered Ti/Pt electrodes were heated for 1 hour at 700 °C in atmospheres like ambient air (AA), hydrogen (H₂) and nitrogen (N₂). In the text, samples will be referred to as A, B, C, D. To avoid any relation between LLZO and Ti/Pt, electrodes were removed before the annealing process.

Figure 5.41 a-d) illustrates the Nyquist plots of macroelectrode measurements for sample A, B, C and D in their pristine state (open circles) and after annealing in various atmospheres (open diamonds). Each sample shows a high frequency semicircle and a small shoulder in the mid frequency range followed by a low frequency contribution which represents the ionically blocking electrodes (Ti/Pt). For a proper quantification of the impedance spectra, the equivalent circuit as shown in Figure 5.12 was used.

The changes induced by the annealing step were rather small for three of four samples and the second semicircle only disappeared after annealing in wet nitrogen. As listed in Table 5.16, the effective conductivity of samples sintered in nitrogen or hydrogen hardly changed. The most pronounced changes were observed upon annealing in ambient air. Although the high frequency semicircle remained unchanged, the impedance of the second semicircle increased significantly, resulting in a drop of σ_{eff} from 2.27×10^{-4} to 5.92×10^{-5} S cm⁻¹.

The reason behind the increased impedance in the mid frequency range can have numer-

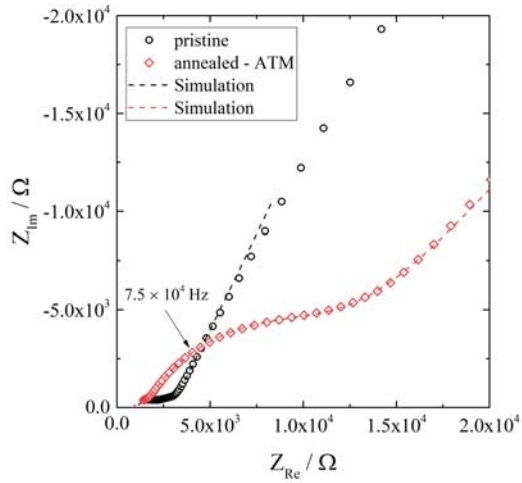
ous reasons. One possibility is the formation of a low conductive surface layer, but since the electrodes were removed before annealing and the sample polished before sputtering, we do not expect any contribution coming from a near surface layer. Another possibility is a grain boundary related phenomena. Based on calculations using the capacitance of the second semicircle, the total thickness of all grain boundaries would be around 30 μm which is not very realistic for grain boundaries. The most probable explanation is a temperature induced change of inhomogeneous phases within the sample. The extent of these inhomogeneities however, can not be estimated by macroelectrode impedance spectroscopy.

Microelectrode measurements

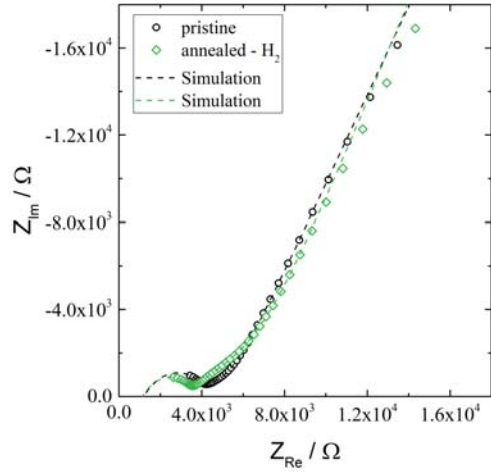
After macroelectrode measurements, the electrodes were used to prepare microelectrodes on top in order to investigate near surface effects caused by atmospheric and temperature treatment. Microelectrodes with a diameter between 10 and 300 μm were fabricated on top and measured at room temperature. Impedance spectra were analyzed by the equivalent circuit shown in 5.23. Figure 5.42 shows exemplary the impedance spectra of differently sized microelectrodes on samples annealed in a) ambient air, b) hydrogen, c) nitrogen and d) wet nitrogen. The high frequency feature is attributed to the ionic charge transport in the bulk followed by a capacitive response caused by the ionically blocking electrodes, just as explained in chapter 5.1.

The separation of bulk transport and blocking electrodes is less obvious in a) ambient air since the first semicircle is hardly visible; this is at least partly a consequence of the small bulk resistance. Figure 5.43 displays nominal σ_{me} values for different diameters, calculated by equation 5.7. Solid lines represent the effective conductivity, obtained from macroelectrode measurements before (black) and after the sintering step. The number of measured microelectrodes with a diameter smaller than 100 μm was limited, due to issues with interparticle and intraparticle porosity.

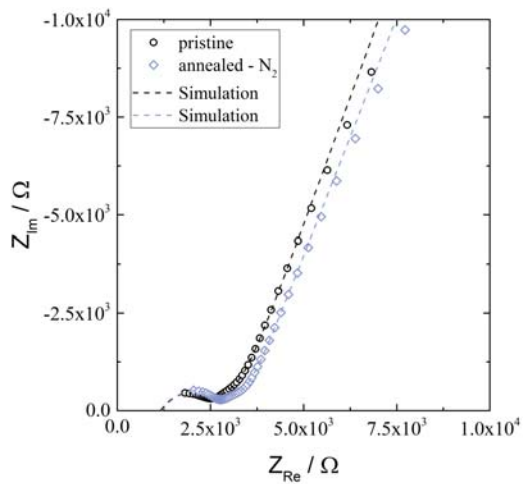
Some microelectrode measurements showed a relation between ionic conductivity and diameter of the microelectrode. This is not the case for the sample annealed in ambient air, simply due to the large scattering of σ_{me} . However, when comparing the conduc-



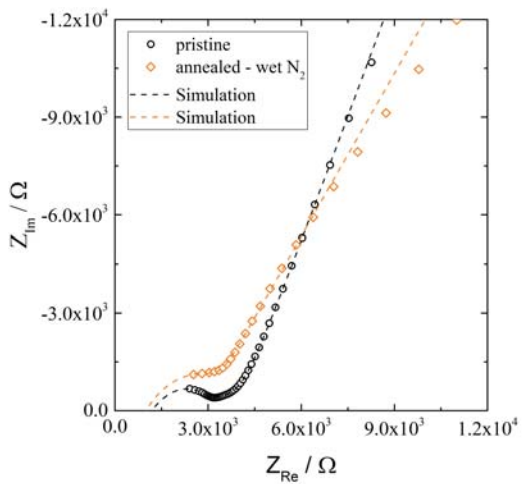
(a) Sample A - ambient air



(b) Sample B - hydrogen

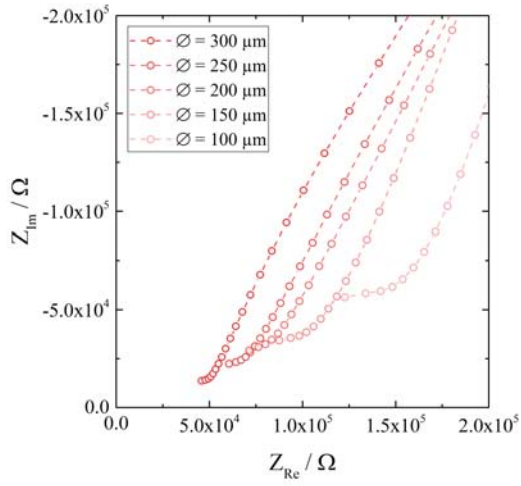


(c) Sample C - dry nitrogen

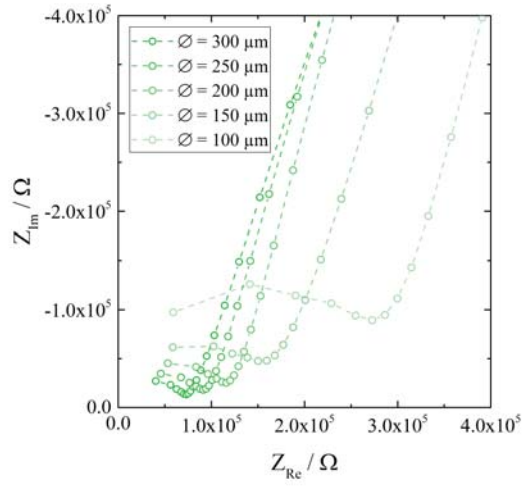


(d) Sample D - wet nitrogen

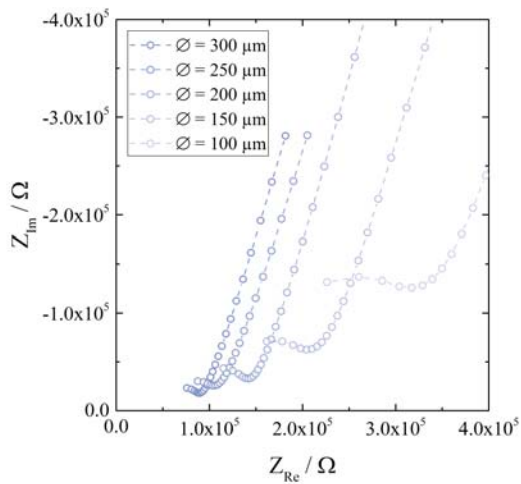
Figure 5.41: Nyquist plots of macroelectrode measurements before (blue) and after (red) annealing at 700 °C in a) ambient air, b) hydrogen, c) nitrogen and d) wet nitrogen. The impedance measurements were done at RT in ambient air.



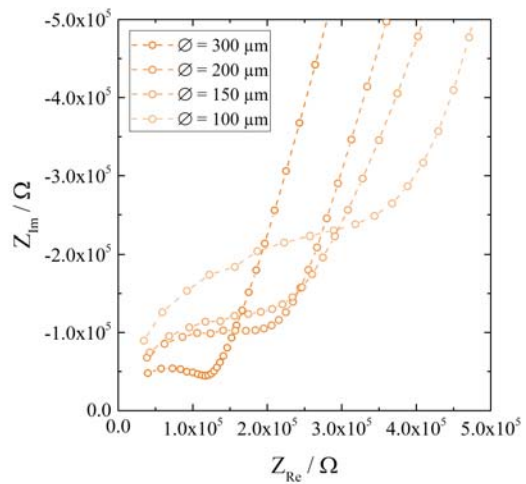
(a) Ambient air



(b) Hydrogen

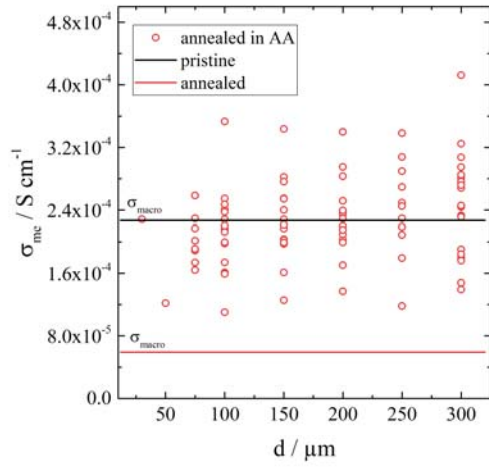


(c) Dry nitrogen

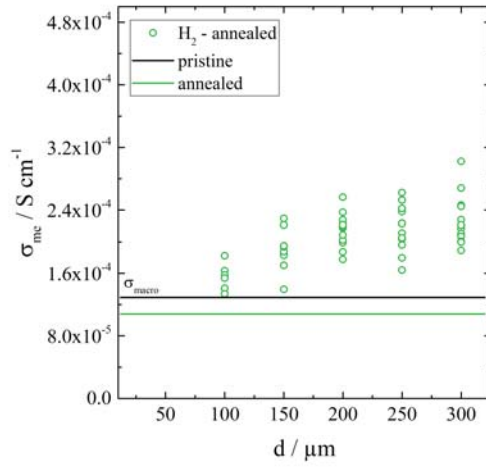


(d) Wet nitrogen

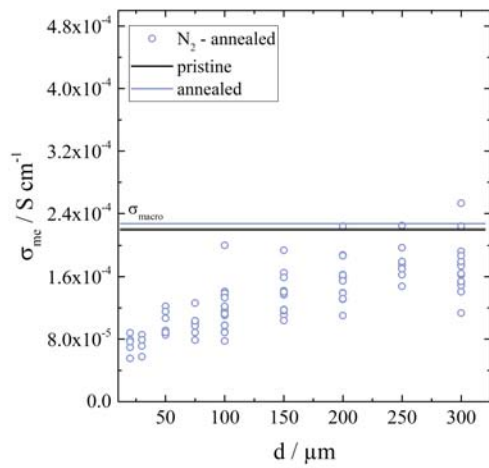
Figure 5.42: Microelectrode impedance measurements, investigating the effect of annealing in different atmospheres (a - d) near the surface. To probe depth variations in conductivity, microelectrodes with a diameter between 100 and 300 μm were applied on top and measured at room temperature.



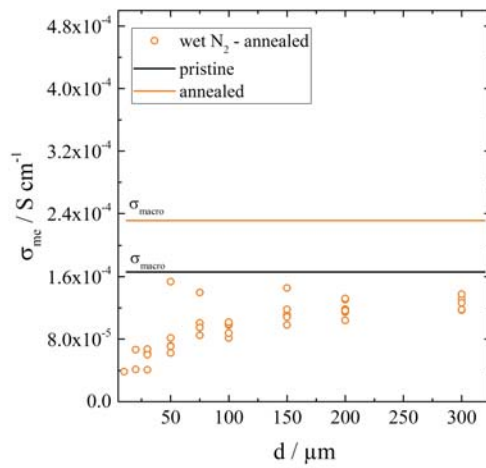
(a) Ambient air



(b) Hydrogen



(c) Dry nitrogen



(d) Wet nitrogen

Figure 5.43: Ionic conductivity obtained by microelectrode measurements on different diameters after annealing in a) AA, b) H_2 , c) N_2 and d) wet N_2 . Solid lines represent the effective conductivity obtained from macroelectrode measurements (Figure 5.41).

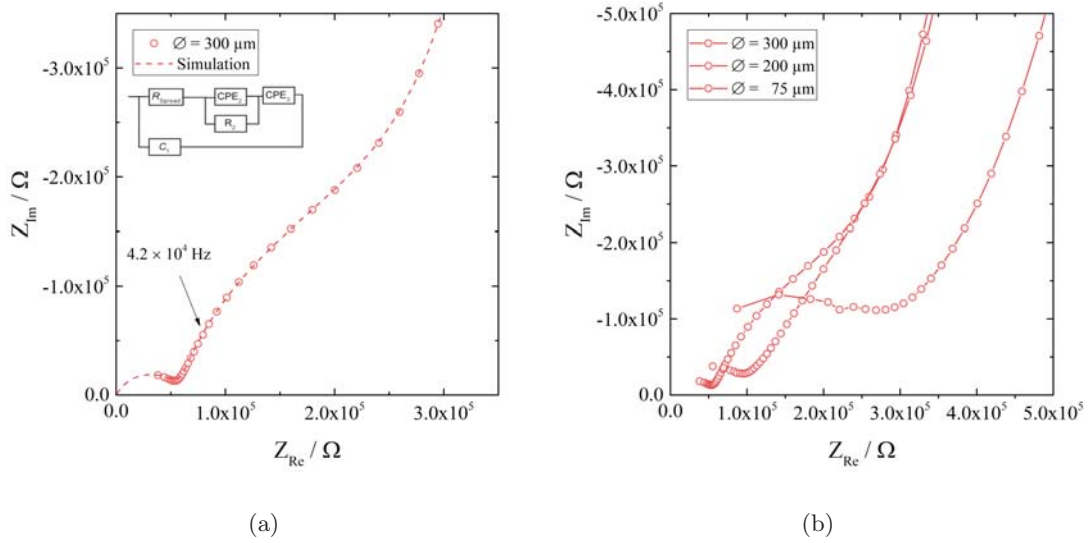


Figure 5.44: a) Impedance spectrum of a $300 \mu\text{m}$ electrode yielding an additional semi-circle, with the corresponding simulation (dashed line) based on the equivalent circuit shown above. b) The second semicircle disappears for smaller microelectrodes.

tivities of macro- and microelectrode measurements, the annealing in nitrogen seems to lower the ionic conductivity near the surface since macroelectrodes obtained higher conductivities than microelectrodes. On the other hand, samples which were sintered in hydrogen or ambient air, microelectrode measurements yielded similar or even better results as macroelectrode measurements. Macroelectrode measurements showed a significant drop in effective conductivity upon annealing in AA, which is not reflected by microelectrode measurements. Accordingly, the low conductive regions are not located near the surface of the sample. Instead they are probably located in the core of the sample, supporting the assumption of inhomogeneities responsible for the lower overall performance.

Inhomogeneities found by microelectrodes

In some areas, microelectrode measurements after annealing in ambient air, yielded an additional semicircle in the mid-frequency region. Figure 5.44 a) shows the impedance

Table 5.17: Calculated peak frequencies from the impedance spectra shown in Figure 5.44.

	300 μm	200 μm	75 μm	Macroelectrode
R [Ω]	2.52×10^5	2.91×10^5	2.35×10^5	9.74×10^3
C [F]	9.44×10^{-11}	8.20×10^{-11}	1.69×10^{-11}	1.38×10^{-9}
ω [Hz]	4.21×10^4	4.19×10^4	2.52×10^5	7.46×10^4

measurement of a 300 μm electrode with two semicircles. For properly simulating the impedance data, the equivalent circuit had then to be adapted by adding an additional R||CPE element. With decreasing electrode diameter, the contribution of this additional arc diminishes (Figure 5.44 b). In order to investigate if there is a correlation between the mid-frequency semicircle from macro- and microelectrode measurements, the peak frequency for both is calculated using

$$\omega = \frac{1}{RC}. \quad (5.11)$$

The resistive (R) and capacitive (C) values for micro- and macroelectrode measurements, as well as their calculated peak frequencies are listed in Table 5.17. The peak frequencies of the 300 μm electrode (4.21×10^4 Hz) and the macroelectrode (7.46×10^4 Hz) are very similar, supporting the assumption that those two semicircles share the same origin namely a low conductive inhomogeneity inside the sample.

5.8 Degradation of LLZO garnet material

Degradation in LLZO includes several different topics such as second phase formation in the garnet, interface formation or ion exchange reactions. To describe each kind of degradation and its effects would be out of the scope of this work. Therefore only some aspects of water induced degradation, including ionic performance, structural changes and chemical inertness will be discussed in this section.

Earlier studies claimed that LLZO is chemically stable against moisture [41]. This

misinterpretation was partly due to the fact that protonation can help to stabilize the cubic garnet structure and it does not necessarily slow down the ion conduction. Since then a lot of research has been done describing the exchange reaction between LLZO and H₂O and the consequences coming along with it [48, 57–60, 62, 63, 65–67, 124, 130–132, 138, 142–146].

5.8.1 Proton exchange

In case a LLZO sample is stored in ambient air, moisture starts the following chemical reaction: The initial reaction with LLZO and water from ambient air is



LiOH reacts with carbon dioxide



forming a lithiumcarbonate layer on the surface. The velocity at which such a layer forms depends on factors like storage, surface roughness, pretreatment, etc. A few days stored in ambient air are usually sufficient to see contributions from it in XRD patterns. As a consequence of the incorporation of protons into the garnet, the lattice constant starts to increase. Yow *et al.* investigated the lattice constant of LLZTO (Ta: 0.4 pfu) powder and pellets when immersed in water over 7 days by XRD (Table 5.18) [132]. The lattice constant of the powder became larger than for pellets, because a larger active surface area lead to faster protonation. The increased lattice constants are due to the replacement of Li-O bonds through weaker O-H bonds [57, 58, 65].

5.8.2 Site occupation

A reason why the effect of moisture has been missed in earlier studies was that protons have a beneficial effect on the ionic conductivity in the beginning. Generally speaking the incorporation of H⁺ ions results in a disordering of lithium which is a critical factor for fast lithium diffusion. The disordering usually implicates the distribution of Li-ions on

Table 5.18: Development of the lattice constant for $\text{Li}_{6.6}\text{La}_3\text{Zr}_{1.6}\text{Ta}_{0.4}\text{O}_{12}$ powder and pellet immersed in water [132].

days	powder	pellet
0	12.9378(3) Å	12.9403(3) Å
1	12.9924(7) Å	12.9473(3) Å
3	13.0274(7) Å	12.9493(3) Å
5	13.0377(6) Å	12.9551(3) Å
7	13.0530(8) Å	12.9606(4) Å

tetrahedral (24d) and preferably octahedral sites (48g, 96h), since we consider a cubic phase garnet. Different studies tried to analyze the level of occupation and the site preference of protons [57, 66, 67, 130, 131, 138, 146, 147]. Cheng Ma *et al.* investigated hot pressed LLZO immersed in water and proposed that tetrahedral sites are not affected by the Li^+/H^+ exchange reaction at all. Some Li-ions are exchanged on 48g sites but the majority is exchanged on 96h sites. This is in contrast to observations from other garnets, like $\text{Li}_5\text{La}_3\text{Ta}_2/\text{Nb}_2\text{O}_{12}$ where octahedral as well as tetrahedral sites participate in the Li^+/H^+ exchange reaction [130]. Based on the work of Li *et al.* for Al stabilized LLZO (Al 0.19 pfu) levels of site occupation are [49]:

- 24d - 36.0 %
- 48g - 25.0 %
- 96h - 31.7 %

Only a few publications quantified the amount of Li and H within the garnet. Larraz *et al.* found 3.8 Li pfu (54 %) and Galven *et al.* 2.25 (32 %) Li pfu after degradation [57, 66]. Furthermore there are differences between Li-5 and Li-7 stuffed garnets. Truong *et al.* performed similar experiments, using $\text{Li}_5\text{La}_3\text{M}_2\text{O}_{12}$ ($\text{M} = \text{Nb}, \text{Ta}$) as sample material. First they could show that a Li-5 stuffed garnet can be protonated even further than Li-7 stuffed garnets, leaving only 0.6 Li pfu (11 %) after the exchange reaction of $\text{Li}_5\text{La}_3\text{Nb}_2\text{O}_{12}$. Furthermore, they showed that the exchange reaction can be enhanced or slowed by B-site elemental variations. Instead of Nb, Ta was used on the

B-site and after the proton exchange reaction the remaining amount of Li pfu was 1.8 (36 %). The extent to which a garnet can sustain the Li^+/H^+ reaction is unknown. Long term impedance measurements on Mo stabilized LLZO (0.25 pfu) in wet oxygen ended with the decomposition of the garnet after 7 days in wet atmosphere. Two explanations are possible why the structural integrity was altered:

1. The extracted amount of Li passed the threshold of the garnet structure
2. Growing residuals between grains modified the sample until it decomposed

If all the Li could be extracted, then the garnet would be no longer a Li-stuffed garnet instead it would be a hydrogarnet.

5.8.3 Preparation

Lithium is a highly reactive element and as soon as a fresh source of Li (Li_2CO_3) is used, for example to weight educts for sample preparation, reaction with moisture will start immediately. Therefore, degradation will always be present, unless sample preparation and storage of educts is not entirely done in a sealed atmosphere. Sample preparation also included thermal treatment, meaning powder/samples are calcinated at $850\text{ }^\circ\text{C}$ / annealed at $1230\text{ }^\circ\text{C}$ for several hours. Thermo-gravimetric analysis (TGA) showed the following three steps during thermal treatment [132]:

I T: $\approx 250\text{ }^\circ\text{C}$ - evaporation of adsorbed surface water

II T: $\approx 400 - 450\text{ }^\circ\text{C}$ - release of H_2O from the garnet and of some CO_2

III T: $\approx 500 - 700\text{ }^\circ\text{C}$ - release of CO_2

Similar steps were found for a calcinated powder in slightly shifted temperature regimes (II: $\approx 340 - 550\text{ }^\circ\text{C}$ and III: $\approx 550 - 900\text{ }^\circ\text{C}$). A comparison between pellet and powder showed that step II starts earlier for a pellet, so there might be an additional reaction producing CO_2 . Larraz and Yow proposed the existence of quasi-amorphous hydrocar-

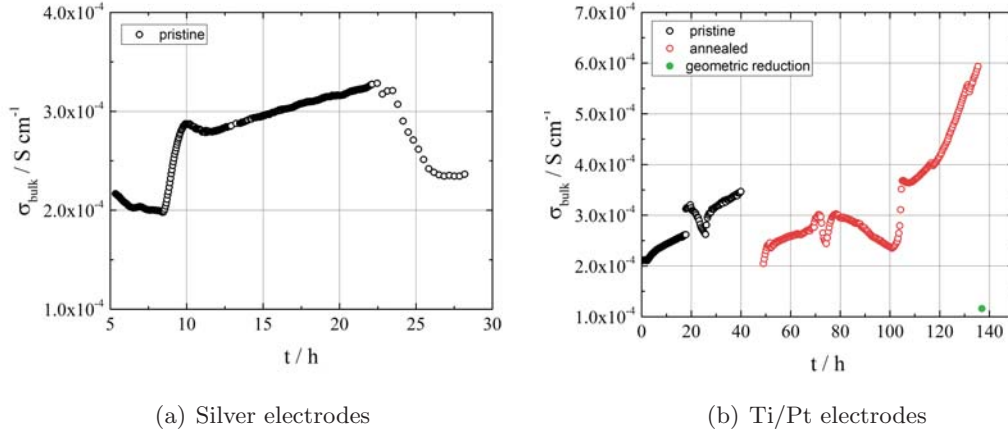
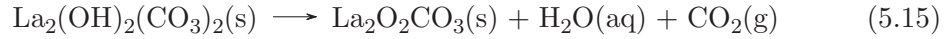
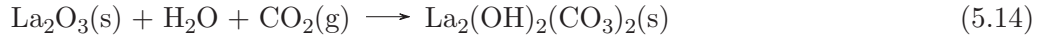


Figure 5.45: Conductivity development in wet atmosphere using a) porous silver electrodes and b) sputtered Ti/Pt electrodes.

bonates which decompose at these temperatures and release CO_2 .



Thus after some hours at 850°C the powder or sample should be free of carbonates and protons. However, upon cooling Larraz *et al.* could show the uptake of CO_2 around 500°C [59]. Below 200°C there is another noticeable weight gain, this time attributed to the uptake of H_2O or CO_2 [63].

Therefore sintering in ambient air always leads to reactions with water and carbon dioxide and the easiest way to avoid these contaminations is to use synthetic gases like N_2 , He, Ar, etc.

5.8.4 Results

Ionic conductivity and reversibility

Impedance measurements on Mo (0.25 pfu) stabilized LLZO were done to investigate the effect of moisture on the ionic performance of the sample. Measurements were made at RT in a wet oxygen atmosphere. In order to maximize the active surface

area for exchange reactions, porous silver electrodes were applied on both sides. Figure 5.45 a) displays the development of σ_{bulk} over 30 hours in wet oxygen. During the first hours the ionic conductivity dropped slightly, before σ_{bulk} started to increase from $1.97 \times 10^{-4} \text{ S cm}^{-1}$ to $3.26 \times 10^{-4} \text{ S cm}^{-1}$. After 24 hours the ionic conductivity decreased again. Reasons behind these conductivity variations remain unknown so far.

To make sure that the investigated effects are not a result of reactions between the electrode material and water, another sample was investigated using sputtered Ti/Pt layers as electrode material. The tightness of a sputtered layer should provide some protection against water driven reactions at the sites of the electrodes. Therefore, proton exchange reactions should mainly occur at the sample's sides.

Despite a different electrode material, similar conductivity fluctuations were observed. A first minor drop is followed by an improved ion conduction (Figure 5.45 b). In order to investigate the reversibility of the proton exchange reaction during 40 h, electrodes were removed and the sample was annealed at 700°C for 1 hour in ambient atmosphere before impedance measurements were continued. The new bulk conductivity was similar to the pristine value, which supports the assumption that protonation can be reversed. Continuing the impedance measurement in wet oxygen yielded again increased conductivities, but this time changes were more pronounced. The ionic conductivity started from $2.05 \times 10^{-4} \text{ S cm}^{-1}$ and reached a maximum of $5.93 \times 10^{-4} \text{ S cm}^{-1}$, before the measurement was stopped. An equilibration state had not been reached, so the ion conduction probably might have increased even further in a longer experiment.

One has to keep in mind that an ongoing exchange reaction reduces the contribution of charge transportation from Li-ions. Protonation transforms a Li-stuffed garnet into a hydrogarnet and a systematic study to understand the effects on partial conductivities has not been done yet.

At the beginning of Li^+/H^+ exchange reactions, only an outer shell of a grain is affected by this reaction. The rest is still Li-stuffed LLZO. Over time the protonated shell expands and lithium carbonate is likely deposited between grains or on the surface. In order to test, how far protonation has proceeded for the investigated sample in Figure 5.45 b), parts of the sample were removed by sandpaper. As a result the bulk conductivity

dropped from 5.93×10^{-4} to 1.16×10^{-4} S cm⁻¹ (green point - Figure 5.45 b) which is the lowest bulk conductivity measured for this sample.

The loss in ion conduction can be attributed to the diameter reduction, a similar phenomenon has been shown in Chapter 5.1. There, conductivity fluctuations were attributed to inhomogeneous elemental distributions and not to degradational effects since samples were quickly measured after their preparation. However, a connection between both experiments can not be ruled out since protonation starts immediately when the sample is cooled after the annealing step. Therefore, the condition of the sample in terms of protonation progression is not known and can as well play a larger role than expected.

Chapter 6

Summary

The ionic conductivity of many LLZO samples of different composition and preparation procedure or pretreatment could be characterized in detail by impedance spectroscopy. It was shown that microelectrodes ($\varnothing : 20 - 300 \mu\text{m}$) can be successfully applied to a polycrystalline LLZO garnet sample and allowed microelectrode impedance spectroscopy studies. Those resulted in local information on bulk ionic conductivities. A comparison between the effective conductivity of the overall sample and conductivities of local areas of the sample revealed differences. Locally, conductivities were up to twice the effective bulk conductivity with a maximum local value of $6.3 \times 10^{-4} \text{ S cm}^{-1}$. Moreover, smaller microelectrodes lead to smaller nominal conductivities which indicates that near to the surface less conductive regions exist. The sensitivity of microelectrodes towards near-surface resistive changes was also used to investigate how exposure to ambient air affects the properties of LLZO samples. A substantial degradation of the local conductivity was found, particularly for small microelectrodes.

In order to further investigate the extent of degradation, samples were sintered in different atmospheres (N_2 , wet N_2 , H_2 , ambient air) and investigated by measurements using macro- and microelectrodes. While the overall sample performance hardly changed (except for one sample most likely due to an inhomogenous phase), local conductivity measurements again confirmed the existence of a low conductive area near surface.

Reasons behind local conductivity variations were further investigated by a combination of impedance spectroscopy and LA-ICP-OES. Three different LLZO samples, stabilized

with Al, were therefore chemically and electrochemically characterized. Microelectrode measurements revealed the existence of distinct local conductivity variation within individual samples, but also differences between the samples. LA-ICP-OES was used to investigate the local chemical composition. Samples showed gradients in the Al and Li content and also deviations from the nominal values in near-surface regions (too much Al, too little Li). However, there is no clear trend visible how the elemental variation relates to the electrical performance. A high amount of Li does not lead to higher ionic conductivities than low amounts. It is very likely that another yet unknown parameter (e.g. local lattice or oxygen vacancies) has a higher impact on the ionic performance of LLZO than the local stoichiometry.

In order to investigate the reproducibility of the sintering method and the homogeneity of the ionic conductivity on a large scale, numerous Al-stabilized LLZO samples with identical Al contents were prepared by a nominally identical solid state route and sintered at 1150 °C and 1230 °C, respectively. In the best case, effective sample conductivities of about $8 \times 10^{-4} \text{ S cm}^{-1}$ were obtained, which is among the highest values ever reported for Al stabilized LLZO. In other cases, effective values with less than $10^{-4} \text{ S cm}^{-1}$ were found. XRPD measurements could not resolve reasons for these variations. The diameter of several samples was changed by grinding and the samples were repeatedly analyzed using EIS, which revealed pronounced spatial inhomogeneities in the ionic conductivity. In most cases the peripheral parts showed higher conductivities than the central sample parts. For thicker samples ($> 2.5 \text{ mm}$) additional non-idealities come into play: grinding experiments revealed the existence of unwanted side phases near the sample's core which were not observed by XRD of the pristine sample, since the penetration depth of the X-rays was too small.

Chapter 7

Acknowledgment

Nachdem so viel über Lithium geschrieben wurde, kommt nun der Teil in der Arbeit in dem ich mich bei allen bedanken möchte mit denen ich in den letzten 3 Jahren viel zu tun hatte und die bewusst oder unbewusst dazu beigetragen haben, die Diss zu schreiben. Zu sagen das die letzten drei Jahre ohne Probleme über die Bühne liefen wäre eine glatte Lüge. Es gab jede Menge Pannen und Rückschläge und doch hatte ich nie das Gefühl verloren zu sein. Das lag vor allem an der tollen Betreuung durch meinen Professor, den ich sogar soweit gebracht habe wieder ins Labor zu gehen und mit mir Impedanz zu messen. Ein weiterer Grund dafür waren unsere Kollegen aus Salzburg: Prof. Amthauer, Reini und Daniel. Die Gewissenhaftigkeit und Hingabe mit der ihr an diesem Gebiet gearbeitet habt war extrem motivierend. Unsere vielen Skype-Diskussionen werde ich nie vergessen. Ein Dankeschön geht auch an die Arbeitsgruppe Limbeck, die Methodentwicklung war verdammt viel Arbeit - Kudos Stefan!

Neben externen Arbeitsgruppen möchte ich mich auch bei meinen Arbeitskollegen bedanken. Das Klima und der Umgang miteinander machten aus dem Erdgeschoss einen tollen Arbeitsplatz. Gut, nehmen wir das Untergeschoss auch noch dazu, immerhin ist der Werner auch ein Unikat. Besonders lustig waren die Selbsthilfegruppen die sich regelmäßig in unserem Zimmer formierten. Mein Arbeitszimmer → super cool (dazu zählen auch vergangene Zimmergenossen - einmal BC EG A20 - immer BC EG A20) Auch einen großen Dank an das gesamte Sekretariat das mir über die Jahre ans Herz gewachsen ist.

Motivation und Inspiration habe ich mir nicht nur von Leuten in der Arbeit geholt sondern auch von außerhalb. Ohne der Unterstützung der Familien-Clans WeWaHuGr wäre Operation Dissertation nicht möglich gewesen. Vor allem kleine Gesten wie übervolle Teller zu Mittag, kiloweise Gemüselieferungen, Bremskeile von Tortenstücken ließen meine wissenschaftlichen Probleme kurzzeitig lächerlich erscheinen.

Danken möchte ich auch meinen Freunden (Heroes never die) und meinen Kollegen im TKD Verein (#5). Ein besonderer Dank an Mighty T, deren Freude und Herzlichkeit im Training mich über so manch schwierigen Tag gerettet hat.

Und die letzten Worte gehören meiner Frau:

Applaus, Applaus

Für deine Worte

Mein Herz geht auf

Wenn du lachst!

Applaus, Applaus

Für deine Art mich zu begeistern

Hör niemals damit auf!

Ich wünsch' mir so sehr

Du hörst niemals damit auf

Chapter 8

Curriculum Vitae

Andreas WACHTER-WELZL

Oberhoferstrasse 7a/2/10

2130 Mistelbach

* 31.08.1986 (AUT)

✉ Andreas.Wachter-Welzl@gmx.at

☎ +43 660 641 1391

Wissenschaftlicher Werdegang

DISSERTATION IN TECHNISCHER CHEMIE

Prof. Jürgen Fleig

08/2014 –
2017

„Local conductivities in Li ion conducting garnet-based ceramics“

Elektrochemische Analyse und Optimierung von Lithium leitenden Festoxidelektrolyten.

Technische Universität Wien, 1060 Wien

MASTER IN ENERGIETECHNIK

Prof. Jürgen Fleig

10/2011 –
07/2014

„Spannungs- und Partialdruckabhängigkeit des Polarisationswiderstands von LaMnO₃-Elektroden auf Festelektrolyten“

Untersuchung des Zusammenhangs zwischen Partialdruck und Spannung auf die Reaktionskinetik von Brennstoffzellenelektroden.

Technische Universität Wien, 1060 Wien

AUSLANDSSEMESTER

10/2012 –
03/2013

*Humboldt-Universität zu Berlin und
Technische Universität Berlin, Deutschland*

BACHELOR IN TECHNISCHER PHYSIK

09/2006 –
07/2011

Technische Universität Wien, 1060 Wien

ABSCHLUSS HANDELSAKADEMIE

09/2000 –
07/2005

Schwerpunkt: Informationsmanagement und Informationstechnologie

Bundeshandelsakademie, 2130 Mistelbach

Technische Kenntnisse

Elektrochemische Analyse:	Impedanzspektroskopie (EIS), DC-Messungen
Elementanalyse:	Röntgenspektroskopie (XRF)
Mikrostrukturanalyse:	Pulver- und Dünnschicht-Röntgendiffraktometrie (XRD), Elektronenmikroskopie (SEM)
Materialwissenschaften:	Herstellung von Oxidgranaten über Sol Gel und Sinterung
Dünnschichten:	Erzeugung von Dünnschichten mit Hilfe von Sputterdeposition und Laserstrahlverdampfung (PLD), Nanostrukturierung mittels Lithografie
Programmiersprachen:	<ul style="list-style-type: none">• C, C++, C#• Assembler• MySQL• LabView• CSS

Kenntnisse & Fähigkeiten

SPRACHEN

Deutsch	Muttersprache
Englisch	Fließend in Wort und Schrift
Französisch	Maturaniveau
Ungarisch	Anfängerniveau

PC-KENNTNISSE

MS-Office, Origin, SAP, Internet und Social Media

Soft Skills

verantwortungsvoll, koordiniert	Einhaltung von Projektmeilensteinen, Anleitung von Mitarbeitern (Praktikanten, Diplomanden)
strategisch, analytisch	Frühzeitiges Erkennen von Problemen und gezielte Vermeidung
kontaktfreudig	Angriff neuer Themengebiete mit Kooperationspartnern (Nasicon, Bioimpedanz, LCO - Elektroden)
präsentationserfahren	Vorträge auf internationalen Konferenzen (USA, Deutschland)
wissbegierig, strebsam	Vertiefende Fortbildungen in zusätzlichen Themengebieten (Röntgendiffraktometrie, Kinetik und Katalyse, Elektronik, ...)

Kooperationen

Austrian Institute of Technology, Universität Salzburg, Österreich (Projekt SoLiK)
Forschungszentrum Jülich, Deutschland (Dr. Frank Tietz)
ETH Zürich, Schweiz (Dr. Jennifer Rupp)
Massachusetts Institute of Technology, USA (Dr. Daniel Rettenwander)

Publikationen

Hauptautor	<i>The effects of stoichiometric changes on the local ionic conductivity</i> Andreas Wachter-Welzl , S. Smetacek, R. Wagner, D. Rettenwander, S. Taibl, G. Amthauer, A. Limbeck, J. Fleig; <i>in preparation</i> (2017)
Hauptautor	<i>The origin of conductivity variations in Al-stabilized $\text{Li}_7\text{La}_3\text{Zr}_2\text{O}_{12}$ ceramics</i> Andreas Wachter-Welzl , J. Kirowitz, R. Wagner, S. Smetacek, G. C. Brunauer, M. Bonta, D. Rettenwander, S. Taibl, A. Limbeck, G. Amthauer, J. Fleig; <i>submitted</i> (2017)
Hauptautor	<i>Microelectrodes for local conductivity and degradation measurements on Al stabilized $\text{Li}_7\text{La}_3\text{Zr}_2\text{O}_{12}$ garnets</i> Andreas Wachter-Welzl , R. Wagner, D. Rettenwander, S. Taibl, G. Amthauer, J. Fleig; <i>Journal of Electrochemistry</i> (2016)
Mitautor	<i>A Novel Application for Low Frequency Electrochemical Impedance Spectroscopy as an Online Process Monitoring Tool for Viable Cell Concentrations</i> Christoph Slouka, D. J. Wurm, G. Brunauer, A. Wachter-Welzl , O. Spadiut, J. Fleig and C. Herwig; <i>Sensors</i> (2016)
Mitautor	<i>Structural and Electrochemical Consequences of Al and Ga co-substitution in $\text{Li}_7\text{La}_3\text{Zr}_2\text{O}_{12}$ Solid Electrolytes</i> Daniel Rettenwander, G. Redhammer, F. Preishuber-Pflügl, L. Cheng, L. Miara, R. Wagner, A. Welzl , E. Suard, M. M. Doeff, M. Wilkening, J. Fleig, and G. Amthauer; <i>Chemistry of Materials</i> (2016)
Mitautor	<i>Fast Li-ion conducting $\text{Li}_{7-3x}\text{Fe}_x\text{La}_3\text{Zr}_2\text{O}_{12}$ with uncommon I-43d structure</i> Reinhard Wagner, Günther J. Redhammer, D. Rettenwander, G. Tippelt, A. Welzl , S. Taibl, J. Fleig, A. Franz, W. Lottermoser and G. Amthauer; <i>Chemistry of Materials</i> (2016)
Mitautor	<i>A microcontact impedance study on NASICON-type $\text{Li}_{1+x}\text{Al}_x\text{Ti}_{2-x}(\text{PO}_4)_3$ ($0 \leq x \leq 0.5$) single crystals</i> D. Rettenwander, A. Welzl , S. Pristat, F. Tietz, S. Taibl, G. J. Redhammer and J. Fleig; <i>Materials Chemistry A</i> (2015)
Mitautor	<i>Synthesis, Crystal Chemistry, and Electrochemical Properties of $\text{Li}_{7-2x}\text{La}_3\text{Zr}_2\text{-xMo}_x\text{O}_{12}$ ($x = 0.1-0.4$): Stabilization of the Cubic Garnet Polymorph via Substitution of Zr^{4+} by Mo^{6+}</i> Daniel Rettenwander, A. Welzl , L. Cheng, J. Fleig, M. Musso, E. Suard, M. M. Doeff, G. J. Redhammer and G. Amthauer; <i>Inorganic Chemistry</i> (2015)
Mitautor	<i>Electrochemical properties of $\text{La}_{0.6}\text{Sr}_{0.4}\text{CoO}_{3-\delta}$ thin films investigated by complementary impedance spectroscopy and isotope exchange depth profiling</i> Markus Kubicek, T. M. Huber, A. Welzl , A. Penn, G. M. Rupp, J. Bernardi, M. Stöger-Pollach, H. Hutter and J. Fleig; <i>Solid State Ionics</i> (2014)

Mitautor *Design of a novel pulsed spin resonator for the beta-decay experiment PERC*
Christoph Gösselsberger, H. Abele, G. Badurek, E. Jericha, S. Nowak, G. Wautischer and **A. Welzl**; *Physics Procedia* (2011)

Konferenzen

Vortrag

MRS – Dez 2016
Boston
USA

Inhomogeneous conductivities in $\text{Li}_7\text{La}_3\text{Zr}_2\text{O}_{12}$ ceramics investigated by spatially resolved impedance spectroscopy and elemental analytics

Vortrag

SSB – Nov 2016
Frankfurt
Germany

Inhomogeneous conductivities in $\text{Li}_7\text{La}_3\text{Zr}_2\text{O}_{12}$ ceramics investigated by spatially resolved impedance spectroscopy and elemental analytics

Poster Präsentation

GDCH – Sept 2016
Frankfurt
Germany

The implication of inhomogeneities in $\text{Li}_7\text{La}_3\text{Zr}_2\text{O}_{12}$ ceramics

Poster Präsentation

ECSSC – Aug 2015
Vienna
Austria

Local conductivities in Li ion conducting garnet-based ceramics measured by microelectrodes

Poster Präsentation

SoLiK – Jun 2015
Vienna
Austria

Local conductivities in Li ion conducting garnet-based ceramics measured by microelectrodes

Poster Präsentation

EMRS – Mai 2014
Lille
France

The Voltage Dependence of Oxygen Reduction Pathways on Strontium-Doped Lanthanum Manganite (LSM) Model Electrodes

Chapter 9

Bibliography

- [1] P. Atkins, *Shriver and Atkins' inorganic chemistry*. Oxford University Press, USA, 2010.
- [2] "Battery cell comparison," 2017.
- [3] M. S. Whittingham, "Electrical energy storage and intercalation chemistry," *Science*, vol. 192, no. 4244, pp. 1126–1127, 1976.
- [4] "Sony keyword 01," 1991.
- [5] N. A. Kaskhedikar and J. Maier, "Lithium storage in carbon nanostructures," *Advanced Materials*, vol. 21, no. 25-26, pp. 2664–2680, 2009.
- [6] M. Levi and D. Aurbach, "Diffusion coefficients of lithium ions during intercalation into graphite derived from the simultaneous measurements and modeling of electrochemical impedance and potentiostatic intermittent titration characteristics of thin graphite electrodes," *The Journal of Physical Chemistry B*, vol. 101, no. 23, pp. 4641–4647, 1997.
- [7] E. Markevich, M. Levi, and D. Aurbach, "Comparison between potentiostatic and galvanostatic intermittent titration techniques for determination of chemical diffusion coefficients in ion-insertion electrodes," *Journal of Electroanalytical Chemistry*, vol. 580, no. 2, pp. 231–237, 2005.

- [8] K. Persson, V. A. Sethuraman, L. J. Hardwick, Y. Hinuma, Y. S. Meng, A. van der Ven, V. Srinivasan, R. Kostecki, and G. Ceder, "Lithium diffusion in graphitic carbon," *The Journal of Physical Chemistry Letters*, vol. 1, no. 8, pp. 1176–1180, 2010.
- [9] T. Hatchard and J. Dahn, "In situ XRD and electrochemical study of the reaction of lithium with amorphous silicon," *Journal of The Electrochemical Society*, vol. 151, no. 6, pp. A838–A842, 2004.
- [10] R. Chandrasekaran, A. Magasinski, G. Yushin, and T. F. Fuller, "Analysis of lithium insertion/deinsertion in a silicon electrode particle at room temperature," *Journal of the Electrochemical Society*, vol. 157, no. 10, pp. A1139–A1151, 2010.
- [11] B. Laforge, L. Levan-Jodin, R. Salot, and A. Billard, "Study of germanium as electrode in thin-film battery," *Journal of the Electrochemical Society*, vol. 155, no. 2, pp. A181–A188, 2008.
- [12] L. Baggetto and P. H. Notten, "Lithium-ion (de) insertion reaction of germanium thin-film electrodes: an electrochemical and in situ xrd study," *Journal of The Electrochemical Society*, vol. 156, no. 3, pp. A169–A175, 2009.
- [13] J. L. Tirado, "Inorganic materials for the negative electrode of lithium-ion batteries: state-of-the-art and future prospects," *Materials Science and Engineering: R: Reports*, vol. 40, no. 3, pp. 103–136, 2003.
- [14] J. Xie, N. Imanishi, A. Hirano, Y. Takeda, O. Yamamoto, X. Zhao, and G. Cao, "Li-ion diffusion behavior in Sn, SnO and SnO₂ thin films studied by galvanostatic intermittent titration technique," *Solid State Ionics*, vol. 181, no. 35, pp. 1611–1615, 2010.
- [15] R. Fong, U. Von Sacken, and J. R. Dahn, "Studies of lithium intercalation into carbons using nonaqueous electrochemical cells," *Journal of The Electrochemical Society*, vol. 137, no. 7, pp. 2009–2013, 1990.

- [16] Y. Ein-Eli, B. Markovsky, D. Aurbach, Y. Carmeli, H. Yamin, and S. Luski, “The dependence of the performance of Li-C intercalation anodes for Li-ion secondary batteries on the electrolyte solution composition,” *Electrochimica Acta*, vol. 39, no. 17, pp. 2559–2569, 1994.
- [17] P. Stallworth, J. Fontanella, M. Wintersgill, C. D. Scheidler, J. J. Immel, S. Greenbaum, and A. Gozdz, “NMR, DSC and high pressure electrical conductivity studies of liquid and hybrid electrolytes,” *Journal of Power Sources*, vol. 81, pp. 739–747, 1999.
- [18] A. M. Andersson, M. Herstedt, A. G. Bishop, and K. Edström, “The influence of lithium salt on the interfacial reactions controlling the thermal stability of graphite anodes,” *Electrochimica Acta*, vol. 47, no. 12, pp. 1885–1898, 2002.
- [19] K. Hayamizu, Y. Aihara, H. Nakagawa, T. Nukuda, and W. S. Price, “Ionic conduction and ion diffusion in binary room-temperature ionic liquids composed of [emim][BF₄] and LiBF₄,” *The Journal of Physical Chemistry B*, vol. 108, no. 50, pp. 19527–19532, 2004.
- [20] R. Dominko, M. Bele, J.-M. Goupil, M. Gaberscek, D. Hanzel, I. Arcon, and J. Jamnik, “Wired Porous Cathode Materials: A Novel Concept for Synthesis of LiFePO₄,” *Chemistry of Materials*, vol. 19, no. 12, pp. 2960–2969, 2007.
- [21] M. M. Doeff, J. D. Wilcox, R. Kostecki, and G. Lau, “Optimization of carbon coatings on LiFePO₄,” *Journal of Power Sources*, vol. 163, no. 1, pp. 180–184, 2006.
- [22] M. M. Doeff, J. D. Wilcox, R. Yu, A. Aumentado, M. Marcinek, and R. Kostecki, “Impact of carbon structure and morphology on the electrochemical performance of LiFePO₄/C composites,” *Journal of Solid State Electrochemistry*, vol. 12, no. 7-8, pp. 995–1001, 2008.
- [23] J. Cho, Y.-W. Kim, B. Kim, J.-G. Lee, and B. Park, “A breakthrough in the safety of lithium secondary batteries by coating the cathode material with

- AlPO₄ nanoparticles,” *Angewandte Chemie International Edition*, vol. 42, no. 14, pp. 1618–1621, 2003.
- [24] T. Ohzuku, A. Ueda, and M. Nagayama, “Electrochemistry and structural chemistry of LiNiO₂ (R3m) for 4 volt secondary lithium cells,” *Journal of the Electrochemical Society*, vol. 140, no. 7, pp. 1862–1870, 1993.
- [25] P. Bruce, A. Robert Armstrong, and R. Gitzendanner, “New intercalation compounds for lithium batteries: layered LiMnO₂,” *Journal of Materials Chemistry*, vol. 9, no. 1, pp. 193–198, 1999.
- [26] F. Lin, I. M. Markus, D. Nordlund, T.-C. Weng, M. D. Asta, H. L. Xin, and M. M. Doeff, “Surface reconstruction and chemical evolution of stoichiometric layered cathode materials for lithium-ion batteries,” *Nature Communications*, vol. 5, p. 3529, 2014.
- [27] A. Robertson, A. West, and A. Ritchie, “Review of crystalline lithium-ion conductors suitable for high temperature battery applications,” *Solid State Ionics*, vol. 104, no. 1, pp. 1–11, 1997.
- [28] G.-y. Adachi, N. Imanaka, and H. Aono, “Fast Li⁺ conducting ceramic electrolytes,” *Advanced Materials*, vol. 8, no. 2, pp. 127–135, 1996.
- [29] V. Thangadurai and W. Weppner, “Recent progress in solid oxide and lithium ion conducting electrolytes research,” *Ionics*, vol. 12, no. 1, pp. 81–92, 2006.
- [30] S. Stramare, V. Thangadurai, and W. Weppner, “Lithium lanthanum titanates: a review,” *Chemistry of Materials*, vol. 15, no. 21, pp. 3974–3990, 2003.
- [31] F. Abbattista, M. Vallino, and D. Mazza, “Remarks on the binary systems Li₂O Me₂O₅ (Me Nb, Ta),” *Materials Research Bulletin*, vol. 22, no. 8, pp. 1019–1027, 1987.
- [32] H. Hyooma and K. Hayashi, “Crystal structures of La₃Li₅M₂O₁₂ (M= Nb, Ta),” *Materials Research Bulletin*, vol. 23, no. 10, pp. 1399–1407, 1988.

- [33] V. Thangadurai, H. Kaack, and W. J. Weppner, “Novel Fast Lithium Ion Conduction in Garnet-Type $\text{Li}_5\text{La}_3\text{M}_2\text{O}_{12}$ (M= Nb, Ta),” *Journal of the American Ceramic Society*, vol. 86, no. 3, pp. 437–440, 2003.
- [34] V. Thangadurai, S. Narayanan, and D. Pinzaru, “Garnet-type solid-state fast Li ion conductors for Li batteries: critical review,” *Chemical Society Reviews*, vol. 43, no. 13, pp. 4714–4727, 2014.
- [35] M. P. O’Callaghan, D. R. Lynham, E. J. Cussen, and G. Z. Chen, “Structure and Ionic-Transport Properties of Lithium-Containing Garnets $\text{Li}_3\text{Ln}_3\text{Te}_2\text{O}_{12}$ (Ln= Y, Pr, Nd, Sm- Lu),” *Chemistry of Materials*, vol. 18, no. 19, pp. 4681–4689, 2006.
- [36] M. P. O’Callaghan and E. J. Cussen, “Lithium dimer formation in the Li-conducting garnets $\text{Li}_{5+x}\text{Ba}_x\text{La}_{3-x}\text{Ta}_2\text{O}_{12}$ ($0 \leq x \leq 1.6$),” *Chemical Communications*, no. 20, pp. 2048–2050, 2007.
- [37] J. Awaka, N. Kijima, Y. Takahashi, H. Hayakawa, and J. Akimoto, “Synthesis and crystallographic studies of garnet-related lithium-ion conductors $\text{Li}_6\text{CaLa}_2\text{Ta}_2\text{O}_{12}$ and $\text{Li}_6\text{BaLa}_2\text{Ta}_2\text{O}_{12}$,” *Solid State Ionics*, vol. 180, no. 6, pp. 602–606, 2009.
- [38] J. D. Percival, *Synthesis and characterisation of novel lithium Ion containing garnet-related materials for potential lithium Ion battery applications*. PhD thesis, University of Surrey, 2009.
- [39] H. Xie, J. A. Alonso, Y. Li, M. T. Fernández-Díaz, and J. B. Goodenough, “Lithium distribution in aluminum-free cubic $\text{Li}_7\text{La}_3\text{Zr}_2\text{O}_{12}$,” *Chemistry of Materials*, vol. 23, no. 16, pp. 3587–3589, 2011.
- [40] D. Rettenwander, A. Welzl, L. Cheng, J. Fleig, M. Musso, E. Suard, M. M. Doeff, G. J. Redhammer, and G. Amthauer, “Synthesis, Crystal Chemistry, and Electrochemical Properties of $\text{Li}_{7-2x}\text{La}_3\text{Zr}_{2-x}\text{Mo}_x\text{O}_{12}$ ($x = 0.1 - 0.4$): Stabilization of the Cubic Garnet Polymorph via Substitution of Zr^{4+} by Mo^{6+} ,” *Inorganic chemistry*, vol. 54, no. 21, pp. 10440–10449, 2015.

- [41] R. Murugan, V. Thangadurai, and W. Weppner, "Fast lithium ion conduction in garnet-type $\text{Li}_7\text{La}_3\text{Zr}_2\text{O}_{12}$," *Angewandte Chemie International Edition*, vol. 46, no. 41, pp. 7778–7781, 2007.
- [42] J. Awaka, N. Kijima, H. Hayakawa, and J. Akimoto, "Synthesis and structure analysis of tetragonal $\text{Li}_7\text{La}_3\text{Zr}_2\text{O}_{12}$ with the garnet-related type structure," *Journal of Solid State Chemistry*, vol. 182, no. 8, pp. 2046–2052, 2009.
- [43] M. Matsui, K. Takahashi, K. Sakamoto, A. Hirano, Y. Takeda, O. Yamamoto, and N. Imanishi, "Phase stability of a garnet-type lithium ion conductor $\text{Li}_7\text{La}_3\text{Zr}_2\text{O}_{12}$," *Dalton Transactions*, vol. 43, no. 3, pp. 1019–1024, 2014.
- [44] J. Percival, E. Kendrick, R. Smith, and P. Slater, "Cation ordering in Li containing garnets: synthesis and structural characterisation of the tetragonal system, $\text{Li}_7\text{La}_3\text{Sn}_2\text{O}_{12}$," *Dalton Transactions*, no. 26, pp. 5177–5181, 2009.
- [45] E. J. Cussen, "Structure and ionic conductivity in lithium garnets," *Journal of Materials Chemistry*, vol. 20, no. 25, pp. 5167–5173, 2010.
- [46] K. Meier, T. Laino, and A. Curioni, "Solid-state electrolytes: Revealing the mechanisms of Li-ion conduction in tetragonal and cubic LLZO by first-principles calculations," *The Journal of Physical Chemistry C*, vol. 118, no. 13, pp. 6668–6679, 2014.
- [47] J. Awaka, A. Takashima, K. Kataoka, N. Kijima, Y. Idemoto, and J. Akimoto, "Crystal structure of fast lithium-ion-conducting cubic $\text{Li}_7\text{La}_3\text{Zr}_2\text{O}_{12}$," *Chemistry Letters*, vol. 40, no. 1, pp. 60–62, 2010.
- [48] M. Xu, M. S. Park, J. M. Lee, T. Y. Kim, Y. S. Park, and E. Ma, "Mechanisms of Li^+ transport in garnet-type cubic $\text{Li}_{3+x}\text{La}_3\text{M}_2\text{O}_{12}$ (M= Te, Nb, Zr)," *Physical Review B*, vol. 85, no. 5, p. 052301, 2012.
- [49] Y. Li, J.-T. Han, C.-A. Wang, S. C. Vogel, H. Xie, M. Xu, and J. B. Goodenough, "Ionic distribution and conductivity in lithium garnet $\text{Li}_7\text{La}_3\text{Zr}_2\text{O}_{12}$," *Journal of Power Sources*, vol. 209, pp. 278–281, 2012.

- [50] H. Buschmann, J. Dölle, S. Berendts, A. Kuhn, P. Bottke, M. Wilkening, P. Heitjans, A. Senyshyn, H. Ehrenberg, A. Lotnyk, *et al.*, “Structure and dynamics of the fast lithium ion conductor $\text{Li}_7\text{La}_3\text{Zr}_2\text{O}_{12}$,” *Physical Chemistry Chemical Physics*, vol. 13, no. 43, pp. 19378–19392, 2011.
- [51] C. A. Geiger, E. Alekseev, B. Lazic, M. Fisch, T. Armbruster, R. Langner, M. Fechtelkord, N. Kim, T. Pettke, and W. Weppner, “Crystal chemistry and stability of $\text{Li}_7\text{La}_3\text{Zr}_2\text{O}_{12}$ garnet: A fast lithium-ion conductor,” *Inorganic Chemistry*, vol. 50, no. 3, pp. 1089–1097, 2010.
- [52] J. Wolfenstine, J. Sakamoto, and J. Allen, “Electron microscopy characterization of hot-pressed Al substituted $\text{Li}_7\text{La}_3\text{Zr}_2\text{O}_{12}$,” *Journal of Materials Science*, vol. 47, no. 10, pp. 4428–4431, 2012.
- [53] T. Thompson, J. Wolfenstine, J. L. Allen, M. Johannes, A. Huq, I. N. David, and J. Sakamoto, “Tetragonal vs. cubic phase stability in Al-free Ta doped $\text{Li}_7\text{La}_3\text{Zr}_2\text{O}_{12}$ (LLZO),” *Journal of Materials Chemistry A*, vol. 2, no. 33, pp. 13431–13436, 2014.
- [54] W. G. Zeier, “Structural limitations for optimizing garnet-type solid electrolytes: a perspective,” *Dalton Transactions*, vol. 43, no. 43, pp. 16133–16138, 2014.
- [55] D. Rettenwander, P. Blaha, R. Laskowski, K. Schwarz, P. Bottke, M. Wilkening, C. A. Geiger, and G. Amthauer, “DFT Study of the Role of Al^{3+} in the Fast Ion-Conductor $\text{Li}_{7-3x}\text{Al}_{3+x}\text{La}_3\text{Zr}_2\text{O}_{12}$ Garnet,” *Chemistry of Materials*, vol. 26, no. 8, pp. 2617–2623, 2014.
- [56] D. Rettenwander, J. Langer, W. Schmidt, C. Arrer, K. J. Harris, V. Terskikh, G. R. Goward, M. Wilkening, and G. Amthauer, “Site Occupation of Ga and Al in Stabilized Cubic $\text{Li}_{7-3(x+y)}\text{Ga}_x\text{Al}_y\text{La}_3\text{Zr}_2\text{O}_{12}$ Garnets As Deduced from ^{27}Al and ^{71}Ga MAS NMR at Ultrahigh Magnetic Fields,” *Chemistry of Materials*, vol. 27, no. 8, pp. 3135–3142, 2015.
- [57] C. Galven, J.-L. Fourquet, M.-P. Crosnier-Lopez, and F. Le Berre, “Instability

- of the lithium garnet $\text{Li}_7\text{La}_3\text{Sn}_2\text{O}_{12}$: Li^+/H^+ exchange and structural study,” *Chemistry of Materials*, vol. 23, no. 7, pp. 1892–1900, 2011.
- [58] C. Galven, J. Dittmer, E. Suard, F. Le Berre, and M.-P. Crosnier-Lopez, “Instability of Lithium Garnets against Moisture. Structural Characterization and Dynamics of $\text{Li}_{7-x}\text{H}_x\text{La}_3\text{Sn}_2\text{O}_{12}$ and $\text{Li}_{5-x}\text{H}_x\text{La}_3\text{Nb}_2\text{O}_{12}$,” *Chemistry of Materials*, vol. 24, no. 17, pp. 3335–3345, 2012.
- [59] G. Larraz, A. Orera, and M. Sanjuan, “Cubic phases of garnet-type $\text{Li}_7\text{La}_3\text{Zr}_2\text{O}_{12}$: the role of hydration,” *Journal of Materials Chemistry A*, vol. 1, no. 37, pp. 11419–11428, 2013.
- [60] Y. Jin and P. J. McGinn, “ $\text{Li}_7\text{La}_3\text{Zr}_2\text{O}_{12}$ electrolyte stability in air and fabrication of a $\text{Li}/\text{Li}_7\text{La}_3\text{Zr}_2\text{O}_{12}/\text{Cu}_{0.1}\text{V}_2\text{O}_5$ solid-state battery,” *Journal of Power Sources*, vol. 239, pp. 326–331, 2013.
- [61] X. Wang, Y. Xia, J. Hu, Y. Xia, Z. Zhuang, L. Guo, H. Lu, T. Zhang, and Q. Fang, “Phase transition and conductivity improvement of tetragonal fast lithium ionic electrolyte $\text{Li}_7\text{La}_3\text{Zr}_2\text{O}_{12}$,” *Solid State Ionics*, vol. 253, pp. 137–142, 2013.
- [62] F. Gam, C. Galven, A. Bulou, F. Le Berre, and M.-P. Crosnier-Lopez, “Reinvestigation of the Total Li^+/H^+ Ion Exchange on the Garnet-Type $\text{Li}_5\text{La}_3\text{Nb}_2\text{O}_{12}$,” *Inorganic Chemistry*, vol. 53, no. 2, pp. 931–934, 2014.
- [63] Y. Wang and W. Lai, “Phase transition in lithium garnet oxide ionic conductors $\text{Li}_7\text{La}_3\text{Zr}_2\text{O}_{12}$: The role of Ta substitution and $\text{H}_2\text{O}/\text{CO}_2$ exposure,” *Journal of Power Sources*, vol. 275, pp. 612–620, 2015.
- [64] L. Cheng, C. H. Wu, A. Jarry, W. Chen, Y. Ye, J. Zhu, R. Kostecki, K. Persson, J. Guo, M. Salmeron, *et al.*, “Interrelationships among grain size, surface composition, air stability, and interfacial resistance of Al-substituted $\text{Li}_7\text{La}_3\text{Zr}_2\text{O}_{12}$ solid electrolytes,” *ACS applied materials & interfaces*, vol. 7, no. 32, pp. 17649–17655, 2015.

- [65] C. Liu, K. Rui, C. Shen, M. E. Badding, G. Zhang, and Z. Wen, "Reversible ion exchange and structural stability of garnet-type Nb-doped $\text{Li}_7\text{La}_3\text{Zr}_2\text{O}_{12}$ in water for applications in lithium batteries," *Journal of Power Sources*, vol. 282, pp. 286–293, 2015.
- [66] G. Larraz, A. Orera, J. Sanz, I. Sobrados, V. Diez-Gomez, and M. Sanjuan, "NMR study of Li distribution in $\text{Li}_{7-x}\text{H}_x\text{La}_3\text{Zr}_2\text{O}_{12}$ garnets," *Journal of Materials Chemistry A*, vol. 3, no. 10, pp. 5683–5691, 2015.
- [67] A. Orera, G. Larraz, J. A. Rodríguez-Velamazán, J. Campo, and M. L. Sanjuan, "Influence of Li^+ and H^+ Distribution on the Crystal Structure of $\text{Li}_{7-x}\text{H}_x\text{La}_3\text{Zr}_2\text{O}_{12}$ ($0 \leq x \leq 5$) Garnets," *Inorganic chemistry*, vol. 55, no. 3, pp. 1324–1332, 2016.
- [68] W. Xia, B. Xu, H. Duan, Y. Guo, H. Kang, H. Li, and H. Liu, "Ionic conductivity and air stability of Al-doped $\text{Li}_7\text{La}_3\text{Zr}_2\text{O}_{12}$ sintered in alumina and Pt crucibles," *ACS applied materials & interfaces*, vol. 8, no. 8, pp. 5335–5342, 2016.
- [69] M. Matsui, K. Sakamoto, K. Takahashi, A. Hirano, Y. Takeda, O. Yamamoto, and N. Imanishi, "Phase transformation of the garnet structured lithium ion conductor: $\text{Li}_7\text{La}_3\text{Zr}_2\text{O}_{12}$," *Solid State Ionics*, vol. 262, pp. 155–159, 2014.
- [70] S. Toda, K. Ishiguro, Y. Shimonishi, A. Hirano, Y. Takeda, O. Yamamoto, and N. Imanishi, "Low temperature cubic garnet-type CO_2 -doped $\text{Li}_7\text{La}_3\text{Zr}_2\text{O}_{12}$," *Solid State Ionics*, vol. 233, pp. 102–106, 2013.
- [71] Y. Zhang, F. Chen, R. Tu, Q. Shen, X. Zhang, and L. Zhang, "Effect of lithium ion concentration on the microstructure evolution and its association with the ionic conductivity of cubic garnet-type nominal $\text{Li}_7\text{Al}_{0.25}\text{La}_3\text{Zr}_2\text{O}_{12}$ solid electrolytes," *Solid State Ionics*, vol. 284, pp. 53–60, 2016.
- [72] J. Fleig and J. Maier, "Local conductivity measurements on AgCl surfaces using microelectrodes," *Solid State Ionics*, vol. 85, no. 1, pp. 9–15, 1996.

- [73] J. Fleig and J. Maier, "Microcontact impedance measurements of individual highly conductive grain boundaries: General aspects and application to AgCl," *Physical Chemistry Chemical Physics*, vol. 1, no. 14, pp. 3315–3320, 1999.
- [74] J. Fleig, "Microelectrodes in solid state ionics," *Solid State Ionics*, vol. 161, no. 3, pp. 279–289, 2003.
- [75] J.-S. Lee, J. Fleig, J. Maier, T.-J. Chung, and D.-Y. Kim, "Microcontact impedance spectroscopy in nitrogen-graded zirconia," *Solid State Ionics*, vol. 176, no. 19, pp. 1711–1716, 2005.
- [76] Y. Jin and P. J. McGinn, "Al-doped $\text{Li}_7\text{La}_3\text{Zr}_2\text{O}_{12}$ synthesized by a polymerized complex method," *Journal of Power Sources*, vol. 196, no. 20, pp. 8683–8687, 2011.
- [77] E. Rangasamy, J. Wolfenstine, and J. Sakamoto, "The role of Al and Li concentration on the formation of cubic garnet solid electrolyte of nominal composition $\text{Li}_7\text{La}_3\text{Zr}_2\text{O}_{12}$," *Solid State Ionics*, vol. 206, pp. 28–32, 2012.
- [78] D. Rettenwander, C. A. Geiger, and G. Amthauer, "Synthesis and crystal chemistry of the fast Li-ion conductor $\text{Li}_7\text{La}_3\text{Zr}_2\text{O}_{12}$ doped with Fe," *Inorganic Chemistry*, vol. 52, no. 14, pp. 8005–8009, 2013.
- [79] D. Rettenwander, C. Geiger, M. Tribus, P. Tropper, R. Wagner, G. Tippelt, W. Lottermoser, and G. Amthauer, "The solubility and site preference of Fe^{3+} in $\text{Li}_{7-3x}\text{Fe}_x\text{La}_3\text{Zr}_2\text{O}_{12}$ garnets," *Journal of solid state chemistry*, vol. 230, pp. 266–271, 2015.
- [80] D. Rettenwander, C. A. Geiger, M. Tribus, P. Tropper, and G. Amthauer, "A Synthesis and Crystal Chemical Study of the Fast Ion Conductor $\text{Li}_{7-3x}\text{Ga}_x\text{La}_3\text{Zr}_2\text{O}_{12}$ with $x = 0.08$ to 0.84 ," *Inorganic chemistry*, vol. 53, no. 12, pp. 6264–6269, 2014.
- [81] J. L. Allen, J. Wolfenstine, E. Rangasamy, and J. Sakamoto, "Effect of substitution (Ta, Al, Ga) on the conductivity of $\text{Li}_7\text{La}_3\text{Zr}_2\text{O}_{12}$," *Journal of Power Sources*, vol. 206, pp. 315–319, 2012.

- [82] J. Wolfenstine, J. Ratchford, E. Rangasamy, J. Sakamoto, and J. L. Allen, "Synthesis and high Li-ion conductivity of Ga-stabilized cubic $\text{Li}_7\text{La}_3\text{Zr}_2\text{O}_{12}$," *Materials Chemistry and Physics*, vol. 134, no. 2, pp. 571–575, 2012.
- [83] Y. Chen, E. Rangasamy, C. Liang, and K. An, "Origin of high Li^+ conduction in doped $\text{Li}_7\text{La}_3\text{Zr}_2\text{O}_{12}$ garnets," *Chemistry of Materials*, vol. 27, no. 16, pp. 5491–5494, 2015.
- [84] E. Rangasamy, J. Wolfenstine, J. Allen, and J. Sakamoto, "The effect of 24c-site (A) cation substitution on the tetragonal–cubic phase transition in $\text{Li}_{7-x}\text{La}_{3-x}\text{A}_x\text{Zr}_2\text{O}_{12}$ garnet-based ceramic electrolyte," *Journal of Power Sources*, vol. 230, pp. 261–266, 2013.
- [85] P. Bottke, D. Rettenwander, W. Schmidt, G. Amthauer, and M. Wilkening, "Ion dynamics in solid electrolytes: NMR reveals the elementary steps of Li^+ hopping in the garnet $\text{Li}_{6.5}\text{La}_3\text{Zr}_{1.75}\text{Mo}_{0.25}\text{O}_{12}$," *Chemistry of Materials*, vol. 27, no. 19, pp. 6571–6582, 2015.
- [86] A. Logéat, T. Köhler, U. Eisele, B. Stiaszny, A. Harzer, M. Tovar, A. Senyshyn, H. Ehrenberg, and B. Kozinsky, "From order to disorder: The structure of lithium-conducting garnets $\text{Li}_{7-x}\text{La}_3\text{Ta}_x\text{Zr}_{2-x}\text{O}_{12}$ ($x = 0-2$)," *Solid State Ionics*, vol. 206, pp. 33–38, 2012.
- [87] S. Mukhopadhyay, T. Thompson, J. Sakamoto, A. Huq, J. Wolfenstine, J. L. Allen, N. Bernstein, D. A. Stewart, and M. Johannes, "Structure and stoichiometry in supervalent doped $\text{Li}_7\text{La}_3\text{Zr}_2\text{O}_{12}$," *Chemistry of Materials*, vol. 27, no. 10, pp. 3658–3665, 2015.
- [88] Y. Li, C.-A. Wang, H. Xie, J. Cheng, and J. B. Goodenough, "High lithium ion conduction in garnet-type $\text{Li}_6\text{La}_3\text{ZrTaO}_{12}$," *Electrochemistry Communications*, vol. 13, no. 12, pp. 1289–1292, 2011.
- [89] H. Buschmann, S. Berendts, B. Mogwitz, and J. Janek, "Lithium metal electrode kinetics and ionic conductivity of the solid lithium ion conductors $\text{Li}_7\text{La}_3\text{Zr}_2\text{O}_{12}$

- and $\text{Li}_{7-x}\text{La}_3\text{Zr}_{2-x}\text{Ta}_x\text{O}_{12}$ with garnet-type structure,” *Journal of Power Sources*, vol. 206, pp. 236–244, 2012.
- [90] S. Ohta, T. Kobayashi, and T. Asaoka, “High lithium ionic conductivity in the garnet-type oxide $\text{Li}_{7-x}\text{La}_3(\text{Zr}_{2-x}\text{Nb}_x)\text{O}_{12}$ ($x = 0-2$),” *Journal of Power Sources*, vol. 196, no. 6, pp. 3342–3345, 2011.
- [91] S. Ramakumar, L. Satyanarayana, S. V. Manorama, and R. Murugan, “Structure and Li^+ dynamics of Sb-doped $\text{Li}_7\text{La}_3\text{Zr}_2\text{O}_{12}$ fast lithium ion conductors,” *Physical Chemistry Chemical Physics*, vol. 15, no. 27, pp. 11327–11338, 2013.
- [92] C. Deviannapoorani, L. Dhivya, S. Ramakumar, and R. Murugan, “Lithium ion transport properties of high conductive tellurium substituted $\text{Li}_7\text{La}_3\text{Zr}_2\text{O}_{12}$ cubic lithium garnets,” *Journal of Power Sources*, vol. 240, pp. 18–25, 2013.
- [93] L. Dhivya, N. Janani, B. Palanivel, and R. Murugan, “ Li^+ transport properties of W substituted $\text{Li}_7\text{La}_3\text{Zr}_2\text{O}_{12}$ cubic lithium garnets,” *Aip Advances*, vol. 3, no. 8, p. 082115, 2013.
- [94] Y. Xia, L. Ma, H. Lu, X.-P. Wang, Y.-X. Gao, W. Liu, Z. Zhuang, L.-J. Guo, and Q.-F. Fang, “Preparation and enhancement of ionic conductivity in Al-added garnet-like $\text{Li}_{6.8}\text{La}_3\text{Zr}_{1.8}\text{Bi}_{0.2}\text{O}_{12}$ lithium ionic electrolyte,” *Frontiers of Materials Science*, vol. 9, no. 4, pp. 366–372, 2015.
- [95] Y. Suzuki, K. Kami, K. Watanabe, A. Watanabe, N. Saito, T. Ohnishi, K. Takada, R. Sudo, and N. Imanishi, “Transparent cubic garnet-type solid electrolyte of Al_2O_3 -doped $\text{Li}_7\text{La}_3\text{Zr}_2\text{O}_{12}$,” *Solid State Ionics*, vol. 278, pp. 172–176, 2015.
- [96] M. Botros, R. Djenadic, O. Clemens, M. Moller, and H. Hahn, “Field assisted sintering of fine-grained $\text{Li}_{7-3x}\text{La}_3\text{Zr}_2\text{Al}_x\text{O}_{12}$ solid electrolyte and the influence of the microstructure on the electrochemical performance,” *Journal of Power Sources*, vol. 309, pp. 108–115, 2016.
- [97] R. Sudo, Y. Nakata, K. Ishiguro, M. Matsui, A. Hirano, Y. Takeda, O. Yamamoto,

- and N. Imanishi, "Interface behavior between garnet-type lithium-conducting solid electrolyte and lithium metal," *Solid State Ionics*, vol. 262, pp. 151–154, 2014.
- [98] D. Rettenwander, G. Redhammer, F. Preishuber-Pfluegl, L. Cheng, L. Miara, R. Wagner, A. Welzl, E. Suard, M. M. Doeff, M. Wilkening, *et al.*, "Structural and electrochemical consequences of Al and Ga cosubstitution in $\text{Li}_7\text{La}_3\text{Zr}_2\text{O}_{12}$ solid electrolytes," *Chemistry of Materials*, vol. 28, no. 7, pp. 2384–2392, 2016.
- [99] C.-L. Tsai, E. Dashjav, E.-M. Hammer, M. Finsterbusch, F. Tietz, S. Uhlenbruck, and H. P. Buchkremer, "High conductivity of mixed phase Al-substituted $\text{Li}_7\text{La}_3\text{Zr}_2\text{O}_{12}$," *Journal of Electroceramics*, vol. 35, no. 1-4, pp. 25–32, 2015.
- [100] M. Kotobuki, K. Kanamura, Y. Sato, and T. Yoshida, "Fabrication of all-solid-state lithium battery with lithium metal anode using Al_2O_3 -added $\text{Li}_7\text{La}_3\text{Zr}_2\text{O}_{12}$ solid electrolyte," *Journal of Power Sources*, vol. 196, no. 18, pp. 7750–7754, 2011.
- [101] S. Kumazaki, Y. Iriyama, K.-H. Kim, R. Murugan, K. Tanabe, K. Yamamoto, T. Hirayama, and Z. Ogumi, "High lithium ion conductive $\text{Li}_7\text{La}_3\text{Zr}_2\text{O}_{12}$ by inclusion of both Al and Si," *Electrochemistry Communications*, vol. 13, no. 5, pp. 509–512, 2011.
- [102] W. E. Tenhaeff, E. Rangasamy, Y. Wang, A. P. Sokolov, J. Wolfenstine, J. Sakamoto, and N. J. Dudney, "Resolving the Grain Boundary and Lattice Impedance of Hot-Pressed $\text{Li}_7\text{La}_3\text{Zr}_2\text{O}_{12}$ Garnet Electrolytes," *ChemElectroChem*, vol. 1, no. 2, pp. 375–378, 2014.
- [103] J. van den Broek, S. Afyon, and J. L. Rupp, "Interface-Engineered All-Solid-State Li-Ion Batteries Based on Garnet-Type Fast Li^+ Conductors," *Advanced Energy Materials*, vol. 6, no. 19, 2016.
- [104] Y. Zhang, J. Cai, F. Chen, R. Tu, Q. Shen, X. Zhang, and L. Zhang, "Preparation of cubic $\text{Li}_7\text{La}_3\text{Zr}_2\text{O}_{12}$ solid electrolyte using a nano-sized core-shell structured precursor," *Journal of Alloys and Compounds*, vol. 644, pp. 793–798, 2015.

- [105] Y. Zhang, F. Chen, R. Tu, Q. Shen, and L. Zhang, “Field assisted sintering of dense Al-substituted cubic phase $\text{Li}_7\text{La}_3\text{Zr}_2\text{O}_{12}$ solid electrolytes,” *Journal of Power Sources*, vol. 268, pp. 960–964, 2014.
- [106] Y. Matsuda, K. Sakamoto, M. Matsui, O. Yamamoto, Y. Takeda, and N. Imanishi, “Phase formation of a garnet-type lithium-ion conductor $\text{Li}_{7-3x}\text{La}_3\text{Zr}_2\text{O}_{12}$,” *Solid State Ionics*, vol. 277, pp. 23–29, 2015.
- [107] Y. Kim, H. Jo, J. L. Allen, H. Choe, J. Wolfenstine, and J. Sakamoto, “The Effect of Relative Density on the Mechanical Properties of Hot-Pressed Cubic $\text{Li}_7\text{La}_3\text{Zr}_2\text{O}_{12}$,” *Journal of the American Ceramic Society*, 2016.
- [108] Z. Hu, H. Liu, H. Ruan, R. Hu, Y. Su, and L. Zhang, “High Li-ion conductivity of Al-doped $\text{Li}_7\text{La}_3\text{Zr}_2\text{O}_{12}$ synthesized by solid-state reaction,” *Ceramics International*, vol. 42, no. 10, pp. 12156–12160, 2016.
- [109] R.-J. Chen, M. Huang, W.-Z. Huang, Y. Shen, Y.-H. Lin, and C.-W. Nan, “Effect of calcining and Al doping on structure and conductivity of $\text{Li}_7\text{La}_3\text{Zr}_2\text{O}_{12}$,” *Solid State Ionics*, vol. 265, pp. 7–12, 2014.
- [110] S. R. Catarelli, D. Lonsdale, L. Cheng, J. Syzdek, and M. Doeff, “Intermittent Contact Alternating Current Scanning Electrochemical Microscopy: A Method for Mapping Conductivities in Solid Li Ion Conducting Electrolyte Samples,” *Frontiers in Energy Research*, vol. 4, p. 14, 2016.
- [111] L. Cheng, J. S. Park, H. Hou, V. Zorba, G. Chen, T. Richardson, J. Cabana, R. Russo, and M. Doeff, “Effect of microstructure and surface impurity segregation on the electrical and electrochemical properties of dense Al-substituted $\text{Li}_7\text{La}_3\text{Zr}_2\text{O}_{12}$,” *Journal of Materials Chemistry A*, vol. 2, no. 1, pp. 172–181, 2014.
- [112] I. N. David, T. Thompson, J. Wolfenstine, J. L. Allen, and J. Sakamoto, “Microstructure and Li-Ion Conductivity of Hot-Pressed Cubic $\text{Li}_7\text{La}_3\text{Zr}_2\text{O}_{12}$,” *Journal of the American Ceramic Society*, vol. 98, no. 4, pp. 1209–1214, 2015.

- [113] R. Wagner, D. Rettenwander, G. J. Redhammer, G. Tippelt, G. Sabathi, M. E. Musso, B. Stanje, M. Wilkening, E. Suard, and G. Amthauer, "Synthesis, Crystal Structure, and Stability of Cubic $\text{Li}_{7-x}\text{La}_3\text{Zr}_{2-x}\text{Bi}_x\text{O}_{12}$," *Inorganic Chemistry*, 2016.
- [114] A. Wachter-Welzl, J. Kirowitz, R. Wagner, S. Smetaczek, G. Brunbauer, M. Bonta, D. Rettenwander, S. Taibl, A. Limbeck, G. Amthauer, and J. Fleig, "The origin of conductivity variations in Al-stabilized $\text{Li}_7\text{La}_3\text{Zr}_2\text{O}_{12}$ ceramics," *Submitted*, 2017.
- [115] R. Wagner, G. J. Redhammer, D. Rettenwander, A. Senyshyn, W. Schmidt, M. Wilkening, and G. Amthauer, "Crystal Structure of Garnet-Related Li-Ion Conductor $\text{Li}_{7-3x}\text{Ga}_x\text{La}_3\text{Zr}_2\text{O}_{12}$: Fast Li-Ion Conduction Caused by a Different Cubic Modification?," *Chemistry of Materials*, vol. 28, no. 6, pp. 1861–1871, 2016.
- [116] "Panalytical," 2016.
- [117] J. Fleig, "The grain boundary impedance of random microstructures: numerical simulations and implications for the analysis of experimental data," *Solid State Ionics*, vol. 150, no. 1, pp. 181–193, 2002.
- [118] Q. Zhao, M. B. Nardelli, and J. Bernholc, "Ultimate strength of carbon nanotubes: A theoretical study," *Physical Review B*, vol. 65, no. 14, p. 144105, 2002.
- [119] H. Hou, L. Cheng, T. Richardson, G. Chen, M. Doeff, R. Zheng, R. Russo, and V. Zorba, "Three-dimensional elemental imaging of Li-ion solid-state electrolytes using fs-laser induced breakdown spectroscopy (LIBS)," *Journal of Analytical Atomic Spectrometry*, vol. 30, no. 11, pp. 2295–2302, 2015.
- [120] A. Wachter-Welzl, S. Smetaczek, R. Wagner, D. Rettenwander, S. Taibl, G. Amthauer, A. Limbeck, and J. Fleig, "Li-ion conductivity fluctuations within $\text{Li}_7\text{La}_3\text{Zr}_2\text{O}_{12}$ solid electrolytes and their relation to local stoichiometric changes," *Submitted*, 2017.
- [121] R. Wagner, G. J. Redhammer, D. Rettenwander, G. Tippelt, A. Welzl, S. Taibl, J. Fleig, A. Franz, W. Lottermoser, and G. Amthauer, "Fast Li-Ion-Conducting

- Garnet-Related $\text{Li}_{7-3x}\text{Fe}_x\text{La}_3\text{Zr}_2\text{O}_{12}$ with Uncommon $\bar{1}43d$ Structure,” *Chemistry of Materials*, vol. 28, no. 16, pp. 5943–5951, 2016.
- [122] Y. Li, J.-T. Han, C.-A. Wang, H. Xie, and J. B. Goodenough, “Optimizing Li^+ conductivity in a garnet framework,” *Journal of Materials Chemistry*, vol. 22, no. 30, pp. 15357–15361, 2012.
- [123] S. Adams and R. P. Rao, “Ion transport and phase transition in $\text{Li}_{7-x}\text{La}_3(\text{Zr}_{2-x}\text{M}_x)\text{O}_{12}$ ($\text{M} = \text{Ta } 5^+, \text{Nb } 5^+, x = 0, 0.25$),” *Journal of Materials Chemistry*, vol. 22, no. 4, pp. 1426–1434, 2012.
- [124] Y. Shimonishi, A. Toda, T. Zhang, A. Hirano, N. Imanishi, O. Yamamoto, and Y. Takeda, “Synthesis of garnet-type $\text{Li}_{7-x}\text{La}_3\text{Zr}_2\text{O}_{12-1/2x}$ and its stability in aqueous solutions,” *Solid State Ionics*, vol. 183, no. 1, pp. 48–53, 2011.
- [125] I. Kokal, M. Somer, P. Notten, and H. Hintzen, “Sol–gel synthesis and lithium ion conductivity of $\text{Li}_7\text{La}_3\text{Zr}_2\text{O}_{12}$ with garnet-related type structure,” *Solid State Ionics*, vol. 185, no. 1, pp. 42–46, 2011.
- [126] E. Ilina, O. Andreev, B. Antonov, and N. Batalov, “Morphology and transport properties of the solid electrolyte $\text{Li}_7\text{La}_3\text{Zr}_2\text{O}_{12}$ prepared by the solid-state and citrate–nitrate methods,” *Journal of Power Sources*, vol. 201, pp. 169–173, 2012.
- [127] J. Wolfenstine, E. Rangasamy, J. L. Allen, and J. Sakamoto, “High conductivity of dense tetragonal $\text{Li}_7\text{La}_3\text{Zr}_2\text{O}_{12}$,” *Journal of Power Sources*, vol. 208, pp. 193–196, 2012.
- [128] “Leibniz Institute for Crystal Growth, Max-Born-Strasse 2, 12389 Berlin, Germany,” 2017.
- [129] B. Stanje, D. Rettenwander, S. Breuer, M. Uitz, S. Berendts, M. Lerch, R. Uecker, G. Redhammer, I. Hanzu, and M. Wilkening, “Extremely Fast Charge Carriers in Garnet-Type $\text{Li}_6\text{La}_3\text{ZrTaO}_{12}$ Single Crystals,” *Solid Electrolytes*, 2017.

- [130] L. Truong and V. Thangadurai, “Soft-Chemistry of Garnet-Type $\text{Li}_{5+x}\text{Ba}_x\text{La}_{3-x}\text{Nb}_2\text{O}_{12}$ ($x= 0, 0.5, 1$): Reversible $\text{H}^+ \leftrightarrow \text{Li}^+$ Ion-Exchange Reaction and Their X-ray, ^7Li MAS NMR, IR, and AC Impedance Spectroscopy Characterization,” *Chemistry of Materials*, vol. 23, no. 17, pp. 3970–3977, 2011.
- [131] L. Truong, J. Colter, and V. Thangadurai, “Chemical stability of Li-stuffed garnet-type $\text{Li}_{5+x}\text{Ba}_x\text{La}_{3-x}\text{Ta}_2\text{O}_{12}$ ($x= 0, 0.5, 1$) in water: a comparative analysis with the Nb analogue,” *Solid State Ionics*, vol. 247, pp. 1–7, 2013.
- [132] Z. F. Yow, Y. L. Oh, W. Gu, R. P. Rao, and S. Adams, “Effect of Li^+/H^+ exchange in water treated Ta-doped $\text{Li}_7\text{La}_3\text{Zr}_2\text{O}_{12}$,” *Solid State Ionics*, vol. 292, pp. 122–129, 2016.
- [133] M. Kubicek, A. Wachter-Welzl, D. Rettenwander, R. Wagner, S. Berendts, R. Uecker, G. Amthauer, H. Hutter, and J. Fleig, “Oxygen Vacancies in Fast Lithium-Ion Conducting Garnets,” *Chemistry of Materials*, 2017.
- [134] A. Wachter-Welzl, R. Wagner, D. Rettenwander, S. Taibl, G. Amthauer, and J. Fleig, “Microelectrodes for local conductivity and degradation measurements on Al stabilized $\text{Li}_7\text{La}_3\text{Zr}_2\text{O}_{12}$ garnets,” *Journal of Electroceramics*, pp. 1–6, 2016.
- [135] J. Maier, “On the conductivity of polycrystalline materials,” *Berichte der Bunsengesellschaft für physikalische Chemie*, vol. 90, no. 1, pp. 26–33, 1986.
- [136] F. Llewellyn-Jones, “The physics of electrical contacts,” *Oxford*, 1957.
- [137] A. Aguadero, F. Aguesse, C. Bernuy-López, W. W. Manalastas, J. M. L. del Amo, and J. A. Kilner, “Improvement of Transport Properties in Li-Conducting Ceramic Oxides,” in *Meeting Abstracts*, no. 2 in -, pp. 503–503, The Electrochemical Society, 2015.
- [138] C. Ma, E. Rangasamy, C. Liang, J. Sakamoto, K. L. More, and M. Chi, “Excellent Stability of a Lithium-Ion-Conducting Solid Electrolyte upon Reversible Li^+/H^+ Exchange in Aqueous Solutions,” *Angewandte Chemie*, vol. 127, no. 1, pp. 131–135, 2015.

- [139] Y. Liu, Z. Hu, S. Gao, D. Günther, J. Xu, C. Gao, and H. Chen, “In situ analysis of major and trace elements of anhydrous minerals by LA-ICP-MS without applying an internal standard,” *Chemical Geology*, vol. 257, no. 1, pp. 34–43, 2008.
- [140] S. Smetaczek, “In preparation,” -, 2017.
- [141] R. Murugan, V. Thangadurai, and W. Weppner, “Lattice parameter and sintering temperature dependence of bulk and grain-boundary conduction of garnet-like solid Li-electrolytes,” *Journal of The Electrochemical Society*, vol. 155, no. 1, pp. A90–A101, 2008.
- [142] T. Luna and V. Thangadurai, “Soft-Chemistry of Garnet-Type $\text{Li}_{5+x}\text{Ba}_x\text{La}_{3-x}\text{Nb}_2\text{O}_{12}$ ($x= 0, 0.5, 1$): Reversible $\text{H}^+ \longleftrightarrow \text{Li}^+$ Ion-Exchange Reaction and Their X-ray, Li-7 MAS NMR, IR, and AC Impedance Spectroscopy Characterization,” *Chem. Mater.*, vol. 23, no. 17, pp. 3970–7, 2011.
- [143] C. Galven, E. Suard, D. Mounier, M.-P. Crosnier-Lopez, and F. Le Berre, “Structural characterization of a new acentric protonated garnet: $\text{Li}_{6-x}\text{H}_x\text{CaLa}_2\text{Nb}_2\text{O}_{12}$,” *Journal of Materials Research*, vol. 28, no. 16, pp. 2147–2153, 2013.
- [144] M. Howard, O. Clemens, E. Kendrick, K. Knight, D. Apperley, P. Anderson, and P. Slater, “Effect of Ga incorporation on the structure and Li ion conductivity of $\text{La}_3\text{Zr}_2\text{Li}_7\text{O}_{12}$,” *Dalton Transactions*, vol. 41, no. 39, pp. 12048–12053, 2012.
- [145] L. Truong and V. Thangadurai, “First Total H^+/Li^+ Ion Exchange in Garnet-Type $\text{Li}_5\text{La}_3\text{Nb}_2\text{O}_{12}$ Using Organic Acids and Studies on the Effect of Li Stuffing,” *Inorganic Chemistry*, vol. 51, no. 3, pp. 1222–1224, 2012.
- [146] Y. Li, J.-T. Han, S. C. Vogel, and C.-A. Wang, “The reaction of $\text{Li}_{6.5}\text{La}_3\text{Zr}_{1.5}\text{Ta}_{0.5}\text{O}_{12}$ with water,” *Solid State Ionics*, vol. 269, pp. 57–61, 2015.
- [147] M. Nyman, T. M. Alam, S. K. McIntyre, G. C. Bleier, and D. Ingersoll, “Alternative approach to increasing Li mobility in Li-La-Nb/Ta garnet electrolytes,” *Chemistry of Materials*, vol. 22, no. 19, pp. 5401–5410, 2010.